

Optomechanical Coupling in an Interferometer with a SiN-Membrane

Der Fakultät für Mathematik und Physik
der Gottfried Wilhelm Leibniz Universität Hannover
zur Erlangung des Grades

**Doktor der Naturwissenschaften
Dr. rer. nat.**

genehmigte Dissertation
von

MSc. Andreas Sawadsky

2017

Referent: Prof. Dr. Roman Schnabel
Korreferent: Prof. Dr. Karsten Danzmann
Tag der Promotion 30.08.2017

Abstract

The optomechanical coupling between photons and a mechanical oscillator due to radiation pressure force has an important impact for the exploration of macroscopic quantum physics as well as in the field of gravitational-wave (GW) detection. Future GW detectors will on one hand be limited by radiation pressure noise (RPN) and on the other hand this coupling can also increase their sensitivity, e.g., via the optical spring effect.

The first half of this thesis presents the observation of the generalized, that is, dispersive and dissipative, optomechanical coupling in a signal-recycled Michelson-Sagnac interferometer (MSI). Here the mechanical oscillator was a macroscopic $1.5 \times 1.5 \text{ mm}^2$ sized SiN membrane, which served as a common end mirror of the Michelson mode. For the first time the presence of strong dissipative coupling in an optomechanical system could be demonstrated by the observation of optical cooling on cavity resonance and a second instability regime on the cooling side of the cavity resonance with excellent agreement with the theoretically model. Thereby the effective temperature of the mechanical oscillator could be reduced by 3 orders of magnitude to 126 mK.

Besides the dynamical radiation force this topology in principle also allows the detection of RPN. It has been shown that for the detection of this quantum noise the interferometer has to be operating at cryogenic temperatures. Therefore in the second half of the thesis several new MSIs for low temperatures were realized and investigated. Thereby a reduction of the thermal displacement noise by one order of magnitude was achieved and a displacement sensitivity of $3 \cdot 10^{-16} \text{ m}/\sqrt{\text{Hz}}$ at 10 K was measured the frequency next to the fundamental mode of the membrane. For the final interferometer, high mechanical and dimensional stability over the temperature range of 300 K to 10 K was achieved by utilization of a nickel-iron alloy (Invar) with a thermal expansion of $2 \cdot 10^{-6} 1/\text{K}$. The interferometer was remotely controllable by customized high precision positioner stack for the alignment of the optics with a small step size in the nm regime. Thereby an interferometer contrast of 0.9996 at 293 K could be demonstrated. At a temperature of 16 K the measured contrast was 0.98, and limited by technical issues, so far. This resulting interferometer operating at low temperatures is a big step towards the observation of RPN with a signal-recycled Michelson-Sagnac interferometer.

Keywords: Interferometry, SiN-membranes, Optomechanics, Cryogenics

Kurzfassung

Die optomechanische Kopplung zwischen Photonen und einem mechanischen Oszillator durch Strahlungsdruck hat einen wichtigen Einfluss sowohl auf die Erforschung makroskopischer Quanten Physik als auch im Forschungsfeld der Gravitationswellen (GW) Detektion. Zukünftige GW Detektoren werden einerseits durch das Strahlungsdruckrauschen (SDR) limitiert sein, andererseits aber kann diese Kopplung auch ihre Sensitivität, durch eine optische Feder, erhöhen.

Im ersten Teil dieser Arbeit zeigt die Beobachtung der umfassenden optomechanischen Kopplung, bestehend aus der dispersiven und dissipativen Kopplung, in einem Signal überhöhten Michelson Sagnac Interferometer (MSI). Dabei war der mechanische Oszillator eine makroskopische SiN Membran mit einer Fläche von $1.5 \times 1.5 \text{ mm}^2$. Diese wurde als gemeinsamer Endspiegel für die Michelson Mode eingesetzt. Zum ersten mal konnte starke dissipative Kopplung, durch die Beobachtung von optischer Kühlung auf der Resonator Resonanz und einer zweiten Instabilität auf der Kühlseite der Resonanz, beobachtet werden. Diese stimmte hervorragend mit dem theoretischen Model überein. Dabei konnte die effektive Temperatur des mechanischen Oszillators auf 126 mK reduziert werden.

Neben dem dynamischen Strahlungsdruck ist auch die Beobachtung von Strahlungsdruckrauschen mit dieser Topologie möglich. Es wurde gezeigt, dass das Interferometer dafür zu kryogenen Temperaturen gekühlt werden muss. Deshalb wurden im zweiten Teil der Arbeit einige neue Michelson-Sagnac Interferometer für tiefe Temperaturen realisiert und untersucht. Es wurde eine Absenkung des thermischen Rauschens um eine Größenordnung erreicht. Dabei wurde eine Genauigkeit im Positionsrauschen von $3 \cdot 10^{-16} \text{ m}/\sqrt{\text{Hz}}$ bei 10 K , für Frequenzen in der Nähe der mechanischen Grundmode, erreicht. Das final entwickelte Interferometer wies eine hohe mechanische Stabilität, in einen Temperaturbereich von 300 K bis 10 K , auf. Dies wurde, durch die Verwendung von Invar mit einem thermischen Ausdehnungskoeffizienten von $2 \cdot 10^{-6} 1/\text{K}$, erreicht. Außerdem war das Interferometer durch speziell entwickelte Hoch- Präzisions- Positionierer fernsteuerbar, die eine genaue Justage der Spiegel im nm Bereich ermöglichten. Dadurch konnte bei 293 K ein Kontrast von 0.9996 erreicht werden. Bei 16 K war der gemessene Kontrast 0.98 . Er war limitiert durch technische aufgetretenen Probleme. Diese Interferometer konnte bei kalter Temperatur angewandt werden und ist ein großer Schritt in Richtung des Strahlungsdruckrauschens.

Schlagerworte: Interferometrie, SiN-Membrane, Optomechanik, Kryogenik

Contents

Contents	7
List of Abbreviations	11
List of Figures	13
1. Introduction	15
2. Principles of the Michelson-Sagnac Interferometer	19
2.1. Silicon Nitride Membrane	19
2.1.1. The oscillator transfer function	20
2.2. Topology	21
2.3. Noise Sources	23
2.3.1. Shot Noise	23
2.3.2. Radiation Pressure Noise	24
2.3.3. Thermal Noise	25
2.3.4. Technical Laser Noise	27
2.4. Chapter Conclusion	28
3. Signal-Recycled Michelson-Sagnac Interferometer	31
3.1. Interferometer Cavity Basics	31
3.1.1. Interferometer Cavity Detuning	32
3.1.2. Interferometer Characteristics	35
3.2. Signal Enhancement and Noise Budget	37
3.3. Optomechanical Coupling	39
3.3.1. Optical Spring	39
3.3.2. Dispersive and Dissipative Coupling	40
3.4. Chapter Conclusion	41
4. Observation of Dissipative Coupling and Cooling	43
4.1. Experimental Setup	43
4.1.1. Laser Beam Preparation	44
4.1.2. Interferometer Characteristics	44
4.1.3. Detection Scheme	46
4.2. Optomechanical Cooling Measurements	48
4.2.1. Spectrum Measurement at 126 mK	48
4.2.2. Observation of Dissipative Coupling	49
4.2.3. Cooling on Cavity Resonance	51
4.3. Chapter Conclusion	51

CONTENTS

5. The Cryocooler System	53
5.1. A few Significant Basics at Low Temperature	53
5.1.1. Heat Transfer	53
5.1.2. Properties of Solids	57
5.2. 10 Kelvin Cryogenic System	62
5.2.1. Vacuum System	62
5.2.2. Heat Exchange Gas System	64
5.2.3. Refrigerator System	65
5.3. Modification of the Cryogenic System	67
5.3.1. A new Vacuum Chamber	67
5.3.2. A new Heat Shield	68
5.3.3. Vibration Isolation	69
5.3.4. Wiring	71
5.3.5. Additional Temperature Sensor	74
5.4. Chapter Conclusion	74
6. Towards a Cryogenic Interferometer	77
6.1. Laser Beam Preparation	77
6.2. Signal Detection Schemes	78
6.2.1. DC-Readout	78
6.2.2. Homodyne Detection	80
6.3. Optical Parameter Discussion for the Interferometer	81
6.3.1. Impact of the Contrast	81
6.3.2. Internal losses	83
6.3.3. Interferometer Cavity Design Considerations	86
6.3.4. Membrane Properties Requirements	87
6.4. Chapter Conclusion	89
7. Realized Interferometers at Cryogenic Temperatures	91
7.1. Quasi-Monolithic Interferometer of Invar	95
7.1.1. Optical Mounting	95
7.1.2. Spacer	97
7.1.3. Measurement at 10 Kelvin	99
7.1.4. Conclusion	100
7.2. Electric adjustable Interferometer of Copper	101
7.2.1. Interferometer Design	101
7.2.2. Interferometer Alignment Process	104
7.2.3. Measurement Results	105
7.2.4. Conclusion	109
7.3. Adjustable cooled Interferometer of Invar	110
7.3.1. Robust and Adjustable Interferometer Design	111
7.3.2. Optimized Interferometer Alignment Process	114
7.3.3. Measurements	116
7.3.4. Conclusion	118
8. Conclusion	119

B. Appendix	123
B.1. Material Properties	123
Bibliography	127
List of Publications	135
Acknowledgements	139
Curriculum Vitae	141

List of Abbreviations

- AC** alternating current
- AR** anti-reflective
- BS** beam splitter
- CAD** computer aided design
- CCD** Charge-Coupled Device
- CVIP** Cryo Vibration Isolation Platform
- DC** direct current
- LN** technical laser noise
- LND** laser noise detection
- LO** local oscillator
- MLI** Multilayer Insulation
- PD** photo diode
- RIN** Relative Intensity Noise
- RPN** radiation pressure noise
- SN** shot noise
- SQL** standard quantum limit
- SRM** signal-recycling mirror
- TN** thermal noise

List of Figures

2.1. Michelson-Sagnac Interferometer	21
2.2. Displacement Spectral Density of Quantum Noise	25
2.3. Displacement Spectral Density of Thermal Noise	26
3.1. Michelson-Sagnac Interferometer with Signal-Recycling	32
3.2. Transmitted Power of Signal-Recycled Interferometer	33
3.3. Signal-Recycling Mirror Detuning	34
3.4. Membrane Detuning in the Interferometer Cavity	35
3.5. Beam Splitter Unbalancing and Contrast Effects	36
3.6. Internal Power Enhancement in the interferometer Cavity	37
3.7. Displacement Noises of a Signal-Recycled Interferometer	38
4.1. Signal-Recycled Michelson-Sagnac Interferometer Setup	45
4.2. Measured Cavity Linewidth for Various Detunings	47
4.3. Reduced Thermal Noise with Optical Cooling	49
4.4. Generalized Optomechanical Coupling Measurement	50
4.5. Cooling on Cavity Resonance Versus Input Power	51
5.1. Thermal Conductivity for Various Materials	58
5.2. Thermal Contraction for Various Materials	61
5.3. Specific Heat for Various Materials	62
5.4. Vacuum System	63
5.5. Refrigerator System	65
5.6. Modification at Cryostat	68
5.7. Vibration Damping Stage	70
6.1. Detection scheme for cryogenic interferometer	79
6.2. Displacement Spectrum with laser noise subtraction	80
6.3. RIN measurement	82
6.4. Beam Splitter Characterization	85
6.5. Calculated Spectrum with Experimental Parameters	88
6.6. Calculated Improved Spectrum with Experimental Parameters	89
7.1. Quasi-Monolithic Interferometer	95
7.2. Thermal Simulation of Quasi-Monolithic Interferometer	98
7.3. Electric Adjustable Copper-Interferometer	101
7.4. The Membrane Positioning Stack	103
7.5. New Concept for Steering Mirror Mounting	104
7.6. Displacement Spectrum at 293 K and 10 K	107

LIST OF FIGURES

7.7. Modal Frequency Analysis	109
7.8. Adjustable Cooled Interferometer of Invar	110
7.9. Steering Mirror Mounting to Invar Spacer	112
7.10. Interferometer Setup in the Cryostat	116
7.11. Cooling of the Interferometer	117

1

Chapter 1.

Introduction

A photon that is reflected by an object transfers a momentum to it due to the conservation of momentum. The momentum of one photon is $p = \hbar k$ with the wave number $k = \omega/c$ where ω is the wavenumber and c the speed of light. The total momentum of a continuous light field with an average power P results in an effective radiation pressure force $F = 2P/c$ acting onto the reflecting object. This force was already postulated in the 17th century by Kepler [Asp14]. The first experimental observation of radiation forces were done with a light mill configuration by P. Lebedew, E.F. Nichols and G.F. Hull in 1901 [Leb01, Nic01]. For example a light field with a power of 1 W would only generate a force of ≈ 7 nN. In general, to make this weak optomechanical interaction between light field and a reflecting object visible one has to use high power and movable mirrors with high reflectivity and low mass. The momentum transfer of photons to atoms for example was experimentally observed by Frisch in 1933 [Fri33].

The development of laser sources, started by T. H. Maiman in 1960 [Mai60], has provided highly monochromatic, frequency stable, and high power light fields. The application of laser light boosted the investigation of optomechanical coupling between the light field and movable objects. Since then, mainly coupling to small objects was investigated and demonstrated in many different experiments. As for example it was shown that laser light could be used as an optical trap [Ash78], and for optical cooling of atoms and ions [Hä75, Ste86].

In those days also the optomechanical coupling to macroscopic (large) objects was analyzed and investigated by Braginsky et al. in the context of interferometric setups, as for example gravitational-wave detectors [Man67, Man77, Vor]. The optomechanical coupling in such interferometers can be distinguished in two radiation pressure force effects: the dynamical radiation pressure force (i.e. dynamical back-action) and the radiation pressure noise (i.e. quantum quantum coupling).

Dynamical Radiation Pressure Force

Dynamical radiation pressure forces only appear in the environment of an optical cavity with a movable mirror [Asp14, Che13, Mey13]. In such cavities the displacement of the mirror dynamically changes the power of the cavity light field. Since the radiation pressure force depends on the power the mirror displacement will follow the power variation, which again induces a power changes. This generates a dynamical optomechanical coupling of the optical and mechanical degrees of freedom [Saw15]. Dynamical optomechanical coupling arises from two different mechanisms. First, the motion of the mirror changes the cavity resonance frequency (i.e. cavity length), which is known as the dispersive coupling [Asp14]. Second, the displacement of the mirror changes the linewidth of the cavity (i.e. coupling to the thermal bath). This is the so called dissipative coupling [Els09]. Up until now, optomechanical systems were mainly dominated by dispersive coupling. Due to this coupling effect small mechanical oscillators could be cooled down to their ground state [Cha11]. Cooling of an object to its ground state via dispersive coupling requires a cavity linewidth which have to be smaller than the mechanical frequency (resolved sideband regime), which it is very demanding for the low frequencies of macroscopic and heavy objects. For dissipative coupling this condition is not required and it was shown in [Els09] that in principle even heavy macroscopic oscillators could be cooled into their ground states. In [Tar13, Vos14] it was shown that in a gravitational-wave detector operating close to dark port both optomechanical mechanism were present. Due to a generalized optomechanical coupling, which means the presence and interference of dispersive and dissipative coupling, it is possible to produce a stable optical spring inside the gravitational-wave detector. This could lead to an increased sensitivity even beyond the SQL.

In [Tar13] the generalized optomechanical coupling was also modeled for a signal-recycled Michelson-Sagnac interferometer containing a silicon nitride membrane as mechanical oscillator [Saw12, Kau13].

Radiation Pressure Noise

The second mentioned radiation pressure force effect is radiation pressure noise. Due to Heisenberg's uncertainty relation the number of photons in a laser light field is uncertain [Hei27], which results in shot noise. Therefore the radiation pressure force is also fluctuating and is know as the radiation pressure noise (RPN). It was shown by [Cav80] that RPN and shot noise on the photo diode form a limit on how accurate the position of free test masses in an interferometer can be measured with laser light. The limit is well know as the "*standard quantum limit*" (SQL). While the observation of shot noise is easy, at least for weak light fields, the observation of the RPN is much harder and requires a setup with low thermal noise and high displacement sensitivity as for example gravitational-wave detectors [Abr92, Abb09]. In [Buo01, Har10] it was argued that the second generation "*advanced LIGO*"

of the gravitational-wave detector LIGO will be limited by radiation pressure noise in the frequency range of 10 Hz-40 Hz.

While on one hand the observation and investigation of this quantum noise were motivated by gravitational-wave detectors, it is on the other hand also interesting from the fundamental physics point of view. Reaching the SQL opens new investigations in fundamental physics as for example optomechanical and pure mechanical entanglement of macroscopic objects [Vit07, ME08]. To reach this quantum regime it was suggested in [Yam10] to realize a table top experiment with a small silicon nitride membrane (mechanical oscillator) in a Michelson-Sagnac interferometer, which is comparable to the topology of the gravitational wave detectors. It was shown that the radiation pressure noise is in principle observable by cooling down this interferometer to cryogenic temperatures and by implementing signal-recycling similar to the signal enhancement in a gravitational wave detector [Mee88]. In [Fri11, Wes12, Kau12] first sensitivity measurements of such a Michelson-Sagnac interferometer were presented. Since this measurements were done without signal-recycling and at room temperature they were limited by shot noise and thermal noise. In later works [Kau13, Saw12] also a signal-recycled Michelson-Sagnac interferometer was realized and investigated. So far this experiment was still limited by thermal noise and shot noise, as it operated at room temperature. Towards the RPN this interferometer had to be cooled down.

The research described in this thesis was motivated by the dynamical optomechanical coupling as well as by the radiation pressure noise which both are in principle present in a signal-recycled Michelson-Sagnac interferometer. The first half of the thesis concentrated onto the observation and its characterization of the generalized optomechanical coupling (dynamical coupling). The second half of the thesis focused onto the design and realization of a new Michelson-Sagnac interferometer and characterization at cryogenic temperatures, as it is required for the observation of radiation pressure noise.

This thesis is structured as following:

- **Chapter 2** gives a short overview of the principles of a Michelson-Sagnac interferometer.
- In **Chapter 3** the impact of the signal-recycling mirror to the radiation pressure noise and the dynamical optomechanical coupling in such topology are described.
- The observation of the generalized optomechanical coupling is presented in **Chapter 4**.
- **Chapter 5** is the beginning of the second half of the thesis, and explains the cryocooler concept utilized.

1. Introduction

- In **Chapter 6** the required and achieved parameters of the interferometer are discussed with respect to the targeted observation of radiation pressure noise.
- The realization and characterization of new interferometers at cryogenic temperatures are shown in **Chapter 7**.
- **Chapter 8** summarizes the results of the thesis and gives a short outlook.

2

Chapter 2.

Principles of the Michelson-Sagnac Interferometer

This chapter describes the principles of the Michelson-Sagnac interferometer. First the characteristics of the utilized silicon nitride membrane are explained. Then the topology of the Michelson-Sagnac interferometer with the silicon nitride membrane is presented and at the end the relevant noise contributions are calculated and explained.

2.1. Silicon Nitride Membrane

Since the optomechanical coupling, due to radiation pressure force is very small, the mass, reflectivity and the mechanical quality factor of the mechanical coupling mirror have a high impact to the displacement of the mirror induced by the photons momentum transfer. To provide a high optomechanical coupling various mechanical oscillators [Kip08] have been used in the past in optomechanical systems, as for example a 1 g mirror [Cor07], atomic-force-mirror spring [Kle06], silicon toroid [Kip05], silicon nitride (SiN) membrane [Zwi08], etc. In this thesis a SiN membrane was used. Since a detailed explanation of the silicon nitride membrane used in the Michelson-Sagnac interferometer can be found in [Wes09, Saw12, Kau13, Fri11], this section only give an overview of the parameters of the utilized membranes during this thesis.

Membrane Dimensions

The silicon membranes used in this thesis had a surface of 1.5×1.5 mm size and a thickness d_m between 40 nm-75 nm, which result in a very low effective mass of $m_{\text{eff}} \approx 100$ ng [Wes09]. The square frame of the membrane was made

2. Principles of the Michelson-Sagnac Interferometer

out of silicon and had an edge length of 5 mm. This dimensions lead to an frequency ≈ 150 kHz for the fundamental mode.

Mechanical Quality-factor

The mechanical quality-factor is a important characteristic of the membrane. The quality-factor is characterize the coupling of the membrane to the environment. It is a measure of energy dissipation

$$E(t) = E_0 e^{-\frac{\omega_m t}{Q}}. \quad (2.1)$$

with the initial energy E_0 and the time $t = Q/\omega_m$ when the energy drops to $1/e$. The higher the Q-factor is the better is the decoupling of the membrane. In general in an optomechanical coupling experiment the Q-factor is required to be as high as possible. If an oscillator has an high quality factor, it results in a high and narrow resonance peak. In hat case the most motion energy is stored at the resonance frequency. For frequencies off resonance the motion amplitudes are very small. They decrease even more if the Q-factor increases. Thereby the higher the Q-factor the lower is for example the thermal noise excitation for frequencies off resonant. The Q-factor of an oscillator can be determined by

$$Q_{\text{vis}} = \frac{K_m \omega_m}{\Gamma_m} = \frac{m \omega_m}{\Gamma_m}, \quad Q_{\text{st}} = \frac{1}{\phi}. \quad (2.2)$$

where $K_m = \omega_m m$ is the characteristic of the spring, which is given by the oscillators frequency ω_m and mass m , and Γ_m and ϕ are the viscous and structural damping of the membrane [Wes09]. Typically the Q-factor for the SiN membrane is about $Q=10^5-10^6$ at room temperature. At cryogenic temperature the Q-factor increases by approximately one order of magnitude [Zwi08].

2.1.1. The oscillator transfer function

If a damped harmonic oscillator is driven by an external force F_{ex} the motion equation, according to the Newton's 2nd law, is

$$\ddot{x}(\omega) + \Gamma_m \dot{x}(\omega) + K_m(1 + i\phi)x(\omega) = \frac{F_{\text{ex}}(\omega)}{m}. \quad (2.3)$$

From this equation the complex transfer function can be deviated to

$$\chi_m(\omega) = \frac{x(\omega)}{F_{\text{ex}}(\omega)} = \frac{1}{(K_m - m\omega^2) + i(\Gamma_m\omega + K_m\phi)}. \quad (2.4)$$

For very high Q-factor $1 \ll Q$ the viscous and structural damping is almost equal. Since this is the case for the membranes used during this thesis, the real part of the transfer function is

$$\chi_m(f) = \frac{1}{(2\pi f_m)^2 m} \frac{1}{\sqrt{(1 - \frac{f^2}{f_m^2})^2 + (\frac{f}{Q f_m})^2}} \quad (2.5)$$

with $\omega_m = 2\pi f_m$.

Optical Characteristics

According to [Fri11] the amplitude reflectivity r_m of the membrane is

$$r_m = -\frac{(n_2^2 - 1) \sin(k_L n_2 d_m)}{2in_2 \cos(k_L n_2 d_m) + (n_2^2 + 1) \sin(k_L n_2 d_m)}, \quad (2.6)$$

where $k_L = 2\pi/\lambda$ is the wave number and λ the wavelength of the light field, $n_1 = 1$ is the refraction index of vacuum and $n_2 = 2.17$ [NOR12] the refraction index of SiN. Therefore the reflectivity depends on the thickness and the used laser wavelength. Since the used wavelength was 1064 nm and 1550 nm and the thickness varied from 40 nm-75 nm this result in a power reflectivity of $0.12 < r_m^2 < 0.175$.

The optical absorption was investigated in [Fri11, Ste13]. It was shown that the absorption for wavelength of 1064 nm and 1550 nm only were in a range of a few ppm. Therefore the heating due to absorption can be neglected.

2.2. Topology

In general a Michelson interferometer is very useful for high precision measurements. Due to the interference at the beam splitter the change of an arm length (motion of a mirror) can be monitored with an high accuracy. Since the membrane has an expected reflectivity of only $<20\%$ the membrane could not be used as an end mirror in a Michelson interferometer, because of the losses due to membrane transmission (cf. figure 2.1-(a)). Because of that

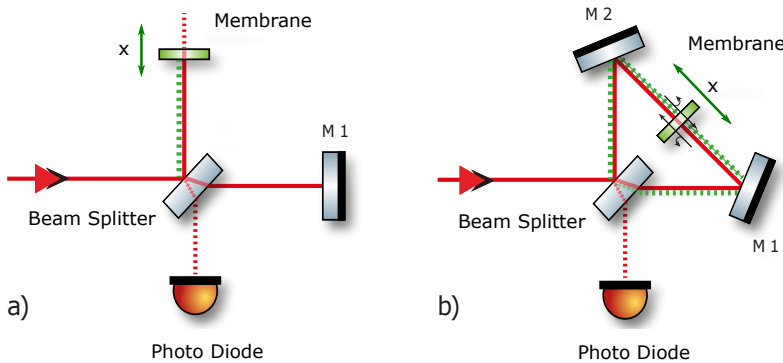


Figure 2.1.: *Michelson-Sagnac Interferometer.* (a) presents the membrane as an end mirror of a Michelson interferometer. Due to the low reflectivity the losses are very high. In (b) the membrane a common end mirror of both Michelson modes. The reflected light form the Michelson modes and the transmitted light field the the Sagnac modes.

it was suggested in [Yam10] to use a Michelson-Sagnac topology as shown in figure 2.1-(b). Here the membrane was used as a common end mirror of

2. Principles of the Michelson-Sagnac Interferometer

both Michelson modes. The transmitted power forms the Sagnac modes. In contrast to the simple Michelson interferometer the transmitted power is in principle not lost, because the Sagnac mode performs as a simple mirror. It reflects all the incoming light back to the port from where it came from. If now an additional mirror would be positioned in the output port or input port the light field would again be reflected back into the interferometer and not lost. Due to the transmission the Sagnac mode is independent of the position of the membrane. So when the membrane moves only Michelson mode can be used to measure the membrane's motion. The resulting output power of a Michelson-Sagnac interferometer is [Saw12]

$$\begin{aligned}
 P_{\text{out}}(x) &= |a_{\text{t,ifo}}|^2 \\
 &= |a_{\text{in}}|^2 \left| \underbrace{t_m e^{i2kl}(r_{\text{bs}}^2 - t_{\text{bs}}^2)}_{\text{Sagnac-Mode}} + \underbrace{r_{\text{bs}} t_{\text{bs}} r_m 2e^{i2kl} \cos(2kx \pm \frac{\pi}{2})}_{\text{Michelson-Mode}} \right|^2, \quad (2.7)
 \end{aligned}$$

where r_{bs} and t_{bs} are the amplitude reflectivity and transmissivity of the beam splitter, l is the Michelson arm length (beam splitter to membrane) and $k = 2\pi/\lambda$ is the wave number with λ as wavelength. The output power depends on the membrane displacement x . The maximum transmitted power is given by $P_{\text{max}} = P_{\text{in}} r_m^2$. For a perfect interferometer the minimum transmitted power is 0. The Michelson-Sagnac interferometer can also be seen as a compound mirror with tunable reflectivity and transmissivity [Saw12, Kau13]

$$\begin{aligned}
 r_{\text{ifo}}^2(x) &= \frac{P_r(x)}{P_{\text{in}}} \\
 t_{\text{ifo}}^2(x) &= \frac{P_{\text{out}}(x)}{P_{\text{in}}}
 \end{aligned} \quad (2.8)$$

where for a lossless interferometer $P_{\text{in}} = P_r(x) + P_{\text{out}}(x)$ is. According to [Tar13] the complex interferometer reflectivity and transmissivity are

$$\begin{aligned}
 \mathcal{R}_{\text{ifo}}(x) &= r_m (t_{\text{bs}}^2 e^{i k x} - r_{\text{bs}}^2 e^{-i k x}) - 2t_m r_{\text{bs}} t_{\text{bs}} \\
 \mathcal{T}_{\text{ifo}}(x) &= r_m t_{\text{bs}} r_{\text{bs}} (e^{i k x} - e^{-i k x}) + r_m (t_{\text{bs}}^2 - r_{\text{bs}}^2).
 \end{aligned} \quad (2.9)$$

In the following mostly the absolute value of the interferometer reflectivity $r_{\text{ifo}}(x) = |\mathcal{R}_{\text{ifo}}(x)|$ and transmissivity $t_{\text{ifo}}(x) = |\mathcal{T}_{\text{ifo}}(x)|$ is used. At the dark port ($x=0$) [Saw12] the $r_{\text{ifo}}(0) = 1$ and $t_{\text{ifo}}(0) = 0$.

Contrast

The above equations are assuming a perfect interferometer without losses. But in the real interferometer optical losses are present and the alignment is

not perfect. A characteristic value which describes this non perfect interferometer is the contrast \mathcal{C} . The contrast describes the quality of the alignment. This lead to the effective interferometer reflectivity and transmissivity

$$\begin{aligned} r_{\text{ifo,eff}}^2(x) &= r_{\text{ifo}}^2(x)\mathcal{C} \\ t_{\text{ifo,eff}}^2(x) &= 1 - r_{\text{ifo,eff}}^2(x) \end{aligned} \quad (2.10)$$

For a perfect interferometer the contrast is $\mathcal{C} = 1$. For the non perfect case the contrast can be determined by the measurement of a fringe [Wes09] and is $\mathcal{C} < 1$.

2.3. Noise Sources

As mentioned in the introduction the long-term goal of the Michelson-Sagnac interferometer is the detection of the RPN (radiation pressure noise). But in general the measured output power of the interferometer was a superposition of the RPN and other noise budgets. The significant noise budgets, which were influencing the measurements of this thesis, were SN (shot noise), radiation pressure noise (RPN), TN (thermal noise) and LN (technical laser noise). In the following sections the noise sources are described, the formula for calculations are presented and also their impact is discussed.

2.3.1. Shot Noise

Due to the Heisenberg uncertainty principle the amplitude of every monochromatic light field is fluctuating over time. So every detected power in the output of the interferometer has a fundamental quantum fluctuation, the so called shot noise. Due to [Ede78] the linear spectral density of this noise can be written as

$$S_{\text{sn}} = \sqrt{\frac{4\pi\hbar c P_{\text{out}}(x)}{\lambda}} = \sqrt{\frac{4\pi\hbar c P_{\text{in}} r_m^2 \sin^2\left(\frac{4\pi}{\lambda}x\right)}{\lambda}}, \quad (2.11)$$

with the interferometer output power $P_{\text{out}}(x)$ (see equation 2.7), the wavelength λ , the Planck's constant \hbar and c as speed of light. Although the shot noise fluctuations are not induced by membrane displacement, shot noise and the real signal not distinguishable in the output of the interferometer. But they depend differently on the input power. With increasing output power the shot noise increases with $\sqrt{P_{\text{in}}(x)}$. Whereas a signal $\delta P_{\text{out}}(x)/\delta x$, which is induced by membrane displacement δx , is proportional to P_{in} . One could compare both with the signal normalization of the shot noise, which is given by

$$\frac{S_{\text{sn}}}{\delta P_{\text{out}}(x)/\delta x} = \sqrt{\frac{\hbar c \lambda}{16\pi P_{\text{in}} r_m^2 \cos^2\left(\frac{4\pi}{\lambda}x\right)}}. \quad (2.12)$$

2. Principles of the Michelson-Sagnac Interferometer

At the dark fringe $x = \lambda/4$ this ratio is at its minimum and can be written as

$$\frac{S_{sn}}{\delta P_{out}(x)/\delta x} = \sqrt{\frac{\hbar c \lambda}{16\pi P_{in} r_m^2}}. \quad (2.13)$$

This equation shows that for a given laser wavelength λ and membrane power reflectivity r_m^2 the impact of the shot noise to the signal measurement could be reduced by increasing the input power. A different technique, which decreases the signal-normalized shot noise is to send a squeezed vacuum light field into the interferometer through the output port. This was shown in various table-top interferometer setups [Vah05, Meh10] and in the gravitational-wave detector GEO600 [Col11, Gro13]. It also should be mentioned that the shot noise is the only of the four noises which is frequency independent for a Michelson-Sagnac interferometer without cavity (i.e. signal recycling).

2.3.2. Radiation Pressure Noise

Radiation pressure noise (RPN) is the second quantum mechanical noise budget and is induced by shot noise in the interferometer arms. RPN is due to the momentum transfer of the photons to the membrane. Since the photon number fluctuates, as mentioned in previous section, the momentum transfer also changes over time. The RPN is an anti-correlated momentum fluctuation [Cav80], so that the momentum on both sides of the membrane do not cancel each other out, as it is true for a DC light power in both arms. Although this momentum is very small it causes a fluctuation of the membrane displacement, which results in an amplitude fluctuation (noise) at the interferometer output port. According to [Yam10] the linear spectral density of the displacement can be written as

$$S_{rpn}(f) = \chi_m(f) \sqrt{\frac{16\pi \hbar r_m^2 P_{in}}{c \lambda}}, \quad (2.14)$$

where $|\chi_m(f)|$ is the transfer function of the membrane from equation 2.5. Because of this force susceptibility the RPN is frequency dependent. According to the transfer function, reducing the mass of the membrane increases the RPN. But also an increasing input power would increase the RPN as it is proportional to $\sqrt{P_{in}}$. Generally this effect is seen as limiting noise, as for example in the "Advanced LIGO" [Har10] simulations where the RPN will limit the sensitivity at low frequencies. But as it is the goal to measure the RPN with the signal-recycled Michelson-Sagnac interferometer, it was interpreted as signal in this thesis.

The superposition of shot noise and radiation pressure noise is often simply called quantum noise. Figure 2.2 shows the calculated quantum noise for a membrane resonance frequency of 150 kHz. For an input power of 3 W the

interferometer output spectrum is shot noise limited, whereas the RPN is about 3 orders of magnitude below at frequencies <150 kHz. As the power increase to 3 kW the spectrum is dominated by the RPN. The minimum of

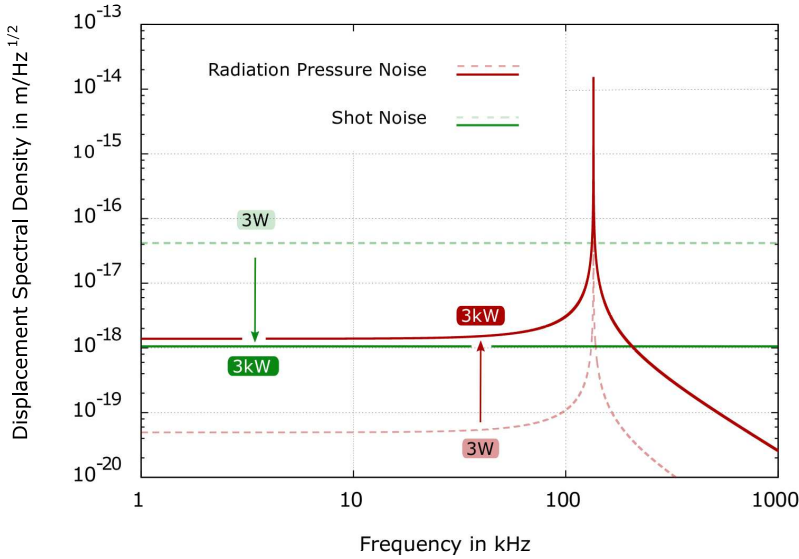


Figure 2.2.: Displacement Spectral Density of Quantum Noise. For an input power of 3 W is the shot noise almost 3 orders of magnitude above the radiation pressure noise. By increasing the input power to 3 kW the spectrum is limited by radiation pressure noise for frequencies around and below the membrane resonance frequency of 150 kHz.

this the uncorrelated sum is known as the *Standard Quantum Limit* (SQL) [Ede78]. But this limit can be suppressed by coupling squeezed light states into the interferometer [Kim01].

2.3.3. Thermal Noise

Thermal noise is usually a non negligible noise budget. Thermal noise is based on the Fluctuation-Dissipation Theorem [Nyg28] and can be divided in at least three categories. The three thermally influenced noises are thermal refractive noise [Bra01], thermal coating noise [Cro04] and Brownian thermal noise [Li99]. Since the thermal contribution in the Michelson-Sagnac interferometer with SiN membrane is totally dominated by Brownian thermal noise [Saw12] only this one will be considered. The Brownian thermal noise describes the internal random motion of particles of optical components, as the mirrors and the membrane. Since the membrane is much lighter than the other optical parts its Brownian thermal noise is the crucial thermal effect inside the interferometer. This thermal noise of the membrane is due to the viscous and structural damping of the membrane which leads to the energy dissipation. A more detailed description can be found

2. Principles of the Michelson-Sagnac Interferometer

in [Wes09, Saw12, Kau13]. As the two effects are quite similar for high mechanical quality-factor, it was sufficient for this thesis to consider just the thermal noise due to the viscous damping. In general this thermal noise causes a displacement fluctuation of the membrane which depends on the membranes temperature. These position fluctuations cause an amplitude fluctuation due to the interference of the two light fields in the interferometer arms, which can be measured with the PD (photo diode). The linear displacement spectral density can be calculated according to [Sau90, Jen98]

$$S_{tn}(f) = |\chi_m(f)| \sqrt{4k_B T \frac{m f_m^2}{f Q}}, \quad (2.15)$$

where m is the mass of the membrane, f_m the resonance frequency of the membrane, T the temperature, Q the mechanical quality factor of the membrane, k_B the Boltzmann constant and $|\chi_m(f)|$ the transfer function of the membrane. Figure 2.3 compares the displacement spectral density of the thermal noise to the above mentioned quantum noise. Even if the input power would be at 3 kW the spectrum would be thermal noise limited at room temperature. One have to reduce the temperature to about 1 K to have the possibility to observe the radiation pressure noise. Beside the reducing the temperature of the membrane the thermal noise also could be decreased by higher a Q-factor, lower mass and lower resonance frequency. A discussion of realistic values is done in section 6.3.

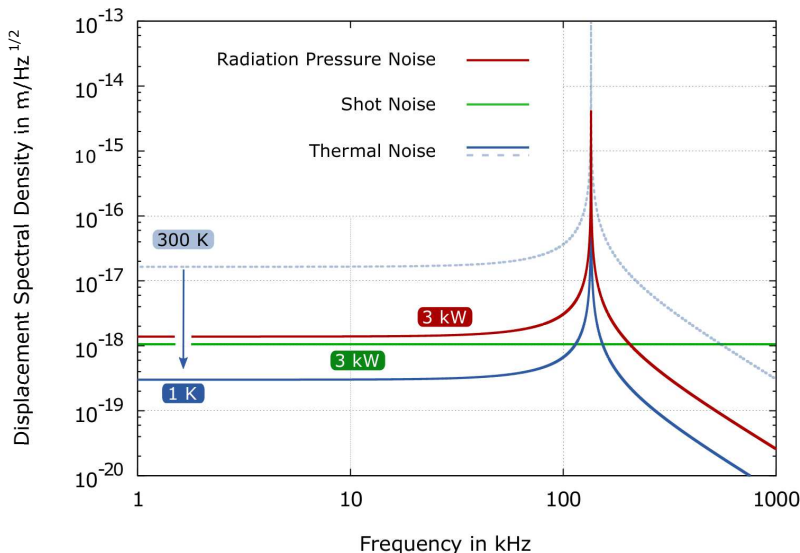


Figure 2.3.: Displacement Spectral Density of Thermal Noise. At room temperature the spectral density at the interferometer's output is limited by the thermal noise. By reducing the temperature of the membrane to 1 K the thermal noise decreases so that the radiation pressure noise could be observed.

2.3.4. Technical Laser Noise

Every laser system introduces classical laser noise to the experiment. This noise can be divided into two different types of noise. On the one hand there is frequency noise and on the other hand amplitude noise. A detailed analysis of the impact of the laser noise in a Michelson-Sagnac interferometer and the suppression of the same, can be found in the thesis of H. Kaufer [Kau13]. The information given in this section is basically a summary of the analysis presented there.

Frequency Noise

The effect of the frequency noise highly depends on the unequal length of the interferometer arms. For an arm length difference of 0.1 mm this noise is approximately 1-2 orders of magnitude below the above described noise budgets. As in all interferometer setups presented in this thesis, the membrane was positioned by positioners with a precision of a few nm, the influence of frequency noise could be avoided.

Amplitude Noise

The amplitude noise of a laser system is characterized by the *relative intensity noise* (RIN). The RIN is frequency dependent and given by the ratio of power fluctuation to average measured power P . Figure 6.3 presents for example the measured RIN for the 1550 nm Koheras Boostik C-15 laser system, which was used for the cryogenic interferometer experiments. The RIN at the membrane's resonance frequency around 150 kHz of the 1550 nm Koheras Boostik C-15 laser system was about $4.4 \cdot 10^{-7} 1/\sqrt{\text{Hz}}$. The impact of classical laser intensity noise to the measurement in the output of the interferometer depends on two different effects. The first effect is quite similar to the quantum natured RPN. The classical intensity fluctuation induces a fluctuation force to the membrane which displaces the membrane. But in contrast to the quantum noise effect, the classical force fluctuations are correlated. This means that for a perfectly balanced beam splitter the classical force fluctuations would cancel itself out. According to [Kau13] the displacement spectral density can be written as

$$S_{\text{in}} = \frac{2}{c} \chi_m(f) r_m^2 \Delta_{\text{bs}} S_{\text{in}}^P \quad (2.16)$$

with the power fluctuation spectral density

$$S_{\text{in}}^P = P \cdot \text{RIN} \quad (2.17)$$

with P as the average detected power. For a high output power the technical laser noise increases and could mask the quantum noise. To provide a quantum limited measurement the following condition has to be fulfilled

2. Principles of the Michelson-Sagnac Interferometer

[Kau13]:

$$\frac{S_{sn}}{S_{ln}^P} > 1 \Leftrightarrow \sqrt{\frac{4\pi\hbar c}{\lambda}} > \Delta_{bs}\sqrt{P} \cdot \text{RIN}. \quad (2.18)$$

Since the laser RIN produces correlated noise in the interferometer arms it will be suppressed by the unbalancing factor Δ_{bs} , with T_{bs} and R_{bs} the power transmissivity and reflectivity of the beam splitter. At the wavelength of 1550 nm this results in

$$5 \cdot 10^{-10} \sqrt{\frac{W}{Hz}} > \Delta_{bs}\sqrt{P} \cdot \text{RIN} \quad (2.19)$$

The crucial parameters in the interferometer design for the laser noise induced force fluctuation which drives the membrane are the total power used and the balancing for the beam splitter. The second impact of laser intensity noise to the measurement is the detected amount of power. It also effects the shot noise (compare equation 2.11). Especially for higher detected power the measurement spectra would be masked by the laser noise. Higher power could be caused, for example, by an non perfect contrast or by positioning the membrane slightly off dark fringe. According to equations (2.11) and (2.17) the condition for a quantum limited measurement with the detected power P_{out} is

$$S_{sn} > S_{ln}^P \Rightarrow \sqrt{\frac{4\pi\hbar c P_{out}}{\lambda}} > P_{out} \cdot \text{RIN} \quad (2.20)$$

Since laser noise increases with $\sqrt{P_{out}}$ faster then shot noise, one have to reduce the the detected power to get a quantum limited measurement. This can be done by increasing the contrast and measuring close to dark fringe or even at the dark fringe depending on the ratio of $S_{sn}/S_{ln}^P > 1$. A different possibility for laser noise reduction is the power stabilization of the laser. Since this is not a topic of this thesis it is not discussed here. But this laser noise stabilization technique is well described in [Kau13].

2.4. Chapter Conclusion

Since the displacement noise due to radiation pressure noise is much smaller than shot noise and thermal noise (see figure 2.3) high powers of several kW are required to provide a RPN limited spectrum measurement. Beside the difficulty to handle such high power it also causes crucial issues. When using high input power the technical laser noise will increase and make a quantum limited measurement almost impossible. Additionally the interferometer alignment (contrast) would also decrease, as such high power causes a thermal lens of inside the transmitted beam splitter. Although the membrane has a very low absorption [Ste17], it might heat up and limit the cool down of the membrane down to a few Kelvin. Overall using a few kW inside

the table top Michelson-Sagnac interferometer is not realizable referring the detection of radiation pressure noise. The application of an additional mirror to enhance the signal could help here out. This so called signal-recycling cavity is described in the next chapter.

3

Chapter 3.

Signal-Recycled Michelson-Sagnac Interferometer

Signal-recycling in an interferometer setup gives the possibility to enhance the output signal without increasing the internal interferometer power. This was firstly suggested by Meers in 1988 [Mee88]. The idea was to use an additional mirror, a so called signal recycling mirror (SRM), at the output of the interferometer. The implementing of such an additional mirror into the special topology of the Michelson-Sagnac interferometer, suggested by [Yam10] and realized in [Kau13, Saw12], is an important step for the goal of observing the radiation pressure noise.

The beginning of this chapter describes the general basics of the interferometer cavity based on the Fabry-Perot cavity. The second section discusses the signal enhancement due to the signal-recycling mirror and the resulting displacement noise. In the last section the emphasis is on to optomechanical interaction inside the interferometer cavity.

3.1. Interferometer Cavity Basics

Since the interferometer can be seen as a compound mirror with reflectivity $r_{\text{ifo}}(x)$ and transmissivity $t_{\text{ifo}}(x)$, that are tunable due to the membrane position x (see section 2.2), the interferometer forms an optical cavity with the SRM. The topology of this signal-recycling cavity is shown in figure 3.1. The membrane and the signal-recycling mirror (SRM) are the two movable optical parts in the interferometer cavity, which can be displaced in direction of the light field propagation. The detuning x of the membrane and the detuning δl_{sr} of the SRM have a strong impact to the interferometer cavity

3. Signal-Recycled Michelson-Sagnac Interferometer

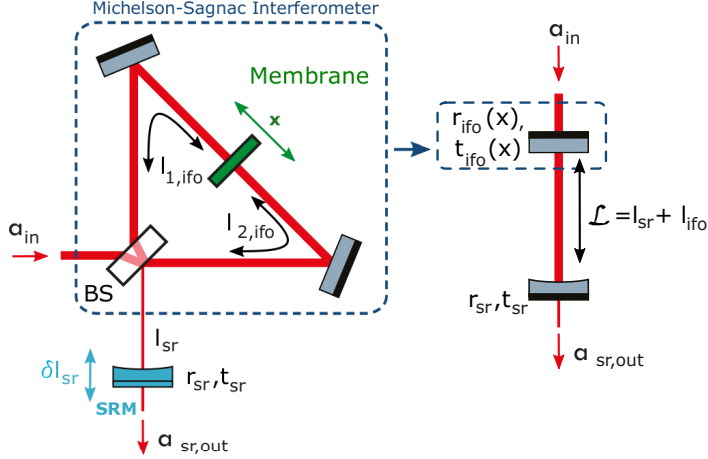


Figure 3.1.: *Michelson-Sagnac Interferometer with Signal-Recycling.* The Michelson-Sagnac interferometer (ifo) acts as a compound mirror with tunable reflectivity $r_{\text{ifo}}(x)$ and transmissivity $t_{\text{ifo}}(x)$, due to the membrane position x . An additional mirror (SRM) in the output port of the interferometer forms together with the interferometer an optical cavity. The total cavity length $\mathcal{L}(x, \delta l_{\text{sr}})$ depends on the membrane detuning x and the SRM detuning δl_{sr} and is the sum of the distance of the SRM to the beam splitter (BS) $l_{\text{sr}} \pm \delta l_{\text{sr}}$ and the interferometer arm length $l_{\text{ifo}}(x) = ((l_{1,\text{ifo}} + x) + (l_{2,\text{ifo}} - x))/2$.

output light field $a_{\text{sr},\text{out}}(x, \delta l_{\text{sr}})$, which can be written as

$$a_{\text{sr},\text{out}}(x, \delta l_{\text{sr}}) = a_{\text{in}} \frac{t_{\text{ifo}}(x) t_{\text{sr}} e^{ik_L \delta l_{\text{sr}}}}{1 - r_{\text{ifo}}(x) r_{\text{sr}} e^{i2k_L \delta l_{\text{sr}}}}, \quad (3.1)$$

with an incoupling light field a_{in} , the amplitude transmissivity t_{sr} and the reflectivity r_{sr} of the SRM, the tunable interferometer reflectivity $r_{\text{ifo}}(x)$ and transmissivity $t_{\text{ifo}}(x)$ (cf. section 2.2) and the laser carrier wave number $k_L = \omega_L/c = 2\pi/\lambda$. Figure 3.2 shows a 3D-plot of the normalized output power $P_{\text{sr},\text{out}}(x, \delta l_{\text{sr}})/P_{\text{in}}$ dependency on the membrane and SRM detunings.

3.1.1. Interferometer Cavity Detuning

The two parameters x and δl_{sr} change the effective length \mathcal{L} of the cavity. This effective cavity length \mathcal{L} is the sum of

$$\mathcal{L}(x, \delta l_{\text{sr}}) = l_{\text{sr}} + \delta l_{\text{sr}} + l_{\text{ifo}}(x), \quad (3.2)$$

with l_{sr} the distance of the beam splitter to the SRM, and $l_{\text{ifo}}(x) = ((l_{1,\text{ifo}} + x) + (l_{2,\text{ifo}} - x))/2$ the average arm length of the two Michelson interferometer arms. In contrast to the Fabry-Perot cavity the length of the interferometer cavity depends on two different displacements. Therefore the total frequency detuning Δ of the cavity is much more complex than of a simple Fabry-Perot cavity.

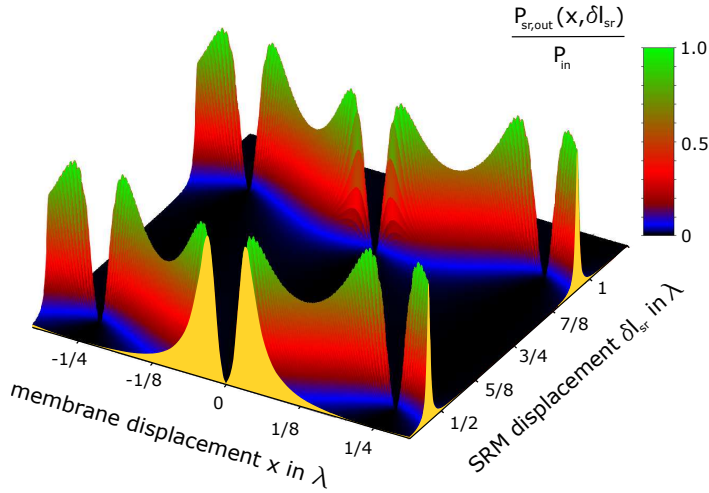


Figure 3.2.: Transmitted power of signal-recycled interferometer. The normalized transmitted power $P_{sr,out}(x, \delta_{sr})/P_{in}$ of the signal-recycled interferometer. The transmitted power is dependent on the membrane displacement x and the signal-recycling mirror (SRM) displacement δ_{sr}

For the signal-recycled Michelson-Sagnac interferometer this detuning Δ was calculated by [Tar13] as

$$\Delta = \underbrace{\omega_L - \omega_{cav}}_{=: \delta_{sr}} + \underbrace{(c/2\mathcal{L})\delta\phi}_{=: \delta_m}, \quad (3.3)$$

where ω_L is the laser frequency, $\omega_{cav} = c/\mathcal{L}(\pi n - 1)$ describes the resonant frequencies for the interferometer cavity and $\delta\phi = [\arg(\mathcal{R}_{ifo}(x)) - 2]$ with $\arg(\mathcal{R}_{ifo}(\lambda/4)) \approx 2$, where equation (2.9) describes $\mathcal{R}_{ifo}(x)$. δ_{sr} describes the detuning of the cavity resonance at interferometer dark port, and δ_m is the detuning of the membrane from dark port position.

Signal-Recycling Mirror Detuning

Figure 3.3 presents the normalized transmitted power $P_{sr,out}(x, \delta_{sr})/P_{in}$ dependent on the SRM detuning δ_{sr} for the three specific membrane detunings $x_1 = \lambda/8$, $x_2 = \lambda/16$ and $x_3 = \lambda/56$, which result due to equation (2.9) in the interferometer reflectivities $r_{1,ifo}^2 = 0.8$, $r_{2,ifo}^2 = 0.9$ and $r_{3,ifo}^2 = 0.99$. As in this calculation for the SRM the reflectivity r_{sr}^2 was set to 0.9, the interferometer is overcoupled for the case $r_{1,ifo}^2 < r_{sr}^2$, impedance matched for $r_{2,ifo}^2 = r_{sr}^2$ and undercoupled for $r_{3,ifo}^2 > r_{sr}^2$.

Membrane Detuning

Figure 3.4 displays the cross section of the output power 3D-plot, shown in figure 3.2), in direction of the membrane displacement axes. In contrast to a simple Fabry-Perot cavity this detuning does not change only the cavity length, but also the reflectivity of the compound interferometer mirror. For

3. Signal-Recycled Michelson-Sagnac Interferometer

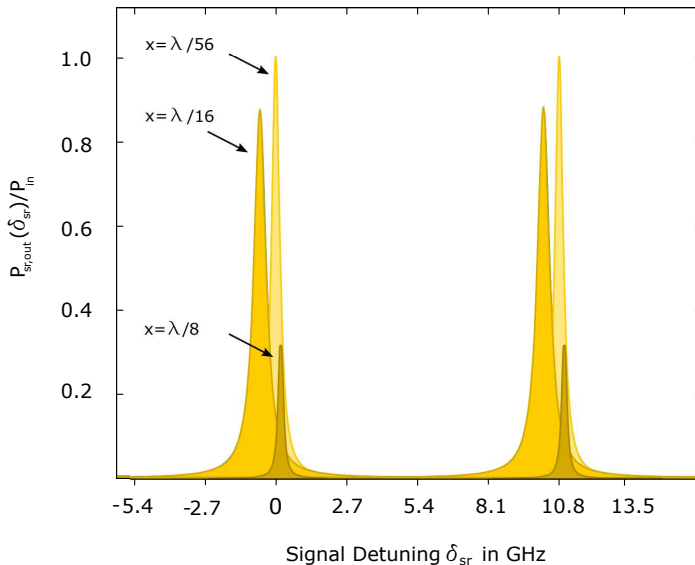


Figure 3.3: *Signal-Recycling Mirror Detuning.* The normalized transmitted power $P_{\text{sr,out}}(x, \delta_{\text{sr}})/P_{\text{in}}$ is shown in dependency of the signal-recycling mirror frequency detuning δ_{sr} for the three various membrane displacements $x_1 = \lambda/8$, $x_2 = \lambda/16$ and $x_3 = \lambda/56$. These displacements result in the interferometer reflectivities $r_{1,\text{ifo}}^2 = 0.8$, $r_{2,\text{ifo}}^2 = 0.9$ and $r_{3,\text{ifo}}^2 = 0.99$. The signal-recycling mirror reflectivity is set to $r_{\text{sr}}^2 = 0.9$.

a membrane position where $r_{\text{ifo}}^2(x) = r_{\text{sr}}^2$ the transmitted power is maximum and the cavity is impedance matched. As the plots are calculated for a perfect contrast $\mathcal{C} = 1$ (for $\mathcal{C} < 1$ see figure 3.5) the highest reflectivity of the interferometer is unity. Thereby for membrane detunings x with $r_{\text{ifo}}^2(x) > r_{\text{sr}}^2$ the cavity is undercoupled. For all other displacements the cavity is overcoupled. As the signal is going to be detected in transmission of the cavity, it is necessary to operate the cavity in the undercoupled regime, to avoid that a part of the signal is dissipating through the input port of the interferometer. For the impedance matched case only the half of the signal is transmitting the SRM. The other half is dissipating the cavity through the input port of the interferometer. The higher the undercoupling is the lower is the loss factor of the signal. In principle it is not lost, as one could detect it in the input port and add both detected half amplitude signals in both ports (input and output). Since this is complicate to realize experimentally, it was decided to detect the signal only in transmission of the cavity. Therefore it is important to have a highly undercoupled signal-recycling cavity. As the contrast describes the upper limit for the interferometer reflectivity, a high interferometer contrast is very important for the detection of RPN. Therefore the contrast should be at least above the SRM reflectivity. The impact of the contrast to the undercoupling range is shown on the right side of figure 3.5. The plots for various contrasts are done with a SRM reflectivity of

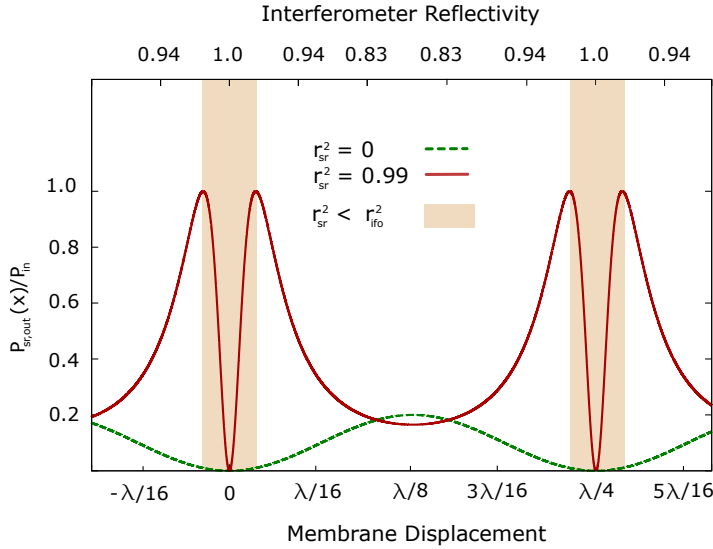


Figure 3.4.: *Membrane Detuning in the Interferometer Cavity.* The transmitted power $P_{\text{sr,out}}(x)$ of the signal-recycled interferometer is dependent on the membrane displacement x for various signal-recycling mirror reflectivities r_{sr}^2 . For both cases the cavity length is set to be $L_{\text{sr}} = n \lambda/2$, which is the resonance of the cavity transmission peak. Here also a perfect contrast $\mathcal{C} = 1$ is assumed. For $r_{\text{sr}}^2 = 0$ the output power is similar to the output power of the interferometer without a signal-recycling mirror. For $r_{\text{sr}}^2 < r_{\text{ifo}}^2$ the signal-recycling cavity is undercoupled.

$r_{\text{sr}}^2 = 0.99$. If the contrast is equal to the SRM reflectivity the undercoupling range vanishes and for higher contrasts the undercoupling range increases. The left side of figure 3.5 demonstrates the impact of an imbalanced beam splitter, which results in an asymmetric power transmission profile.

3.1.2. Interferometer Characteristics

The interferometer cavity can be characterized and compared to other cavities by the "half linewidth at half maximum" (HWHM) of the cavity and the free spectral range.

Interferometer Cavity Linewidth

The total "half linewidth at half maximum" (HWHM) γ of the interferometer cavity depends on the signal-recycling reflectivity r_{sr}^2 and the interferometer reflectivity $r_{\text{ifo}}^2(x)$. For $t_{\text{sr}}^2 \ll 1$ and $t_{\text{ifo}}^2(x) \ll 1$ the cavity linewidth γ is according to [Tar13]

$$\begin{aligned}
 \gamma &= \gamma_{\text{sr}} + \gamma_{\text{m}} \\
 &= \frac{ct_{\text{sr}}^2}{4\mathcal{L}} + \frac{ct_{\text{ifo}}^2(x)}{4\mathcal{L}} \\
 &= \frac{c}{2\mathcal{L}} (1 - r_{\text{sr}} r_{\text{ifo}}(x)).
 \end{aligned} \tag{3.4}$$

3. Signal-Recycled Michelson-Sagnac Interferometer

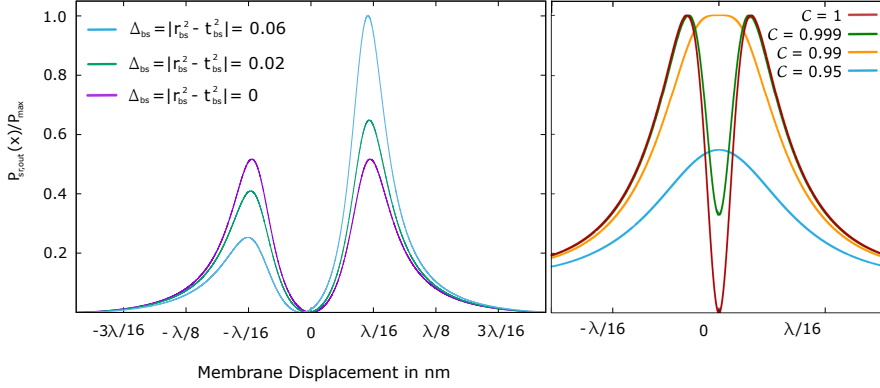


Figure 3.5.: *Beam Splitter Unbalancing Effects and the Contrast Impact on Transmitted Cavity Power.* Left: An unbalanced beam splitter results in an asymmetric behavior of the power transmission in dependency of the membrane displacement. Right: As the Contrast describes the maximal reachable reflectivity, the lower the contrast is the higher is the undercoupling range. For $r_{\text{sr}}^2 = r_{\text{ifo}}^2$ it is not possible to undercouple the cavity.

The membrane detuning dependency of the linewidth is the main difference of the interferometer cavity to a simple Fabry-Perot cavity. With the membrane displacement one can change the coupling rate of the cavity. In figure 3.3 it is visible that the linewidth changes for different membrane positions. This characteristic leads to an optomechanical coupling due to dissipation, which is described in section 3.3 and 4.

Free Spectral Range and Finesse

The *free spectral range* (FSR) describes the frequency distance of two cavity resonant peaks. The FSR is given by

$$\delta f_{\text{FSR}} = \frac{c}{2\mathcal{L}}, \quad (3.5)$$

with \mathcal{L} the cavity length being the only parameter. As the cavity length \mathcal{L} , however, depends on the membrane and the SRM detuning, this is also true for the FSR. The ratio of the FSR and the linewidth is the so called Finesse

$$\mathcal{F} = \frac{\delta f_{\text{FSR}}}{\gamma} = \frac{\pi}{\arcsin\left(\frac{1 - r_{\text{ifo}} r_{\text{sr}}}{2\sqrt{r_{\text{ifo}} r_{\text{sr}}}}\right)}. \quad (3.6)$$

which characterizes the spectral resolution of an optical cavity. For increasing mirror reflectivities the finesse is also increasing and the bandwidth of the cavity decreases. According to equation (3.4) the cavity linewidth also is proportional to $1/\mathcal{L}$.

3.2. Signal Enhancement and Noise Budget

While the maximum output power is equal to the input power, the internal cavity power could reach much higher values and is given by

$$P_{\text{sr,intra}} = \left| \frac{a_{\text{ifo,t}}}{a_{\text{in}}} \right|^2 \quad (3.7)$$

$$= \frac{t_{\text{ifo}}^2}{1 + r_{\text{ifo}}^2 r_{\text{sr}}^2 - 2\sqrt{r_{\text{ifo}}^2 r_{\text{sr}}^2} \cos(2kL)}.$$

The internal power enhancement also depends on the reflectivities of both mirrors and the maximum is given by $r_{\text{ifo}}^2 = r_{\text{sr}}^2$. Figure 3.6 shows the interferometer reflectivity dependent internal power enhancement for different reflectivity values. If the internal power is increased by the signal-recycling

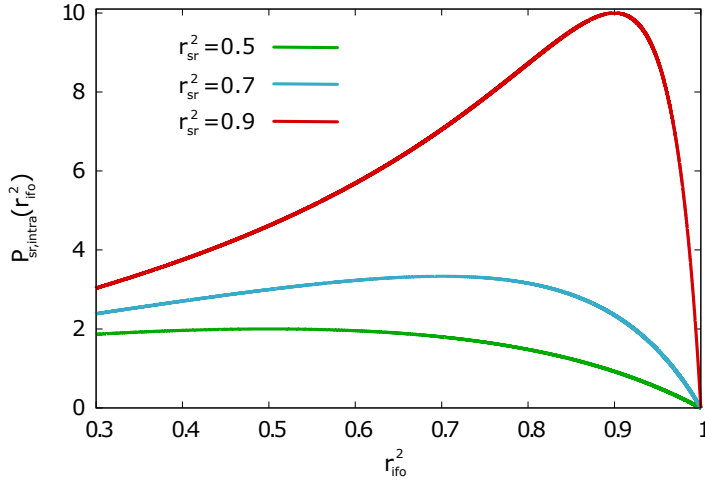


Figure 3.6: *Internal Power Enhancement in the Interferometer Cavity.* The internal power $P_{\text{sr,intra}}(\mathcal{L})$ is shown in dependency of the interferometer reflectivity r_{ifo}^2 . The internal power is maximal at $r_{\text{ifo}}^2 = r_{\text{sr}}^2$.

mirror, as shown in figure 3.6, this is also true for the internally induced signal, by membrane displacement. This effects the shot noise and the radiation pressure noise detection since those are power dependent. According to [Yam10] the displacement spectral density of these two noise budgets changes to

$$S_{\text{sn}}^{\text{sr}} = \sqrt{\frac{\hbar c \lambda}{16\pi \mathcal{G}_{\text{sr}} r_{\text{m}}^2 P_{\text{in}}}} \sqrt{1 + \left(\frac{f}{f_{\text{sr}}}\right)^2}, \quad (3.8)$$

$$S_{\text{rpn}}^{\text{sr}} = \chi(f) \sqrt{\frac{16\pi \mathcal{G}_{\text{sr}} r_{\text{m}}^2 P_{\text{in}}}{c \lambda}} \sqrt{\frac{1}{1 + \left(\frac{f}{f_{\text{sr}}}\right)^2}} \quad (3.9)$$

3. Signal-Recycled Michelson-Sagnac Interferometer

where \mathcal{G}_{sr} is the recycling gain factor

$$\mathcal{G}_{\text{sr}} = \frac{1 + r_{\text{sr}}}{1 - r_{\text{sr}}} \quad (3.10)$$

and f_{sr} the cutoff frequency of the cavity

$$f_{\text{sr}} = \frac{c(1 - r_{\text{sr}})}{4\pi(L_{\text{sr}} + L)} \quad (3.11)$$

for the condition that the recycling mirror amplitude reflectivity r_{sr} is close to unity and $r_{\text{sr}} < r_{\text{ifo}}$. Figure 3.7 compares the displacement spectral density of the two quantum noises in the simple interferometer output to the signal-recycled interferometer with an input power of 3 W. In the spectrum the radiation pressure noise is above the shot noise and the thermal noise at 1 K for a signal recycling mirror with a reflectivity of $r_{\text{sr}}^2 = 0.998$. In this calculation the interferometer contrast was assumed to be perfect ($\mathcal{C} = 1$). But this is not the case in a real experiment and also internal losses reduce the effective recycling gain \mathcal{G}_{sr} . Considerations of real interferometer parameters and signal-recycling mirror parameters are discussed in section 6.3.

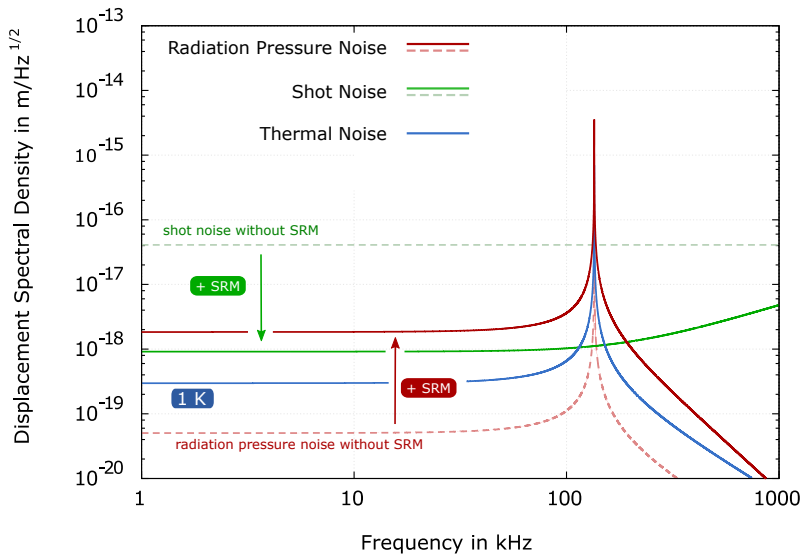


Figure 3.7.: *Displacement Noises of a Signal-Recycled Michelson-Sagnac Interferometer.* Only the membrane's fundamental resonance ($T=1$ K, $f_{\text{m}} = 135$ kHz, $Q=10^7$, $m=90$ ng) is taken into account. The dashed lines present the quantum noise of the interferometer without a signal-recycling mirror (SRM) for an input power of 3 W. The red and green lines show the case for an included SRM with a reflectivity of $r_{\text{sr}}^2 = 0.998$. The shot noise decreases and the radiation pressure noise increases above the shot noise and the thermal noise at 1 K.

3.3. Optomechanical Coupling

Optomechanical coupling is an interaction of a light field with the motion of a cavity mirror (interferometer with SiN-membrane) due to radiation pressure force, which is given by the momentum transfer of the reflected light. A good general overview of cavity optomechanics is given in the review [Asp14]. As already mentioned in section 2.3.2, radiation pressure noise (RPN) is also a result of optomechanical coupling. But in contrast to the RPN the optomechanical coupling described in this section is a dynamical back action, as optical spring and optical cooling, which only are present in a cavity. Since the signal-recycled Michelson-Sagnac interferometer can be seen as a mirror whose reflectivity is tunable via the membrane displacement, such dynamical optomechanical coupling effects occur in the interferometer cavity. The theory of the optomechanical effects in the Michelson-Sagnac interferometer is well described in [Xue11, Tar13, Kha16]. This section only explains the principle of the coupling effects.

3.3.1. Optical Spring

The motion of the movable cavity mirror is driven by the radiation pressure force. This relation between the radiation pressure force and the interferometer cavity detuning results in an optical spring [Bra97, Kha01, Buo02] with the force

$$F_{\text{rp}}(\omega) = -\mathcal{K}(\omega)x(\omega) \quad (3.12)$$

where $\mathcal{K}(\omega)$ is the complex optical spring

$$\mathcal{K}(\omega) = \frac{4\omega_{\text{L}}P_{\text{sr,intra}}}{c\mathcal{L}} \frac{\Delta}{\Delta^2 + (\gamma - i\omega)^2}, \quad (3.13)$$

at dark port, with $P_{\text{sr,intra}}$ as the internal cavity power. The real part $K(\omega) = \Re[\mathcal{K}(\omega)]$ of the optical spring is the rigidity, whereas $\Gamma_{\text{opt}}(\omega) = -1/(2\omega)\Im[\mathcal{K}(\omega)]$ is the optical damping. Due to the optomechanical coupling these two optical spring characteristics modify the membrane's rigidity and damping [Asp14]. The optical rigidity will spring softened or spring hardened the membrane depending on the cavity detuning, which results in a resonant frequency shift of the membrane. The effective membrane frequency is

$$\omega_{\text{eff}} = \omega_{\text{m}} + \delta\omega_{\text{opt}}, \quad (3.14)$$

with $\delta\omega_{\text{opt}} = K(\omega)/m_{\text{eff}}$. The optical damping changes the mechanical oscillator damping to an effective damping

$$\Gamma_{\text{eff}} = \Gamma_{\text{m}} + \Gamma_{\text{opt}}. \quad (3.15)$$

Since the optical damping can be positive or negative depending on the detuning Δ , the effective damping of the membrane can be increased or decreased. For a high mechanical Q-factor $Q_{\text{m}} \ll f_{\text{m}}$ the frequency dependency

3. Signal-Recycled Michelson-Sagnac Interferometer

of the optical spring $\mathcal{K}(\omega)$ can be neglected and it can be estimated that $\omega = \omega_m$. So that the optical rigidity $K(\Delta, \omega_m)$ and damping $\Gamma_{\text{opt}}(\Delta, \omega_m)$ only depend on the cavity detuning Δ . According to [Tar13, sup] the resulting effective mechanical Q-factor can be calculated as

$$Q_{\text{eff}}(\Delta) = \frac{1}{2} \frac{\omega_m}{\gamma_m + \Gamma_{\text{opt}}(\Delta, \omega_m)/m_{\text{eff}}}. \quad (3.16)$$

For $\Gamma_{\text{opt}} > 0$ the effective $Q_{\text{eff}}(\Delta)$ of the membrane decreases, which leads to a decreasing effective temperature

$$T_{\text{eff}}(\Delta) = T_{293\text{K}} \frac{\Gamma_m}{\Gamma_{\text{eff}}(\Delta)} = T_{293\text{K}} \frac{Q_{\text{initial}}}{Q_{\text{eff}}(\Delta)}. \quad (3.17)$$

Therefore additional positive or negative damping Γ_{opt} for the membrane leads to optical cooling ($\Gamma_{\text{opt}} > 0$) or heating ($\Gamma_{\text{opt}} < 0$) of the membrane [Asp14]. Cooling and heating means a reduction or amplification of the thermal fluctuations. The cooling case is the stable region where measurements can be done and the heating case is a parametric instability regime.

On the dark port and cavity resonance ($\Delta = 0$) the rigidity and optical damping vanish. In [Tar13] it is shown that for a membrane which is detuned from the dark port, the resulting optical spring is asymmetric. For far away off dark port membrane detuning there are several stable (cooling) and unstable (heating) regions for different cavity detunings. In contrast to most optomechanical experiments, which are done in a simple Fabry-Perot cavity, for the Michelson-Sagnac interferometer optical cooling is even present on cavity resonance, due to the asymmetric optical damping. The observations of optical cooling in the Michelson-Sagnac interferometer are shown in chapter 4.

3.3.2. Dispersive and Dissipative Coupling

As shown in equation (3.17) the optical cooling depends on the total detuning of the interferometer cavity, because the motion of the membrane is driven by the internal cavity power which depends on the cavity detuning. In general this coupling can be divided into the dispersive and dissipative coupling mechanisms.

Dispersive Coupling

Dispersive coupling describes the coupling of the internal cavity light field and the membrane detuning x that changes the cavity frequency ω_{cav} [Asp14]. The strength of this coupling is given by

$$g_\omega = \frac{\delta\omega_{\text{cav}}}{\delta x}. \quad (3.18)$$

The back-action force spectrum $S_{\text{FF}}(\omega)$ has a Lorentzian shape similar to the power built up inside the cavity [Mar07]. Since this coupling effect is the

dominant one in the Fabry-Perot cavity, the majority of the optomechanical experiments are strongly influenced by the dispersive coupling. As for example the first optical ground-state cooling which is presented in [Cha11]. To reach the ground-state it was required to operate the optomechanical system in the resolved-sideband regime, where the cavity linewidth γ is much smaller than the mechanical frequency $2\pi f_{mo}$ of the mechanical oscillator.

Dissipative Coupling

The term "dissipative" coupling describes the coupling of intra cavity power and membrane position that defines the cavity linewidth γ [Els09]. Therefore the coupling strength can be written as

$$g_\gamma = \frac{\delta\gamma}{\delta x}. \quad (3.19)$$

In contrast to the dispersive coupling the back-action force spectrum $S_{FF}(\omega)$ of the dissipative coupling is a Fano line shape [Els09, Wei13]. The characteristic of this shape is that for a specific detuning ω the back-action force vanishes. Therefore the dissipative coupling allows a ground state cooling without being in the resolved-sideband regime. In [Li09, Wu14] an observation of dissipative coupling with a nanomechanical oscillator is demonstrated. In these experiments the dissipative coupling was dominated by photon dissipation due to internal losses.

Since the membrane displacement has an impact on the cavity frequency and linewidth, both coupling effects occur in the signal-recycled Michelson-Sagnac interferometer. The resulting coupling of membrane motion and light field is an interference of both effects. A detailed theoretical analysis of the generalized optomechanical coupling in this type of interferometer cavity is shown in [Tar13, Kha16]. There it is shown that the impact of each coupling effect is influenced by the beam splitter ratio, the signal-recycling reflectivity and detuning and the membrane detuning. For a membrane detuning of $x=0$ (on the dark port) the dissipative coupling vanishes and the coupling is purely dispersive similar to a simple Fabry-Perot cavity. In [Xue11] it was theoretically shown that for a signal-recycling mirror reflectivity of $r_{sr}^2 = 1$ the dispersive coupling vanishes and the optomechanical coupling in this interferometer is purely dissipative.

3.4. Chapter Conclusion

A signal-recycled Michelson-Sagnac interferometer is in some respect similar to a simple Fabry-Perot cavity. Since the internal power can be increased, also the signal induced by the radiation pressure noise can be enhanced. Therefore with a membrane temperature lowered by a cryocooler and with an increased signal by the SRM, the radiation pressure noise would be observable in the output of the interferometer.

3. Signal-Recycled Michelson-Sagnac Interferometer

The optical spring provides a heating and cooling of the membrane depending on the detuning. In contrast to the simple Fabry-Perot cavity the membrane detuning does not change only the cavity frequency but also the cavity linewidth, which is a specific characteristic of the Michelson-Sagnac interferometer. Due to this dependency not only the dispersive but also the dissipative coupling is observable in this setup. Experimental results are presented in the next chapter.

4

Chapter 4.

Observation of Dissipative Coupling and Cooling

The signal-recycled Michelson-Sagnac interferometer was built up by H. Kaufer and me during his PhD thesis [Kau13, Kau12] and my MSc. thesis [Saw12]. In that time the main motivation for implementing a signal-recycling mirror was the observation of radiation pressure noise. But after implementing the signal-recycling mirror parametric instabilities due a negative optical damping of the optical spring were observed [Kau13, Saw12]. To get a better understanding of this observed optomechanical coupling effect, the signal-recycled Michelson-Sagnac interferometer was theoretically analyzed in a generalized mathematical model by S. Tarabrin in the research group of Prof. Dr. K. Hammerer at the Albert Einstein Institut in Hannover. The results of this theoretically study were published in [Tar13].

This chapter presents the experimental characterization of the generalized optomechanical coupling in the signal-recycled Michelson-Sagnac interferometer and compares the experimental results with the theoretical model calculated by S. Tarabrin [Tar13].

All experimental results of this chapter were previously published in the paper "*Observation of Generalized Optomechanical Coupling and Cooling in a Cavity Resonance*", PHYSICAL REVIEW LETTERS 114, 043601 in 2015.[Saw15]

4.1. Experimental Setup

Since the experimental setup was described in detail in previous works [Kau13, Kau12, Saw12] this section gives only a short overview. The experimental setup could be subdivided in laser beam preparation, interferometer characteristics and detection scheme.

4.1.1. Laser Beam Preparation

The light field at a wavelength of 1064 nm was provided by a **Mephisto** Laser of the company **Innolight**. In front of the interferometer a ring cavity was used as an optical filter to eliminate higher order optical modes and to clean up the polarization. An active laser intensity noise stabilization was also set up, which provided a noise suppression of -10 dB for the relevant measurement frequencies below 150 kHz [Kau13].

4.1.2. Interferometer Characteristics

The experimental setup of the signal-recycled Michelson-Sagnac interferometer is shown in figure 4.1. The optomechanical coupling mirror was a SiN membrane (cf. section 2.1) with a surface of $1.5 \times 1.5 \text{ mm}^2$, which was used as a common end mirror for both arms of the Michelson mode as described in section 2.2. The thickness was about 40 nm which resulted in a power reflectivity of $r_m^2=0.17$ and an effective mass of $m_{\text{eff}}=80 \text{ ng}$. The fundamental frequency of the oscillator was $f_m=136 \text{ kHz}$ at 293 K. The initial mechanical quality factor of this fundamental frequency mode was determined to be $Q_{\text{initial}}=5.8 \cdot 10^6$. To avoid a decrease of the membrane's mechanical quality factor by surrounding gas, the interferometer was setup in a vacuum environment, which provided a high vacuum of $< 1 \cdot 10^{-6} \text{ mbar}$. According to [Wes09] the gas damping can be neglected, for these low pressures. For the measurements presented in this chapter an unbalanced beam splitter with a reflectivity of $r_{bs}^2=0.53$ was used. According to the theory, the unbalanced splitting ratio was expected to increase the dissipative coupling [Tar13]. All optics except the beam splitter were mounted on electrically controllable positioners by the company **NEWPORT**, which provided an alignment inside the vacuum chamber. To keep the cavity length as short as possible optics with a half inch diameter were used for the steering mirrors. The resulting interferometer arm length was 7.5 cm. The implemented signal-recycling mirror with the power reflectivity of $r_{sr}^2=0.9997$ was placed in a distance of 1.2 cm to the beam splitter. Therefore the resulting cavity length was $\mathcal{L}=8.7 \text{ cm}$. According to equation (3.5) this effective cavity length resulted in a free-spectral range of $\delta f_{\text{FSR}}=1.5 \text{ GHz}$.

Interferometer Cavity Detuning

According to the theory [Tar13, Kha16] the weighting of the dispersive and dissipative coupling depends also on the detuning of the membrane and the signal-recycling mirror. Therefore two piezoelectric ceramics were implemented to the mounts of the membrane and the SRM. These two ceramics provided the possibility of continuous sub nm movement in direction of the light field propagation, depending on the voltage applied across the ceramics. With these two ceramics the cavity frequency and linewidth were detuned for the characterization of the generalized optomechanical coupling. Figure 4.2 (a) shows the measurement of the transmitted power of the interfero-

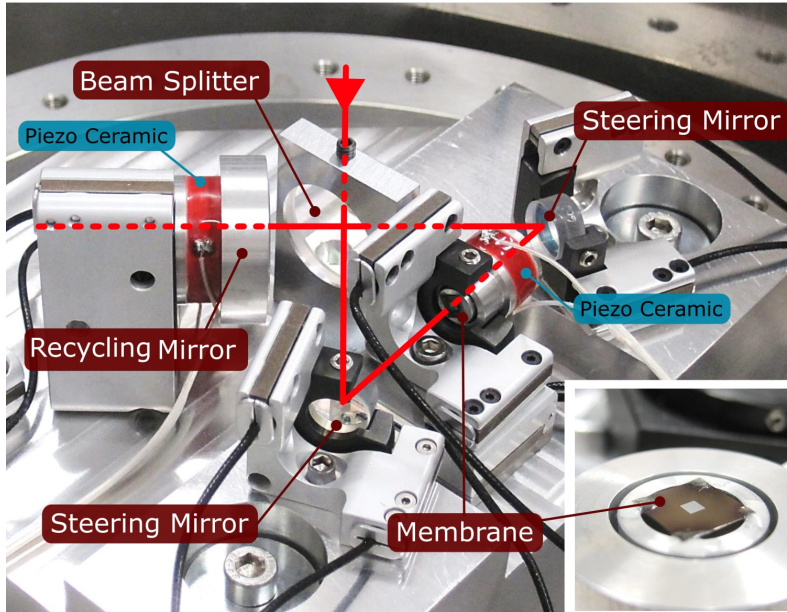


Figure 4.1.: *Signal-Recycled Michelson-Sagnac Interferometer Setup.* The signal-recycling mirror (SRM), the two steering mirrors and the membrane were mounted on remotely controllable positioners from the company NEWPORT, which provides an alignment inside the vacuum chamber. The total cavity length \mathcal{L} from membrane to the SRM was 8.7 cm. The membrane's silicon frame $5 \times 5 \text{ mm}^2$ was glued to an aluminum stamp (insert picture) with a cylindrical piezoelectric ceramic, which allowed the membrane detuning. Also for the SRM a piezoelectric ceramic was used for detuning of the cavity [Saw12, Kau13].[Saw15]

meter cavity depending on the membrane detuning. The asymmetric shape could be explained by the unbalanced beam splitter ratio and was in good agreement with the theory explained in section 3.1.1. This measurements demonstrated that the effective interferometer reflectivity was $r_{\text{ifo}}^2 > r_{\text{sr}}^2$, since it was possible to reach the cavity undercoupled regime for a membrane detuning close to the dark port (cf. figure 3.4). The membrane displacement changes not only the cavity resonance frequency, but in particular it also changes the linewidth of the cavity (cf. section 3.1.1). The observation of this dependency is presented in figure 4.2 (b). The normalized transmitted power is shown in dependent on the signal-recycling mirror detuning for given membrane positions ❶ to ❺ (equivalent to interferometer reflectivities). The higher the interferometer reflectivity, the narrower was the linewidth of the cavity. At the membrane positions ❶ to ❺ the linewidth $\gamma/2\pi$ was tunable from 0.7-1.5 MHz. Thereby the interferometer cavity was far away from the sideband-resolved regime. For the calibration of the x-axis the transfer function of the cavity was measured with a spectrum analyzer for the same membrane detunings. The maximum finesse \mathcal{F} reached was 1200. It was not limited by the reflectivity of the signal-recycling mirror or the reflectivity of

4. Observation of Dissipative Coupling and Cooling

the interferometer, but by the internal losses of the optics. The total internal cavity loss was estimated to be 0.5% [Kau13].

4.1.3. Detection Scheme

In the output port of the cavity a simple photo diode was used for detecting the output light field. This PD transferred the detected photons into an electrical current, where the current was proportional to the detected light power. For measuring the spectra a spectrum analyzer was used, which transformed the output voltage data of the photo diode from the time domain into a frequency domain in dBm units for the power spectrum.

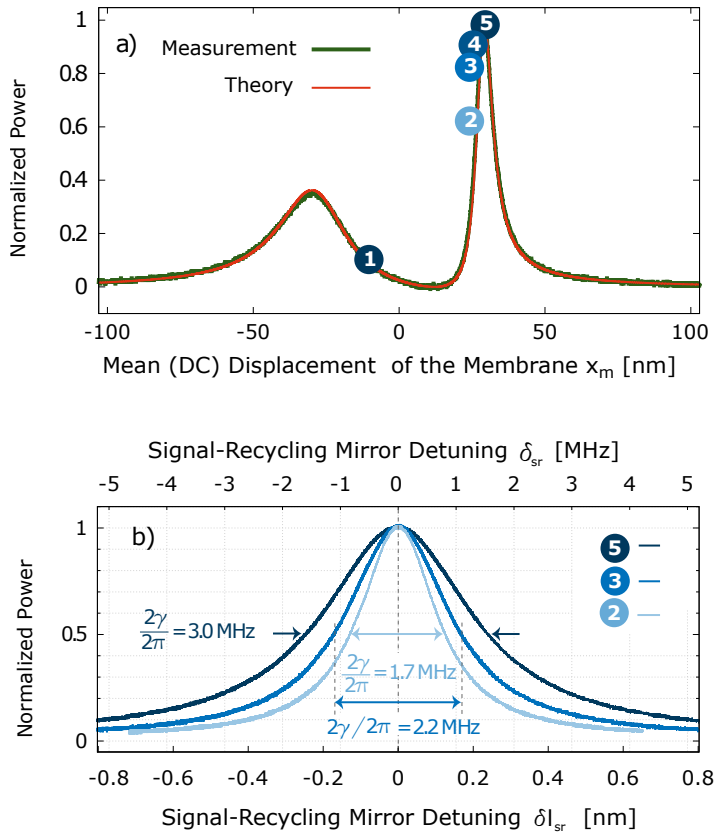


Figure 4.2.: Measured normalized transmitted light powers versus mean membrane displacement (a) and versus signal-recycling mirror displacement for three membrane displacements (b). The input powers used for these measurements were 20 mW (a), and 5 mW (b), respectively. In (a) the SRM was positioned such that at operation point ⑤ an impedance matched resonator was achieved. Numbers ① to ⑤ mark operating points of the membrane that were used for the measurements in this work. Point ① is at 7%, ② at 60%, ③ at 90%, ④ at 95% and ⑤ at 100% of the cavity resonance peak height. (b) shows the dependence of the cavity linewidth γ on the three different chosen membrane positions ②, ③ and ⑤ exemplarily.[Saw15]

4.2. Optomechanical Cooling Measurements

In this section the main measurement results of the generalized optomechanical coupling are presented.

4.2.1. Spectrum Measurement at 126 mK

Figure 4.3 presents the optical cooling by comparing the thermally excited fundamental membrane mode without optical cooling (i.e. without SRM) in figure 4.3-(a) and with optical cooling effect (i.e. with SRM) in figure 4.3-(b). Both measurements were done with an input power of 200 mW. The spectrum taken without SRM was measured with a membrane detuning close to the dark port and at room temperature. This spectrum was calibrated via the derivation of the output power and the known membrane detuning position. A detailed explanation of this method can be found in [Wes09, Wes12]. The Q-factor was determined by a ringdown measurement. Here the membrane was excited by the piezoactuator at its resonance frequency and then after switching off the excitation the ring down of the amplitude was monitored in the time domain by an oscilloscope. The time dependent decreasing oscillation can be described by the equation

$$A(t) = A \cos(\omega_m t), \quad \text{with} \quad A = e^{-\frac{t\omega_m}{2Q}}. \quad (4.1)$$

Fitting A to the measured decreasing amplitude with Q as fitting parameter the mechanical Q-factor could be determined to be $Q_{\text{initial}} = 5.8 \cdot 10^5$. For the spectrum measurement with the SRM (cf. figure 4.3-(b)) the Q-factor could not be determined with a ring down measurement, since the membrane detuning due to oscillations changed the cavity output conditions. Here an effective Q-factor value could be determined by fitting the thermal noise spectral density (cf. equation (2.15)) to the measured thermally excited membrane resonance with Q as fitting parameter. This method worked quite well for low Q-factors, which was the case as the membrane was optically cooled. For high Q-factors ($> 10^7$) the error bar for the fit increases due to the very narrow linewidth (sub mHz regime) of the peak. The effective Q-factor could be determined to $Q_{\text{eff}}=250$. This is the resulting Q-factor of the membrane, which was influenced by the radiation pressure force due to dispersive and dissipative coupling. As described in section 3.3 this adds an additional optically induced damping, which decreased the Q-factor. The optically reduced Q-factor is equivalent to a reduced effective temperature which could be calculated with equation (3.17) to $T_{\text{eff}}=126$ mK. In principle the cooling could be increased by using higher input power, but experimentally it was not possible to measure at higher powers, because the detuning was close to the parametric instability regime. At higher powers the setup "jumped" into the instability regime due to small detuning fluctuations and made a spectrum measurement, which takes a few seconds, impossible.

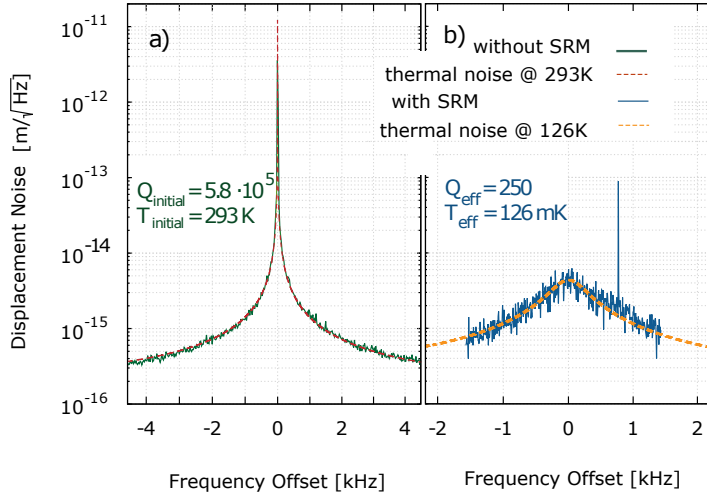


Figure 4.3.: Interferometer output spectra (a) without SRM (i.e. without cavity) close to dark fringe, and (b) for a cavity-enhanced interferometer. The latter spectrum was taken at operation point 1 (Fig. 4.2 a), with a detuning for which our theory predicts a particularly strong cooling effect. The input power was 200 mW in (a) and (b). The thermal noise levels (dashed lines) represent fits to the measurements with the mechanical Q_{eff} -factor as the fitting parameter. In this measurement it could be reached an effective mechanical quality factor $Q_{\text{eff}} = 250$ and an effective temperature of $T_{\text{eff}} = 126 \text{ mK}$. [Saw15]

4.2.2. Observation of Dissipative Coupling

To observe the generalized optomechanical coupling and quantify the optical cooling (i.e. Q_{eff}) in the signal-recycled Michelson-Sagnac interferometer the measurement shown in figure 4.3-(b) was repeated for various membrane and signal-recycling detunings. The quantified damping of the Q-factor Q_{eff} (i.e. optical cooling) is presented in figure 4.4. To avoid influences on the Q-factor due to optical absorption of the membrane all measurements were done next to the standing wave node and not in a vicinity of a standing wave antinode [Fri11]. Also the input power was reduced from 200 mW to 20 mW. The impact of the absorption could be monitored by the frequency shift of the membrane. Since the frequency shift due to absorption was much less than 500 Hz, the influence on the Q factor due to absorption was estimated to be in the order of a few percent and thus negligible for the measurements presented in figure 4.4. This figure represents the observation of generalized optomechanical coupling, i.e. strong signatures of interfering dispersive and dissipative couplings. All four graphs were related to the four various membrane positions ②, ③, ④ and ⑤ shown in figure 4.2. For each fixed membrane position the signal recycling mirror was detuned stepwise over the cavity resonance. At each signal-recycling mirror detuning 5 spectrum measurements were done. The Q-factor for each spectrum was determined similar to the method described for figure 4.3-(b). Every measurement point in figure 4.4 represents 5 independent Q-factor measurements where the error bars

4. Observation of Dissipative Coupling and Cooling

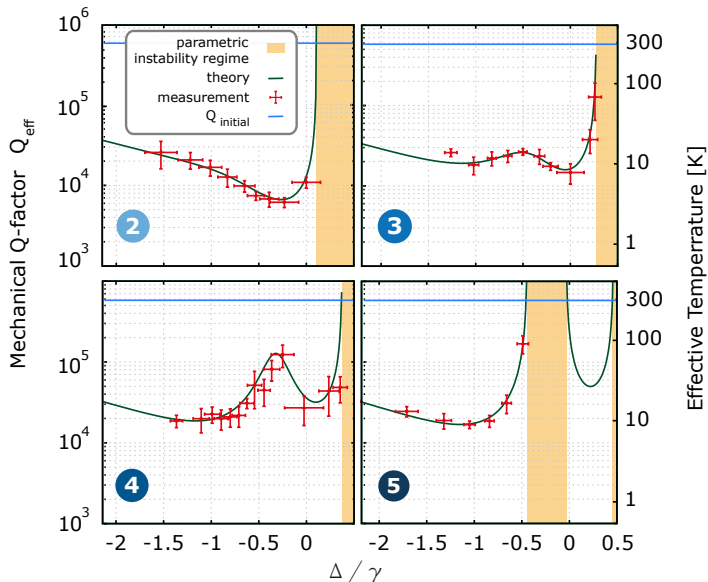


Figure 4.4.: Observed evidence of generalized optomechanical coupling and cooling on cavity resonance ($\Delta/\gamma=0$). Shown in the effective mechanical Q -factor versus cavity detuning for four membrane positions as given in Fig. 4.2(a) with an input power of 20 mW. Already in the first graph cooling on cavity resonance is clearly visible. The next panels show an increasing influence of dissipative coupling and cooling regions that significantly expand into the region of positive (blue) detunings. The last panel confirms the theoretically predicted existence of a new instability region, which appears at negative (red) detunings. Solid lines refer to our theory of generalized optomechanical coupling. Regions of instability are marked yellow. The error bars represent the standard deviation of 5 independent measurements.[Saw15]

represent the standard deviation. The green solid line represents the theoretically calculated effective Q -factor (cf. equation 3.16) for the different membrane detunings. The first graph corresponds to membrane position ②. For negative total detuning Δ of the interferometer cavity optical cooling ($Q_{\text{eff}} < Q_{\text{initial}}$) was observed similar to the purely dispersive regime. But in contrast to that regime optical cooling was observed even at cavity resonance ($\Delta = 0$), which is not possible for the purely dispersive case. At large positive detunings the optical damping got negative which results in the optical heating ($Q_{\text{eff}} > Q_{\text{initial}}$) of the membrane. This was the parametric instability regime, which is marked yellow in the figure. Due to this instability a Q -factor measurement was impossible here. For the membrane detuning position ③ (second graph) the optical cooling on resonance was even more pronounced. In graph two it is visible that a small peak in the cooling regime appears. The graph at membrane position ④ shows the further evolution of the cooling effect. Optical cooling for positive detunings could be observed up to a detuning of $\Delta/\gamma = 0.3$. The appeared peak in graph 2 even increased for further membrane detuning from ③ to ④. In the last graph the peak on

the negative detuning side was evolved into an additional instability regime on the negative cavity detuning side. The theoretical plot in graph 4 predicted an additional cooling region at positive detuning. This region could not be explored in the experiment, because by passing through a region of instability the membrane is excited to very large amplitudes which covers the full range of membrane detuning shown in figure 4.2-(a).

This observed generalized optomechanical coupling was caused by the complex structure of the radiation pressure noise density, which is an interference of a Lorentz profile and a Fano profile corresponding to the dispersive and dissipative contributions, respectively [Els09, Xue11, Tar13, sup, Kha16].

4.2.3. Cooling on Cavity Resonance

A good evidence of having a mixture of dispersive and dissipative coupling is the optical cooling on resonance. According to [Tar13] the cooling on resonance vanishes for purely dispersive and purely dissipative coupling. In figure 4.4 it was already shown that in the signal-recycled Michelson-Sagnac interferometer optical cooling on resonance was present. Figure 4.5 presents the observation of cooling on cavity resonance for different input powers at membrane detuning position \ominus (cf. figure 4.2-(a)), with good agreement with the theoretical model [Tar13, sup].

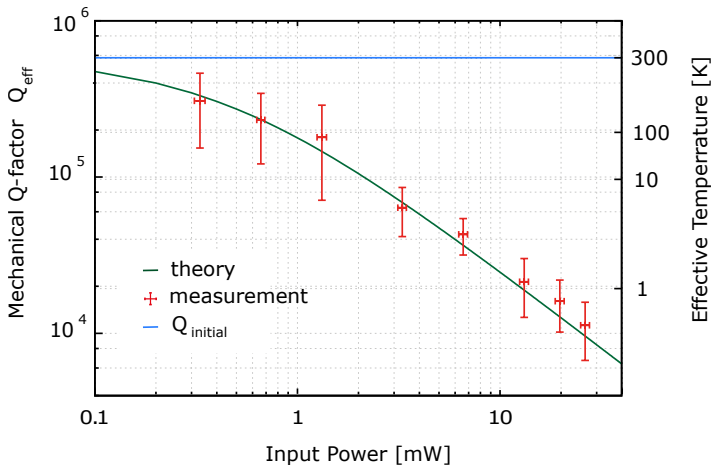


Figure 4.5.: *Cooling on cavity resonance versus input power.* The measurements are in excellent agreement with the theoretical model presented in [Tar13, sup]. Here, the membrane was at position \ominus , as described in Fig. 4.2.

4.3. Chapter Conclusion

With the signal-recycled Michelson-Sagnac interferometer a cavity optomechanical setup with strong dissipative coupling between the motion of the

4. Observation of Dissipative Coupling and Cooling

membrane and the cavity light field was realized. In contrast to other experiments which detected dissipative coupling [Li09, Wu14], the dissipation was not due to optical losses into inaccessible channels. A generalized optomechanical coupling was observed in the experiment and even cooling on cavity resonance could be observed for the first time. Overall the theory of the generalized optomechanical coupling could be confirmed. This is also of interest for gravitational-wave detectors, since the dissipative coupling could give a rise to a stable optical spring [Tar13], as proposed in [Vos14] for the improvement of gravitational-wave detectors. Although the frequency shift due to the optical spring effect was in principle also present in this experimental setup, it was not possible to measure, because due to [Tar13] the expected frequency shift was a few Hz, which was masked by frequency fluctuation of the fundamental mode due to absorptive heating.

5

Chapter 5.

The Cryocooler System

Low temperatures are essential for the observation of RPN in a Michelson-Sagnac interferometer with a SiN-membrane. As shown in chapter 3.2, the membrane has to be at cryogenic temperatures, so that the output measurements are not dominated by thermal noise (cf. figure 2.3). A successfully operating interferometer at cryogenic temperatures at 10 K required very detailed modifications of the cryostat (cf. chapter 5.3) and sophisticated for commercial concepts of the interferometer design (cf. chapter 7).

This chapter starts with a few relevant basics at low temperatures and then continues with describing the 10 K cryogenic system that was used in this experiment. During the developments of the interferometer (cf. chapter 7) it turned out, that this cryogenic system had to be modified in terms of cooling space and electrical wiring for the interferometer. The results of these modifications are presented at the end of this chapter.

5.1. A few Significant Basics at Low Temperature

To get the membrane from 293 K to 10 K many details for the development of the interferometer and the cryostat modifications had to be considered because *"the details are everything"* [Eki06] for a successful cryogenic experiment. The main issue was that at low temperatures the thermal conductivity, heat capacity, dimensional stability and more, behave quite differently from the well known behavior at room temperature. Therefore in particular a good knowledge of heat transfer and the properties of different materials at this temperature range were very useful for the conceptual design of the cryostat modification and the new interferometers.

5.1.1. Heat Transfer

The second law of thermodynamics demonstrates that without any external work the heat Q always flows from the hotter to the colder area [yL41]. The transferred heat is described by the change of heat over time: $\dot{Q}(t) =$

5. The Cryocooler System

$dQ(t)/dt$ In the application of cryogenic systems the topic of heat transfer is essential for two contrary reasons. The first is the thermal insulation of the sample inside the cryostat from the environment at room temperature, and the second is the necessity of a good thermalisation of the sample to the sample holder, which is cooled by the cryocooler.

In general there are three important aspects of heat transfer in cryogenics [Wei98]. Commonly this topic is classified into heat transferred by conduction, radiation and convection [Wei16]. Throughout this thesis, only the first two heat transfer mechanisms were relevant, because the interferometer was inside a vacuum chamber with a pressure of $< 10^{-6}$ mbar, so that the contribution due to convection of the residual gas could be neglected.

Heat Conduction

The conduction heat flow \dot{Q}_{cond} through solids from one surface to an opposite parallel surface of matter, for example a solid bar, is given by

$$\dot{Q}_{cond} = \lambda(T)A \frac{dT}{dx}, \quad (5.1)$$

where A is the cross sectional area, dT the temperature difference and dx the distance between the two surfaces. The temperature dependent $\lambda(T)$ [W/mK] is the thermal conductivity of the material [Eki06]. The thermal conductivity is a specific property of material and highly temperature dependent, which had to be considered while developing the interferometer and cryostat (cf. chapter 5.1.2). The selection of the optimal material for either isolation or high thermal contact, depended highly on the thermal conductivity of the material. In the next section 5.1.2 the figure 5.1 shows the temperature dependance of the thermal conductivity of materials, which were relevant for this thesis. In the appendix B.1 the values are also tabulated for these materials at certain temperatures.

While there are many databases for the thermal conductivity of bulk materials, there is much less information on the heat conduction through solid to solid interfaces. Surfaces are never perfectly smooth, thus the contact between two surfaces is only given at a few discrete points and not at the entire surface. This results in a thermal contact resistance, which could dramatically reduce the total thermal conductivity of the experimental part to the sample holder by few orders of magnitude. For example an interface between two pure copper plates, which are pressed together by a screw with 670 N, has a resultant thermal conductivity of 10 W/K at 4.7 K [Wei98], while each bulk in itself has a much higher thermal conductivity of 630 W/mK (cf. Appendix table B.1) at this temperature.

To increase the interface thermal conductance one could follow different solutions suggested in [Wei98], as for example increasing the applied force. Experiments in the past have shown that the thermal conductance increases asymptotically with raising force [Kit92]. A conforming coating between the

surfaces could also help to increase the contact area. The above example of 10 W/K at 4.7 K for a force of 670 N is the case where the copper plates were uncoated. If the copper plates are gold coated and pressed together with the same force of 670 N the thermal conductance of the interface would increase to 20 W/K. A thin sheet of indium foil would raise the conductivity to even 100 W/K. But the best result would be obtained with a thin film of the vacuum Apiezon-N grease. This would enhance the thermal conductivity to even 200 W/K [Wei98]. On one hand these results demonstrate the importance of using only very few different solids inside a cryogenic experiment to keep the thermal interface resistance low. On the other hand the suggested solutions are very effective and should be considered, while operating the interferometer inside the cryostat.

For the sake of completeness it should be mentioned that the heat conductance through gas also was considered. In [Fre81] it is shown that for a residual gas pressure below 10^{-2} bar the heat transfer is dominated by the radiation heat transfer and therefore could be neglected.

Radiative Heat Transfer

The heat flow from a surface due to radiation is given by the Stefan-Boltzmann equation

$$\dot{Q}_{rad} = \sigma \varepsilon A T^4, \quad (5.2)$$

where σ is the Stefan-Boltzmann constant [$5.67 \cdot 10^{-8}$ W/(m²K⁴)], ε is the emissivity of the surface, A is the area and T the temperature. From this it follows that the radiation heat exchange between two opposite surfaces is given by

$$\dot{Q}_{rad} = \sigma \mathcal{E} A_c (T_w^4 - T_c^4), \quad (5.3)$$

where T_w^4 and T_c^4 the temperatures of the warm and cold surfaces, A_c the area of the colder surface and \mathcal{E} is a factor between 0 and 1, which depends on the emissivity of both surfaces, and the geometries of the surfaces, for example parallel plates, concentric spheres or coaxial cylinders (cf. [Eki06] on page 56). For the experimental settings of this thesis, two cylinders, \mathcal{E} could be calculated by:

$$\mathcal{E} = \frac{\varepsilon_c \varepsilon_w}{\varepsilon_w + \left(\frac{A_c}{A_w}\right)(\varepsilon_c - \varepsilon_c \varepsilon_w)}, \quad (5.4)$$

where A_c and A_w are the areas of the cold and warm surfaces and ε_c and ε_w are the emissivities of them.

The heat transfer formula (5.3) gives a good expression how significant the radiation heat exchange in a cryostat is. The heat flow is proportional to the 4th power of temperature difference from the warm to the cold surface. This

5. The Cryocooler System

is one of the highest heat leaks inside the cryostat. While the interferometer should operate at cryogenic temperature the temperature of the environment (laboratory) is constantly high at 293 K. So this high total temperature difference is founded in the nature of cryogenic experiments and cannot be reduced. But there are still a few techniques, which helps a lot to reduce the high impact of the radiation heat flow inside a cryostat.

A common technique in cryogenics is to use an additional actively cooled heat shield. The cryogenic system used here cooled down the interferometer from 293 K to 10 K. Additionally, there was a metallic heat shield which was cooled down to 77 K and surrounds the interferometer (see figure 5.5 in section 5.2.3). So the temperature difference to the interferometer was reduced from 283 K (without heat shield) to 216 K. This reduced the radiation heat transfer from the vacuum chamber surfaces at 293 K to the interferometer at 10 K by a significant factor of 210. Furthermore, a passively cooled MLI

Material	Temperature		
	293 K	77 K	4 K
Aluminum			
- unfinished	0.09	0.05	-
- oxidized	0.3	-	-
- polished	0.04	0.018	0.011
Copper			
- oxidized	0.6	-	-
- polished	0.03	0.019	0.015
Gold			
- polished	0.02	0.01	-
- polished (plated on Stainless Steel)	0.028	-	-
Bronze			
- polished	0.1	-	-
Stainless Steel			
- unfinished	-	0.049	-
- polished	0.09	0.045	-
Titanium			
- unfinished	0.09	-	-
Multilayer Insulation			
- Aluminum coated	0.022	0.015	-

Table 5.1.: Emissivity ε for different materials, various surface conditions and different temperatures [Eki06, Fre81, Ser17, Mus05, SW14, Fly05].

(Multilayer Insulation) or the so called "*superinsulation*" is used cryogenics

to reduce the radiation heat transfer. A MLI with N layers reduces the radiative heat transfer \dot{Q}_{rad} by a factor of $1/(N+1)$ [Eki06]. In general this is a multilayer of highly reflective and thin material, such as aluminum metalized Mylar foil. To reduce the thermal contact of several metallic layers they were crinkled or separated by spacers or insulators, as for example a net made out of polyester fiber. This technique is efficient, because the thermal conductivity of a MLI with 20-80 layers is in a ultra low range of $4-0.1 \cdot 10^{-4}$ W/mK [Fre81]. It depends on the used material (spacer and metallic layer), the boundary temperatures and the layer density [layers/cm]. A layer density of around 30 layers/cm provides a minimal thermal conductivity [Fly05]. In the cryogenic modification described in chapter 5.3 about 30 layers of crinkled aluminum metalized Mylar were used in addition for the heat shield at 77 K and in a second shielding for the interferometer (cf. chapter 7.3). The thermal conductivity of this MLI is about $6.5 \cdot 10^{-5}$ W/mK (cf. [Fre81] on page 245).

While the temperature difference has such an impact to the radiation heat flow one has to be careful not to underestimate the role of the material dependent emissivity. The emissivities of different metals used in a cryogenic environments scatter in a range 0.01-0.6, depending on the material and the conditions of the surface, e.g. whether it is unfinished, polished or oxidized. As seen in table 5.1 the highly conducting metals gold, copper and aluminum with polished surfaces have an emissivity of about 0.02, whereas the alloys bronze and stainless steel have an about 5 times higher emissivity. Due to the classic model of Drude (1900) the emissivity scales with the square root of the materials resistivity $\varepsilon = 365\sqrt{\rho/\lambda_r}$, where ρ is the electrical resistivity and λ_r the radiation wavelength (cf. [Eki06] page 56). This dependency helps to estimate the emissivity of materials which were used in the experiment, but where no emissivity values could be found in the literature. This was the case for Invar (Fe64Ni36 alloy), which was used as a spacer for the interferometer. Invar has comparable resistivity to stainless steel ([Eki06]), so its emissivity could be expected to be similar to the stainless steel's one. It also explains the identical temperature behavior. For lower temperature the emissivity is decreasing like the electrical resistivity of the materials. The table also shows that the surface finish play a role for the emissivity, by polishing a surface one could reduce the radiative heat transfer by approximately factor of 2.

5.1.2. Properties of Solids

This section gives an overview over the key cryogenic material properties of solids, which were relevant for designing the experiment to operate at low temperatures. These are thermal conductivity, thermal expansion and the specific heat. These properties helps to decide for appropriate materials, to control the heat transfer inside the cryostat, provide dimensional stability in a proper way and get the experiment cooled down to 10 K.

Thermal Conductivity

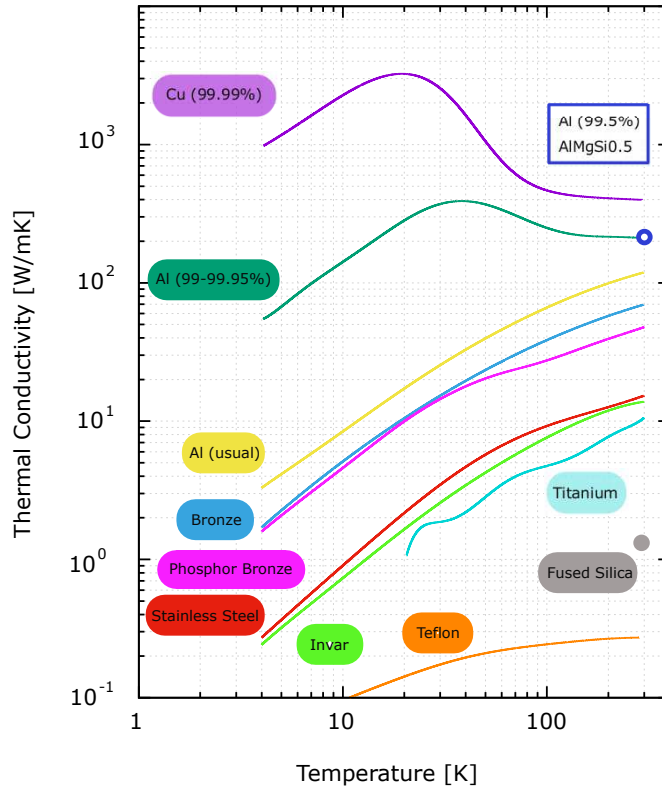


Figure 5.1.: This figure shows the temperature dependent thermal conductivity of several materials over a temperature range of 4-300 K. Presented are only materials, which were relevant for the cryogenic experiments of this thesis. These are pure copper Cu(99.99%) (EN: CW009A) , pure aluminum Al(99-99.95%) (EN: AW1100) and Al99.5 (EN: AW 1050) , usually used aluminum Al (EN: Al5083), aluminum alloy (AlMgSi0.5), copper tin alloy (bronze/CuSn6), phosphor bronze (CuSnP), stainless steel (304), nickel-iron alloy (Invar/Fe64Ni36), titanium (Ti6Al4V) and Teflon (PTFE). For fused silica and the aluminum alloys AlMgSi0.5/Al99.5 only values at 293 K were found [Eki06, Sim92, NIS17, Mar05, Wra59, Cry17a]. But the aluminum alloy is expected to follow almost the line of pure aluminum. The conductivity of the fused silica glass is decreasing with lower temperature [Kit49]. The plots are based on the data listed in the table in appendix B.1

As shown in equation 5.1, the heat transfer is linear dependent on the thermal conductivity of the material. In solid materials the three basic types of thermal conductance are: phonon conduction, electron motion and molecular motion. While the phonon conduction (or lattice vibration) occurs in all solids, the thermal conduction by electron motion is present in metals primarily. In particular in pure metals at low temperatures the almost "free" electrons are responsible for the conductance of heat. This effect leads to

a very high thermal conductivity for pure metals with a high number of "free" electrons, as for example in gold, copper or aluminum. The molecular motion is the major effect in organic solids, as in polymers or glasses. The typical disorder and lattice imperfection in such materials results in a resistance for the heat flow. Generally such materials are used as insulators in cryogenic systems [Fly05]. Figure 5.1 illustrates the temperature dependent thermal conductivity for different materials, which were important for the developing and designing of the cryogenic experiment. The plots are based on specified values, which are listed in a table in the appendix B.1 for specific temperatures from 293 K to 4 K. The oxygen free copper (EN: CW009A), specified with 99.99% purity, and the pure aluminum (EN: AW1050 /AW 1100) provide the highest thermal conductivities at room temperature as well as at 4 K. At cryogenic temperatures the gap between these pure metals and metals with impurities, such as aluminum (EN: Al 5083) and different alloys such as bronze, stainless steel or Invar, even increases from one to two orders of magnitude. The lowest thermal conductivity is provided by Teflon and fused silica. Especially Teflon is often used as a heat transfer resistor.

Thermal Expansion

The interferometers, designed for cryogenic temperatures, and described in chapter 7 had to operate at a high temperature range from 293 K to 10 K. During the cool downs and heat ups the used materials are contracting and expanding. The material dependent thermal expansion coefficient α [1/K] describes the extent of this behavior. Table 5.2 lists a few values at 293 K for relevant materials. The values range widely from $2.5 \cdot 10^{-4}$ 1/K to $4 \cdot 10^{-7}$ 1/K. Using various materials mechanically connected inside the cryostat could cause increasing or decreasing stress during a cool down. If for example two plates of copper are screwed together with stainless steel screws then the force between the two plates will decrease, because the stainless steel screw will shrink less than the copper plates. This will also decrease the thermal conductivity of the interfaces, as described in the heat conduction section. Beside the varying stress also the dimensional stability during the cool down was a big issue for the highly "mirror-displacement" sensitive interferometer. While designing the interferometer and different mountings (described in chapter 7), adapter plates and heat shield (cf. chapter 7) these issues were taken into account. Since the thermal expansion coefficient varies with temperature, the best way to compare the contraction of different materials is to look at the relative contraction $\Delta L/L_{293K}$, with $\Delta L = L_T(T) - L_{293K}$. L_{293K} is the reference value of no contraction and $L_T(T)$ the length of a solid after cooling down to temperature T. Figure 5.2 presents the relative thermal contraction $\Delta L/L_{293K}$ [%] over T for different solids. The plots in this figure are based on values which are listed in table B.2 in the appendix. Whereas the dielectric solids Teflon and silica glass had quite similar low thermal conductivity, the properties due to thermal expansion are quite opposite. The contraction of Teflon during a cool down from 293 K

5. The Cryocooler System

Material	Notation	α [$10^{-6} K^{-1}$]
Teflon	PTFE	250
pure Aluminum	Al	23.1
Bronze	CuSn6	17.0
Phosphor Bronze	CuSnP	17.8
pure Copper	Cu	16.7
Stainless Steel	SS-304	15.1
pure Titanium	Ti	8.0
Invar	Fe36Ni64	2.0
Fused Silica	SO ₂ glass	0.4

Table 5.2.: Thermal expansion coefficient α [$1/K$] for different materials at 293 K. Different alloys of aluminum have almost the same values as pure aluminum [Eki06, Kup17, Mar05, Cry17a].

to 4 K is about 2.3%. In comparison to that the silica glass even expands during a cool down due to its negative thermal expansion coefficient at low temperatures [Eki06].

The nickel-iron alloy is the metal with the lowest expansion of all metals up to now. It was discovered in 1896, and C. E. Guillaume awarded the Nobel prize in 1920 for his work on nickel-iron alloy. Today it is well known as the so called "Invar" for its very low thermal expansion coefficient. The name Invar was derived from "*invariable*" [Net17]. For a cool down to 4 K the contraction is about a factor of 4 lower than the one of titanium and about one order of magnitude lower than the contraction of the other metals. Therefore, Invar is very useful for applications where the device should be cooled down while providing at the same time a high dimensional stability. The advantage over silica glass, which also has a low expansion coefficient, is the higher thermal conductivity.

Specific Heat Capacity

The heat capacity $C=dQ/dT$ [Ws/T] is the amount of heat, which has to be extracted from a body to reduce its temperature by one Kelvin. The specific heat C_m [Ws/(kgT)] is normalized by the mass of the body [Fre81]. For a cryogenic system with given cooling power it takes longer to cool bulk materials with high specific heat capacity than materials with low capacity. In contrary, the temperature of a bulk material with low heat capacity is more sensitive to temperature fluctuations than a material with high capacity. Figure 5.3 shows the temperature dependance of the specific heat for selected materials over a temperature range of 293 K to 4 K. The plots are interpolations based on values from literature and tabulated in B.3 in the appendix. At room temperature aluminum has the highest heat capacity of 902 Ws/(kgT) and copper of 386 Ws/(kgT) the lowest. With decreasing

5.1. A few Significant Basics at Low Temperature

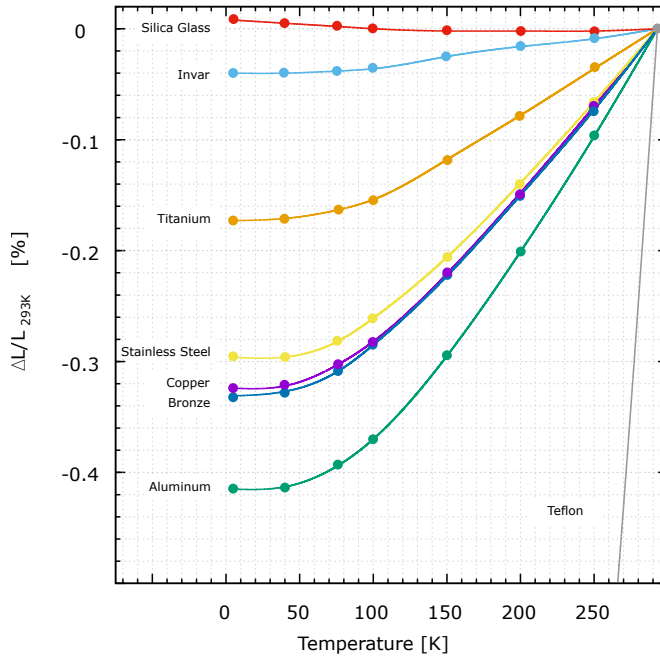


Figure 5.2: The thermal contraction of different materials over temperature range from 293 K-4 K. The y-axis is the relative thermal contraction $\Delta L/L_{293K} = (L_T - L_{293K})/L_{293K}$ in [%]. The Silica Glass is even expanding while cooling down to 4 K because of its small negative thermal expansion coefficient at low temperatures. Invar has the lowest thermal contraction among all metals and alloys. It is about one order of magnitude smaller. On the other side the Teflon has the highest thermal contraction of the here used materials. It is about 2.3% at 4 K [Eki06, Sim92, NIS17, Mar05]. The graphs are based on the listed values in table B.2 in the appendix.

temperature the specific heat capacity also decreases. At low temperature the specific heat capacity is almost equalized between the different materials.

5. The Cryocooler System

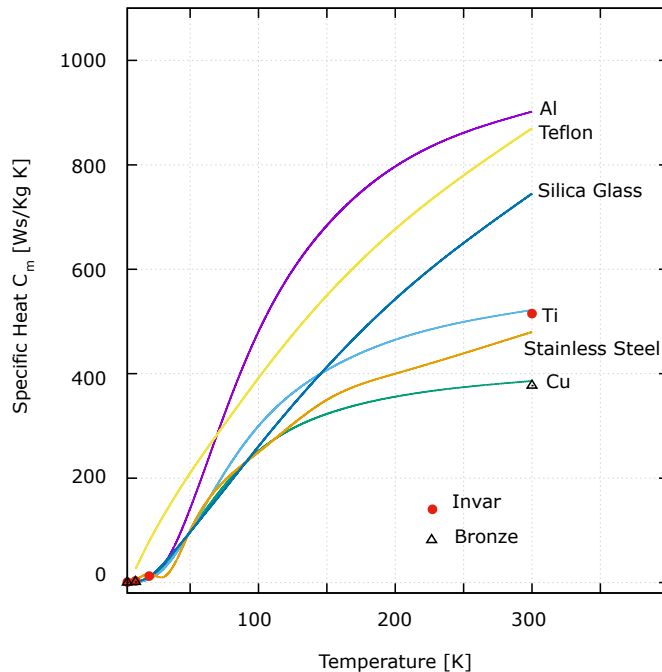


Figure 5.3.: This figure shows the temperature dependence of specific heat (normalized to the mass) for various materials over a temperature range of 293 K to 4 K. At low temperatures there is almost no distinction of specific heat for the various materials. At room temperature the values are spread from 900 - 400 Ws/(kgT) [Eki06, Sim92, NIS17, Kup17]. The graphs are based on the listed values in table B.3 in the appendix.

5.2. 10 Kelvin Cryogenic System

To reduce the thermal excitation of the SiN-membrane, the interferometer had to be cooled down to cryogenic temperatures. Therefore a CCS-XG-CH204N closed cycle refrigerator system from Janis Research Company Inc. was used. The whole cryogenic system was a composition of three different systems. A vacuum system surrounded the experiment, to reduce the gas-damping of the oscillating SiN-membrane. The low temperature of 10 K was provided by a closed cycle refrigerator system and in between these two systems there was a ^4He gas exchange system to decouple the vibration noise of the refrigerator system from the interferometer inside the vacuum system (see figure 5.4).

5.2.1. Vacuum System

The vacuum system was required for three different reasons:

- **Thermal insulation:** The lower the pressure inside the vacuum chamber the lower the heat transfer from the surfaces of the vacuum cham-

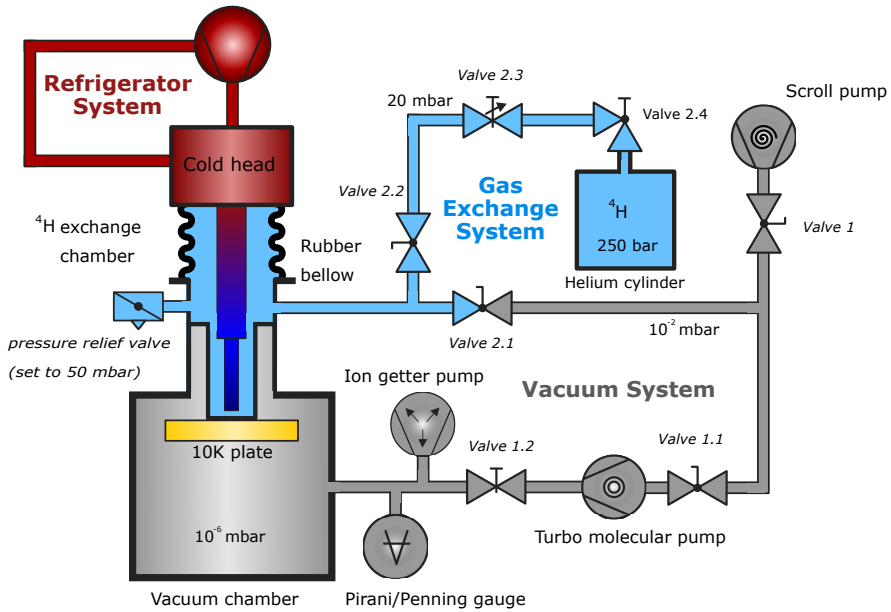


Figure 5.4.: Schematic diagram of the cryogenic system. The cryostat consisted of three different systems. There was a vacuum system (gray), a gas exchange system (blue) and a refrigerator system (red). The vacuum system was important to reduce the gas damping of the membrane. The closed cycle refrigerator system enabled the cooling of the contact plate (yellow) to 10 K. In between these two systems there was the gas exchange system, to decouple the vibrations from the refrigerator system to the interferometer in the vacuum system. Therefore the only mechanical connection between those systems was a flexible rubber bellow. The heat transfer was given by the ^4He gas inside the exchange system.

ber (293 K) to the interferometer (10 K) itself. Reducing the pressure decreases the thermal conductivity of the residual gas inside and also lowers the heat transfer due to gas convection. Thus a pressure below 10^{-4} mbar was recommended in the manufacturers' instructions of the cryogenic system [Man12].

- **Optical losses:** When the interferometer was cooled down, the residual air in the chamber condensed on the cold surfaces. This was especially critical for the optical parts, as there are steering mirrors, beam splitter and membrane. This can lead to optical loss inside the interferometer and reduce its contrast. Also the Q-factor of the membrane will be reduced by condensed water on its surface. Experiences have shown, that these critical influences can be neglected at pressure below 10^{-6} mbar. In general the following procedure was applied to reduce the risk of optical loss: after reaching a pressure below 10^{-4} mbar, the cryostat was switched on. In the beginning of the cool down the temperature of the interferometer was kept at room temperature by heating against the cooling of the cryostat with an internal heater.

5. The Cryocooler System

While the heat shield was cooled by the cryostat, the temperature of the interferometer stayed constantly at room temperature. After about 10-20 minutes the heater could be switched off and the cooling of the interferometer would start. Due to this procedure the residual gas was condensing at the heat shield, which was uncritical, and the optics stayed clean.

- **Gas damping:** As shown in the diploma thesis of T. Westphal [Wes09] a vacuum system was indispensable to reduce the gas damping for a very light SiN-membrane. He also showed that for a pressure $<10^{-6}$ mbar the gas damping could be neglected.

Altogether the vacuum system should provide a pressure below 10^{-6} mbar for this experiment. Thus the vacuum system was conceived with three different pumps (see figure 5.4). The system started with a scroll pump which produced a pre-vacuum of 10^{-2} mbar. After the pre-vacuum was at this stage, a turbo molecular pump pumped down to $<10^{-6}$ mbar. To get rid of the vibrations of the turbo molecular pump an ion getter pump was installed additionally. After the pressure was below 10^{-6} mbar the ion getter pump could be switched on. A few days later, outgassing was reduced to a minimum, so that the valve 1.2 could be closed and the other pumps turned off. The pump rate of the ion getter pump was sufficient to hold the pressure below 10^{-6} mbar.

5.2.2. Heat Exchange Gas System

The gas exchange system enabled a mechanical decoupling of the refrigerator system and the vacuum system, while at the same time a thermal connection was given between these two systems. This was possible by using helium and a rubber bellow. Thus the rubber bellow was the only mechanical connection between the systems, but because of its flexibility it supplied an isolation of the vibrations, coming from the running refrigerator system.

To get the best performance of the gas exchange system, one had to make sure that only helium was inside the exchange chamber during a cool down. The problem was that air inside the exchange chamber would condensate and freeze. That would decrease the thermal conductivity between the two systems. The lowest reachable temperature at the interferometer would be worse by one order of magnitude. Additionally the expanding ice could cause damage. To avoid this, one first had to evacuate the exchange chamber. This was done with the scroll pump of the vacuum system. For this one had to close the direct valve on top of the helium cylinder (see figure 5.4 valve 2.4). After that the valve 2.1 had to be opened and the gas exchange chamber could be evacuated. After reaching a pressure of about 10^{-2} mbar in the exchange gas chamber the residual air was uncritical [Man12] and valve 2.1 could be closed again. With opening valve 2.4 the chamber was filled up with helium. Valve 2.3 was a pressure reducer, which was set to reduce the pressure of the helium cylinder to about 20 mbar above atmosphere. With

a gauge pressure one could exclude that air would leak into the chamber. The exchange chamber had also a pressure relief valve, which was set to 50 mbar above atmosphere pressure. It was required, because of the fast helium expansion during a heat up from 10 K to room temperature. To avoid damage to flexible rubber bellow, the pressure relief valve opens at the set value.

5.2.3. Refrigerator System

The 10 K closed cycle refrigerator system used a determined volume of helium 4 which was recirculated without adding or removing any gas. Based on the Gifford-McMahon thermodynamic cycle a controlled compression and expansion of the helium gas provided the cold temperatures at the sample holder [Fre81, Wei98]. A water cooled compressor Model HC-4E1 of Sumitomo was utilized to maintain the highly compression of the helium. The highly

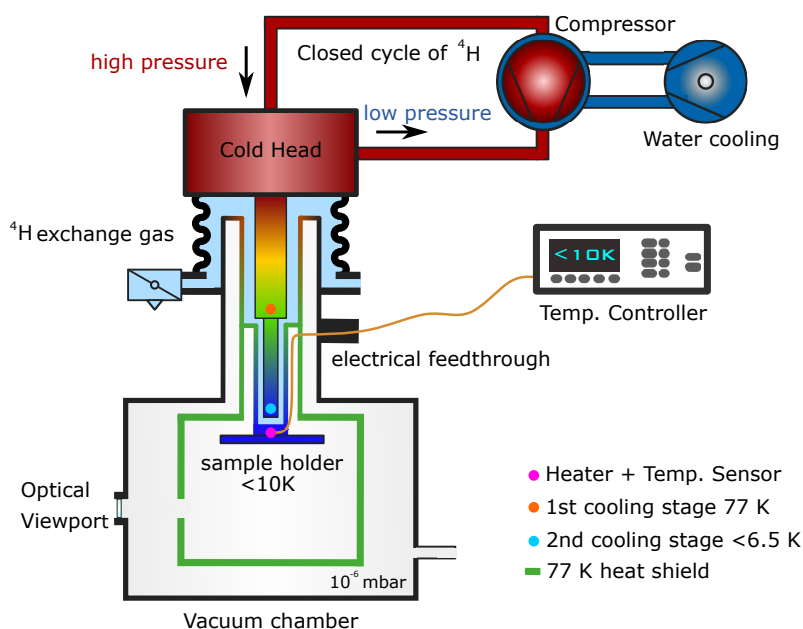


Figure 5.5.: Schematic diagram of the Refrigerator System. The refrigerator system was a two stage closed cycle cryocooler based on the Gifford-McMahon thermodynamic cycle. Inside the closed cycle was helium 4 gas, which was compressed by the compressor and piped to the cold head through flexible metal lines. The cold head had two stages to cool the radiation heat shield to 77 K and the sample holder to < 10 K. The temperature was controlled by a temperature controller using a heater and a temperature sensor at the sample holder.

compressed helium was piped from the compressor to the cold head via flexible metal lines and also the low pressure helium back to the compressor. The cold head had two cold stages. The first stage was to cool the

5. The Cryocooler System

radiation heat shield to 77 K and the second stage for cooling the sample holder to < 10 K [JAN17]. The temperature of the cryogenic system was controlled by the temperature controller Model 335 of the company Lake Shore Cryogenics, Inc. When turning on the compressor the two stages were cooled down to their final temperatures which were not tunable. The temperature on the sample holder was measured by a temperature sensor and regulated by an integrated heater. If the temperature was set to be higher than the temperature of the second stage the heater heated up the sample holder to the required temperature. The temperature sensor and the heater were controlled by the temperature controller, so a stable temperature could be provided at the sample holder.

Refrigerator Cycle:	Modified Gifford-McMahon	
Cold Head Model:	CCS-XG/204N	
Compressor Model:	HC-4E1	
Refrigeration Capacity: (50 Hz, 230 V)	1 st stage:	13.5 W @ 80 K
	2 nd stage:	2.5 W @ 10 K
Lowest Temperature:	2 nd stage:	< 6.5 K
	sample holder:	< 7.8 K
Cool down Time:	2 nd stage:	< 40 min.
	sample holder:	151 min.

Table 5.3.: Specification of the Refrigerator System [JAN17, Man12]. The temperature difference for the lowest reached temperature between the 2nd stage and the sample holder was due to the lower (lower than mechanical copper-copper contact) heat conductance through the helium exchange gas. The same applied for the cool down time. All values are for reference and measured without additional heat load.

The specifications of the used refrigerator system are listed in table 5.3. The refrigerator capacity at the first stage was specified as 13.5 W at 80 K and the second stage provided about 2.5 W at 10 K. These specified powers were not the direct cooling powers for the heat shield and the sample holder. While these powers were available directly at the stages, therefor see figure 5.5, there was a high power reduction because the heat from the experiment had to transfer through helium in the gas exchange chamber. Whereas on one hand the exchange gas was necessary for the vibrational isolation, on the other hand it lowered the cooling rate, compared to a mechanical direct contact between the second stage and the sample holder. So the cooling rate decreased because of the low thermal conductance between solid-gas interfaces and the low thermal conductance of the helium gas (cf. [Eki06]). This effect was visible, when comparing the cooling time of the second stage to 6.5 K. As stated in the specification table 5.3 the cooling time of the second stage to < 6.5 K was less than 40 min. For comparison the sample holder needed 151 min to be cooled down to 7.8 K, without any additional thermal load [Man12]. After consulting Janis Research Company Inc. and their partner company Cryophysics GmbH, it turned out that one could roughly

estimate the cooling power of the refrigerator at the sample holder to be about 500 mW.

5.3. Modification of the Cryogenic System

The very first cryogenic experiment in our group done by R. Moghadas Nia and H. Kaufer [Nia13, Kau13] and the two experiments, presented in chapter 7.1-7.2, started with the custom made cryogenic system build by **Janis Research Company Inc.** and is described in the sections above. With every new developed interferometer the performance of the interferometer inside the cryostat could be improved. But for the latest designed interferometer, described in chapter 7.3, the positioners for the mirrors had to be exchanged, which resulted in a bigger volume of the total interferometer. These changes made a modification of some part of the cryogenic system essential, specifically the vacuum chamber, the 77 K heat shield, the vibration isolation, the wiring and the temperature sensing. All these sections had to be modified and designed to control the heat transfers in a proper way to be able to cool the membrane to at least 10 K. Figure 5.6 presents the modified bottom part of the cryostat, the vacuum chamber, the heat shield and the vibration damping stage.

5.3.1. A new Vacuum Chamber

The old vacuum chamber was a cylindrical chamber with an inner diameter of 14.24 cm and a height (also inside) of 14.12 cm. The inner surface of the chamber was 790.94 cm² (excl. cap) and the volume 2.25 liters. The refrigerator system functioned as the lid of the vacuum chamber. If one wanted to open the vacuum chamber one had to lift the refrigerator system, while the chamber was fixed to the optical table. The vacuum chamber had two optical view ports. The evacuation of the chamber was done through a DN16 flange next to the pressure relief valve. Notice: figures 5.4 and 5.5 already picture the new version. Because of the small valve it took about 5 days to get a vacuum of $5 \cdot 10^{-6}$ mbar.

The new vacuum chamber had also a cylindrical shape and an inner diameter of 31.7 cm and a height of 17.96 cm. The resulting inner surface was 2577.86 cm² (excl. cap) and a volume of 14.17 liters. There were three optical view ports and one flange (KF40) for the evacuation of the chamber. Due to the new flange the pumping time could be reduced to about 2 days. Since the old cap (about 125 cm²) with the refrigerator system on top did not fit any more a new cap (744.5 cm²) was designed, which was screwed to the old top and fitted to the new vacuum chamber.

5. The Cryocooler System

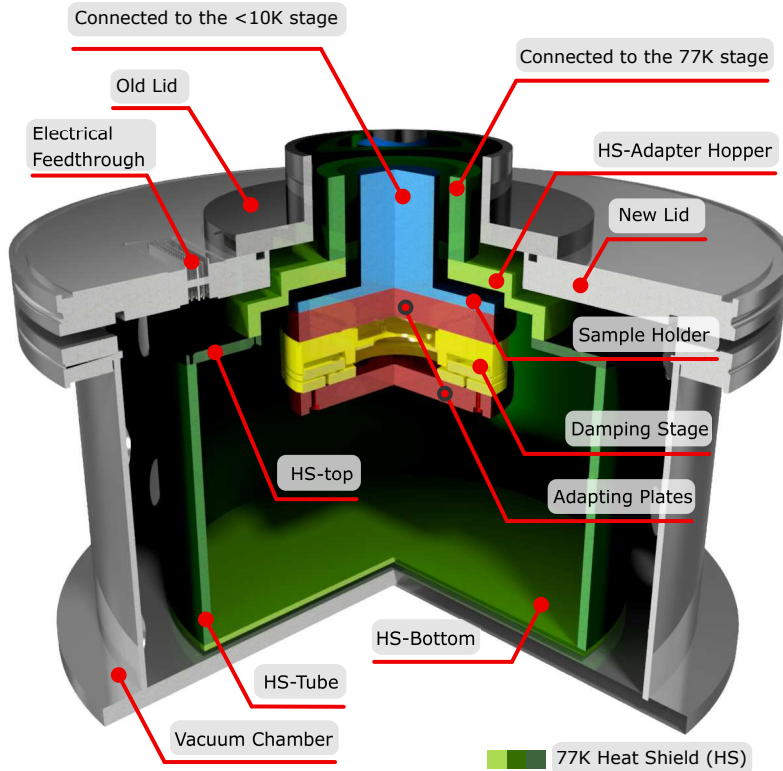


Figure 5.6.: The figure shows the modified bottom part of the cryostat. The gray pieces are parts of the vacuum system. All green objects represent the heat shield at 77 K and the blue one is the sample holder with <10 K. The vibration damping stage is colored yellow. To connect the damping stage to the sample holder and the interferometer to the damping stage, two adapting plates made out of pure copper were necessary.

5.3.2. A new Heat Shield

As the interferometer should again be surrounded by a heat shield it was necessary to build a new one. The main conditions for the material of the heat shield were a low emissivity, to reduce the radiation heat transfer and a high thermal conductance to provide a good thermalisation of the heat shield to the second cooling stage of the refrigerator. A minor condition was a material with low specific heat capacity to get the shield faster to the final temperature of 77 K. Thermal contraction was less significant, because the dimensional stability was unimportant for this part of the modification. Comparing the properties of different materials only pure copper or pure aluminum were qualified for the heat shield. While the emissivity of these two materials is comparable, the specific heat capacity of copper is two times lower and the thermal conductivity two times higher than the one of pure aluminum, at a temperature range from 293 K to 77 K. Although copper was

better than aluminum the heat shield was made out of aluminum because of two reasons. First the cooling power supplied by the refrigerator at the first stage was high enough to handle the heat transfers of an aluminum heat shield and secondly pure aluminum was much cheaper than pure copper.

The new heat shield was a composition of four separate parts, namely bottom, tube, top and adapting plate. The bottom was made out of a 3 mm thick aluminum sheet (EN: AW-1050, 99.5% purity), which was screwed to the tube. The tube had a diameter of 25 cm, a height of 14.45 and a wall thickness of 5 mm. Because it was not possible to get such a tube made out of pure aluminum, it was made out of the high thermal conducting aluminum alloy AlMgSi0.5 (EN AW-6060). The next part was the top of the heat shield. It was a pure aluminum sheet (AW-1050) with 5 mm thickness. In the middle was a hole for the interferometer which was connected to the sample holder. The last part of the heat shield was a kind of hopper to adapt the new heat shield pot to the first cooling stage of the refrigerator. This adapter hopper was also made out of pure aluminum (AW-1050).

The new heat shield pot (without top sheet and the adapter hopper) had an outer surface of about 1688.6 cm² (15.25 cm height and 25 cm diameter). For comparison the old one had a total surface of 478.18 cm² (11.41 cm height and 13.34 cm diameter). Additionally the surface of the top sheet and the adapter hopper had a surface of 636 cm². To reduce the emissivity all parts of the heat shield were mechanically polished. With equation 5.3, the emissivity value for polished aluminum (cf. table 5.1) and the new dimensions the estimated radiative heat load from the vacuum chamber to the heat shield was about 1.03 W. As specified in table 5.3 the first cooling stage of the cryostat provides the heat shield with about 13.5 W which is more than one order of magnitude above the required power.

5.3.3. Vibration Isolation

The biggest issue of the electrical adjustable interferometer made of copper, presented in chapter 7.2, was the vibrational noise, which excited the positioner stacks of the membrane and the steering mirrors. Thus for the last designed interferometer (cf. chapter 7.3) an additional passive vibration damping stage was included. The CVIP (Cryo Vibration Isolation Platform)-3 was a customized product made by the **Janssen Precision Engineering (JPE)** company. Its dimensions were 120 mm diameter and 26.3 mm height. It was made out of bronze, which suited very well as a material for springs even at low temperatures. It was a relatively stiff spring design to be insensitive to added wires (to positioners) and thermal braids, while still having a good vibration isolation. To estimate the noise reduction of this CVIP it could simply be modeled as a spring loaded with a mass of 6.4 kg (interferometer and positioners), a spring constant $k=1.2 \cdot 10^5$ kg/s² and damping ratio $d=0.01$. [JPE15, vB17] It was designed and optimized to have as low as possible cutoff frequencies including the interferometer and positioners as additionally loaded mass (6.4 kg). Modal simulations of the loaded CVIP,

5. The Cryocooler System

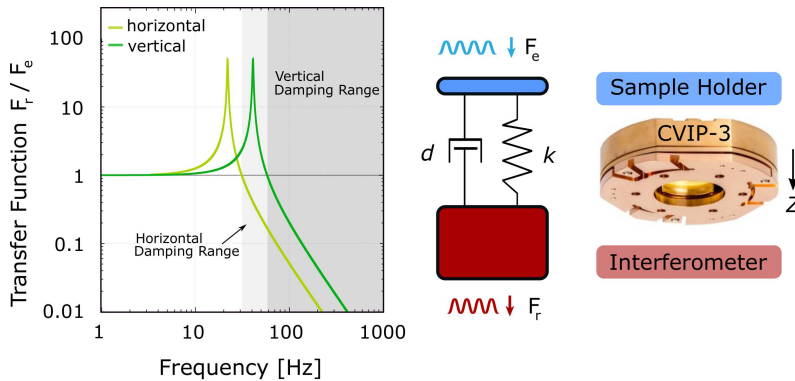


Figure 5.7.: The figure shows the "Cryo Vibration Isolation Platform (CVIP-3)" and its frequency dependent ratio of the external noise force F_e and the resulting noise force F_r at the interferometer. This transfer function was based on modal simulations done by Janssen Precision Engineering company. The damping stage was made out of bronze and was screwed upside down to the sample holder (Cu-adapter plate in between). In the same way the interferometer was fixed to the damping stage. Due to the modal frequency simulations the cutoff frequency in horizontal direction could be expected at 22 Hz and in the vertical direction at 41 Hz [vB17, JPE15]. The spring constant k was specified as $1.2 \cdot 10^5 \text{ kg/s}^2$ and the damping ratio d as 0.01. For frequencies below the cutoff frequencies (22/41 Hz) the interferometer follows the external induced noise force ($F_r/F_e=1$). Around the cutoff frequencies the noise would amplified ($F_r/F_e > 1$) and above the cutoff frequency the noise force frequencies would be suppressed ($F_r/F_e < 1$) by a factor of $1/f^2$.

made by the JPE company, resulted in a cutoff frequency of 22 Hz in the horizontal direction and a cutoff frequency of 41 Hz in the vertical direction (see figure 5.7). The force noise frequencies above this cutoff frequency would be suppressed by -40 dB/decade. So it could be expected, that the limiting noise frequencies at 200 Hz and 300 Hz showing up in the spectrum measurements (see figure 7.6) of the last but one interferometer platform would be reduced by one order of magnitude with this vibration isolation platform. Although the simulations and estimations looked quite promising, a verification in the experiment is still outstanding that vibration noise would not mask the measurement anymore. Due to lack of time this verification could not be done during this thesis.

While this new vibration damping stage may solve the vibration issue, it made it also more difficult to cool down the interferometer and the membrane inside. Having the CVIP between the sample holder and the interferometer and two additional pure copper plates for adapting (cf. figure 5.6), reduces the thermalisation of the interferometer enormously, because of the following aspects:

- **Additional interfaces:** As mentioned in section 5.1.1 mentioned the reduction of the thermal conductivity due to interfaces is significant.
- **Small cross section:** As equation 5.1 shows the heat transfer due to

conduction is linearly dependent the size of area the heat passes. The former interferometer was connected with the entire surface ($1.1 \cdot 10^{-2} \text{ m}^2$) to the sample holder, while the only connection of the isolated interferometer, were the three bronze springs. The cross section of these springs is around $4.9 \cdot 10^{-5} \text{ m}^2$. This was a critical reduction of heat transfer from interferometer to the sample holder.

- **Low thermal conductivity:** The springs and the isolation platform is made out of bronze. Bronze has an about 5.5-300 times lower thermal conductivity than pure copper, depending on the temperature (cf. figure 5.1 and table B.1 in the appendix).

Because of these factors it was hard to estimate how crucial this thermalisation reduction would be in the end. To mitigate this reduction of thermal contact, the CIVP was thermally bypassed by 12 copper braids which were connected to the two pure copper adapter plates (see figure 7.10). These braids were highly flexible, so it could be estimated that they would not decrease the effectiveness of the vibration isolation. This additional cross section for the heat transfer by the braids was about $19.2 \cdot 10^{-5} \text{ m}^2$, which was about 5 times higher than the bronze springs provided. This improvement was supported by the 5.5-300 times higher thermal conductivity of copper. Additionally the interfaces were coated with the grease Apiezon N, which would give an improvement approximately by a factor of 20. This rough estimation showed that the thermalisation reduction by CIVP could almost be compensated by the copper braids and the Apiezon N grease. This is true especially for the low temperature range (down to 10 K), where the improvements were essential because of the decreasing power of the cryostat.

5.3.4. Wiring

A proper wiring in the cryogenic experiment was very essential for reaching the goal temperature of 10 K. Even little carelessness could significantly reduce the cooling power and prevent low temperatures inside the cryostat. As own made experiences have shown, that selecting the right dimension, material and guidance of the wires were essential. There were a few conditions the wires had to fulfill. Firstly they had to be applicable in vacuum and cryogenic temperature environment. Secondly the electrical resistance of each wire should be below $10 \text{ } \Omega$ from controller to actuators, to avoid damage [vB17]. And thirdly the heat load through the wires from room temperature to the sample holder should not exceed the cooling power of approximately 500 mW [Flo17].

The wires should have low electrical resistance ($<10 \text{ } \Omega/\text{m}$) and low thermal conductivity to minimize heat leaking through the wires. Usually used wire materials in cryogenic environments are pure copper, phosphor bronze, nichrome and manganin. While the electrical resistance of the last two materials are specified to be above $10 \text{ } \Omega/\text{m}$, the resistance of pure copper was below $1 \text{ } \Omega/\text{m}$, which would fit the requirement. Phosphor bronze would also

5. The Cryocooler System

work, with a resistance of $4 \Omega/\text{m}$ [Cry17a]. Both materials were used in the work of this thesis. In this subsection the experiences and considerations, during the experiments with wire made out of copper or phosphor bronze, are described.

Copper Wires

The last but one interferometer, presented in chapter 7.2, was operated with 19 cryogenic copper wires (cross section of each was 0.032 mm^2) routed from the electrical feedthrough at the vacuum chamber to the first cooling stage area for thermalisation and then to the sample holder. Due to the new electric positioners from the **Janssen Precision Engineering** company for the interferometer (see chapter 7.3), many more wires were required. In total the new interferometer required 30 wires for positioning the optics and the membrane; 12 wires for two steering mirrors, 6 wires for the membrane positioner stack, 6 wires for positioning the foreseen signal recycling mirror, 2 wires for the diagnostic mirror and 4 wires for the additional temperature sensor (see next section). Therefore an additional electrical feedthrough was implemented at the top plate of the new vacuum chamber. To have enough wires and some spares 26 cryogenic compatible copper wires **311-KAPM-035** by the company **allectra** (cross section of each was 0.081 mm^2) were routed from the new electrical feedthrough to the top of the first stage area, which was cooled to 77 K, and then they were twisted down to the sample holder. These 26 wires were added additionally to the already existing 19 wires. In total there were 45 wires with a total cross section of 2.714 mm^2 . To calculate the heat transfer through the 45 wires from the electrical feedthrough (293 K) to the 77 K stage one has to use the mean thermal conductivity of copper $\bar{\lambda}_{293-77}^{Cu}=417 \text{ W/mK}$ for the temperature range of 293 K to 77 K, because of the temperature dependency of the thermal conductivity and the temperature gradient inside the wires. A table for the different ranges for copper wires could be found in [Eki06] on page 514. With this specified data the heat transfer through the 45 wires from the electrical feedthrough (293 K) to the 77 K stage ($L=20 \text{ cm}$) could be calculated with equation 5.1 as following:

$$\begin{aligned}\dot{Q}_{cond} &= \bar{\lambda}_{293-77}^{Cu} \frac{A}{L} \Delta T \\ &= 417 \frac{\text{W}}{\text{mK}} \cdot \frac{2.714 \cdot 10^{-6} \text{m}^2}{0.2 \text{m}} \cdot 216 \text{K} = 1.22 \text{W}.\end{aligned}\tag{5.5}$$

And for the second wiring section from the 77 K stage to the sample holder the heat transfer was

$$\begin{aligned}\dot{Q}_{cond} &= \bar{\lambda}_{77-10}^{Cu} \frac{A}{L} \Delta T \\ &= 974 \frac{\text{W}}{\text{mK}} \cdot \frac{2.714 \cdot 10^{-6} \text{m}^2}{0.8 \text{m}} \cdot 67 \text{K} = 221 \text{mW},\end{aligned}\tag{5.6}$$

with $\bar{\lambda}_{77-10}^{Cu} = 974 \text{ W/mK}$ and a wire length of 80 cm.

Although the calculated heat load at the sample holder due to the wiring seemed to be low enough compared to the cooling power of 500 mW, the actual cooling measurements displayed the opposite. After the refrigerator ran for three days the sample holder reached 13 K. Usually the sample holder reached about 8.5 K after about 7-8 h. This cooling test run was done without any additional load, such as interferometer or positioners. That means the heat load could only be caused by the radiation heat transfer and the conduction heat transfer through the wires. The radiation heat transfer could be estimated to 6 mW (see chapter 7.3) and therefore this overload of heat must be caused by the additional wires. In a second cooling test run with only 4 wires leading to the sample holder the temperature of 9.5 K could be reached after 8 h. This second measurement confirmed that the heat load of 221 mW overloaded the assumed cooling power of 500 mW at the sample holder. That left the assumption, that the cooling power at the sample holder was less than assumed. This is quite possible as the 500 mW were just an approximate value, which was mentioned during a personal communication [Flo17]. Also a leak in the exchange gas chamber could cause this reduction of effective cooling power. Earlier, a leak was found in the gas exchange chamber and had to be repaired. In the course of the repair water was found inside the gas exchange chamber. This was caused by air, which had leaked through a crack in the rubber bellow and condensated inside. Due to this humidity in the exchange chamber the copper parts at the first and second stage got a patina. It was assumed that this patina increased the interface thermal resistance between the cold head, the helium gas and the sample holder. The patina was removed, but it was decided to exchange also the wires with phosphor bronze wires to reduce the heat load due to wiring.

Phosphor Bronze Wires

The advantage of phosphor bronze over pure copper is the very low thermal conductivity of 48 W/mK at room temperature compare to 397 W/mK (cf. table B.1 in appendix). For low temperatures this difference increases even further (cf. figure 5.1).

In future the experiment will utilize the Duo-TwistTM cryogenic wire (DT32) from Lake Shore Cryotronics Inc.. This wire is specified for applications in high vacuum and with cryogenic temperatures. The diameter of one wire is 0.202 mm (cross section: 0.032 mm^2) and the required length inside the cryostat is about 1 m as before. While the thermal conductivity at room temperature is specified as 48 W/mK, the thermal conductivity at 10 K is 4.6 W/mK (see table B.1 in the appendix). For the mean thermal conductivity $\bar{\lambda}_{293-77}^{PB}$ the value at the higher temperature was assumed $\lambda^{PB}(T) = \lambda^{PB}(293K) = 48 \text{ W/mK}$ (cf. table B.1 in appendix) to have a very conservative estimate of the heat load. With equation 5.1 the heat load

5. The Cryocooler System

from electrical feedthrough to the first stage is estimated as:

$$\begin{aligned}\dot{Q}_{cond} &= \bar{\lambda}_{293-77}^{PB} \frac{A}{L} \Delta T \\ &= 48 \frac{W}{mK} \cdot \frac{1.44 \cdot 10^{-6} m^2}{0.2m} \cdot 216K = 74.65mW.\end{aligned}\tag{5.7}$$

The heat load from the 77 K area to the sample holder with the estimated mean thermal conductivity $\bar{\lambda}_{77-10}^{PB} \approx \lambda^{PB}(T) = \lambda^{PB}(77K) = 25 \text{ W/mK}$ (cf. table B.1 in appendix) could be estimated as:

$$\begin{aligned}\dot{Q}_{cond} &= \bar{\lambda}_{77-10}^{PB} \frac{A}{L} \Delta T \\ &= 25 \frac{W}{mK} \cdot \frac{1.44 \cdot 10^{-6} m^2}{0.8m} \cdot 67K = 3.0mW.\end{aligned}\tag{5.8}$$

This conservative estimated heat load due to 45 wires made out of phosphor bronze is almost two orders of magnitude below the former heat load by the copper wires. With this wire exchange the sample holder should easily reach $<10 \text{ K}$ even though there are 45 wires.

For the sake of completeness it should be mentioned, that joule heating, the heat induced by the electric current passing the wires, could be neglected for the experiments done during this thesis. Although the maximum power was 150 V and the maximum current about 10 A (only pulsed for a few μs) were quite high during alignment, there is no current after the alignment and during the measurements passing the wires.

5.3.5. Additional Temperature Sensor

Due to the "*cryo vibration isolation platform*", the adapter plates and the positioner stack of the membrane, the membrane itself was quite far away from the sample holder and the temperature sensor, which was included by the manufacturer at the sample holder. As the membrane was the main part which should be cooled a second temperature sensor was integrated to monitor the cooling of the membrane directly. Therefore the silicon diode sensor DT-670B-SD from the company **Lake Shore Cryotronics** was built in. It had a temperature range of 550 K to 1.4 K with an accuracy in the 10 K regime of $\pm 12 \text{ mK}$ [Cry17b]. This sensor could also be clamped to other parts to monitor their temperature changes during the cool down.

5.4. Chapter Conclusion

The utilization of the cryocooler made it possible to decrease the thermal noise and though increase the displacement sensitivity of the interferometer. During this thesis the cryostat also had to be modified, because of a new and optimized interferometer design (cf. section 7.3). Therefore a new vacuum chamber and heat shield were designed and built up. Thereby it was

considered to provide a good thermalisation of the heat shield by using pure aluminum. The wiring was also changed, which made the usage of the total remotely controllable interferometer inside the cryostat possible. Due to the change from copper wires to phosphor-bronze wires the heat load could be kept low, although the amount of wires was increased. It also was installed a vibration isolation platform to reduce the incoupling of vibrations which limited previous measurements (cf. section 7.2). New implemented copper braids avoid the decreasing of the interferometer thermalisation due to the vibration isolation platform. Overall the modified cryocooler provides the usage of the new interferometer design and a cooldown of the membrane to 16 K so far, which was a big step towards the observation of radiation pressure noise.

6

Chapter 6.

Towards a Cryogenic Interferometer

Beside the built up of the cryogenic system to cool down the membrane, also the optical parameters were crucial for a successful measurement of radiation pressure noise. As there were the laser system, the detection scheme, optical characteristics of the interferometer, cavity properties and membrane requirements. The cryogenic experiment was subdivided in several runs with different interferometers. The main changes at this various runs were the cryogenic setup, described in chapter 5 and the mechanical changes of the interferometers due to optimization of the mechanical and cryogenic behavior, which is presented in chapter 7. For all these runs the optical requirements and setup was in principle the same. Therefore this chapter discuss the general optical characteristics of the cryogenic experiments.

6.1. Laser Beam Preparation

For the cryogenic experiment the laser system **Koheras Boostik C-15** of the company **NKT Photonics** was used. This system was a CW-single frequency fiber laser at the wavelength of 1550 nm. This wavelength was chosen for the cryogenic experiment, because investigations have shown that the heat entry in the transmitted membrane due to absorption was about 7 times lower than for the wavelength of 1064 nm [Ste17, Ste13]. The Laser system was composed of a seeder and an amplifier, which provided a power of about 5 W. In contrast to the laser system of the first cryogenic interferometer for the experiment [Nia13, Kau13] this laser system had an integrated **Low RIN Option**. Compared to the former used laser system **Koheras Boostik E-15** the amplitude noise was about a factor of 5 lower at membrane fundamental resonance frequency of about 150 kHz (cf. figure 6.3).

The laser beam preparation, mentioned in figure 6.1, was a set of an optical isolator and a ring cavity which was used as a filter to clean up the optical

mode and polarization. With an alignment mirror set in front of the cryostat one could align the beam to get through the interferometer and transmit through the SiN-membrane in the middle.

6.2. Signal Detection Schemes

There were different ways used to detect the light field at the output of the interferometer. At the beginning of the alignment a CCD camera was used to monitor the rough alignment, to avoid clipping and also to monitor the interferometer modes. For measuring the spectrum almost three different options were used, depending on the need. As there were the signal detection by a single photo diode (DC-Readout), the laser noise subtraction technique and the homodyne detection.

6.2.1. DC-Readout

After the rough alignment with the CCD camera, the flip mirror in front of the CCD camera was flipped back and the output light field was detected by a single InGaAs PD, which is called the interferometer readout PD in figure 6.1. This PD transferred the detected photons into an electrical current, where the amplitude of the current was proportional to the detected light power. The photo current was composed by a DC (direct current) part and an AC (alternating current) part. Inside the PD these two different currents were electronically separated, so one could look at the detected DC or AC current. Because of the limited resolution of the CCD camera, the last fine tuning of the interferometer was monitored by the contrast, which could be measured by the PD and monitored by the DC output displayed by an oscilloscope. The AC output was used to measure the spectra with an spectrum analyzer.

For the spectrum measurements the technical laser noise was crucial. In the beginning almost all observed spectra were laser noise limited and sometimes (depending on the input power) even the high thermal excitation peaks of the membrane were not visible. To get rid of the laser noise a second laser noise detection photo diode (LND-PD) was installed in front of the interferometer, to measure the laser noise. This was done with a beam splitter with a reflectivity of $R=36\%$ in the main incoming beam path. The transmitted light was going to the interferometer and the reflected light to the LND-PD. With a $\lambda/2$ plate and a PBS the power to the second PD could be adjusted. With an attenuator the voltage level of the AC channel of the LND PD could be reduced to the same voltage level of the readout PD which detected the signal. The transfer function of both PDs were adjusted to be the same. With a subtraction of these two AC voltages it was possible to subtract the laser noise because of its correlation in both PDs. It looked totally different for the noises which were induced inside the interferometer, for example the thermal excitation of the membrane. This thermal noise was only detected

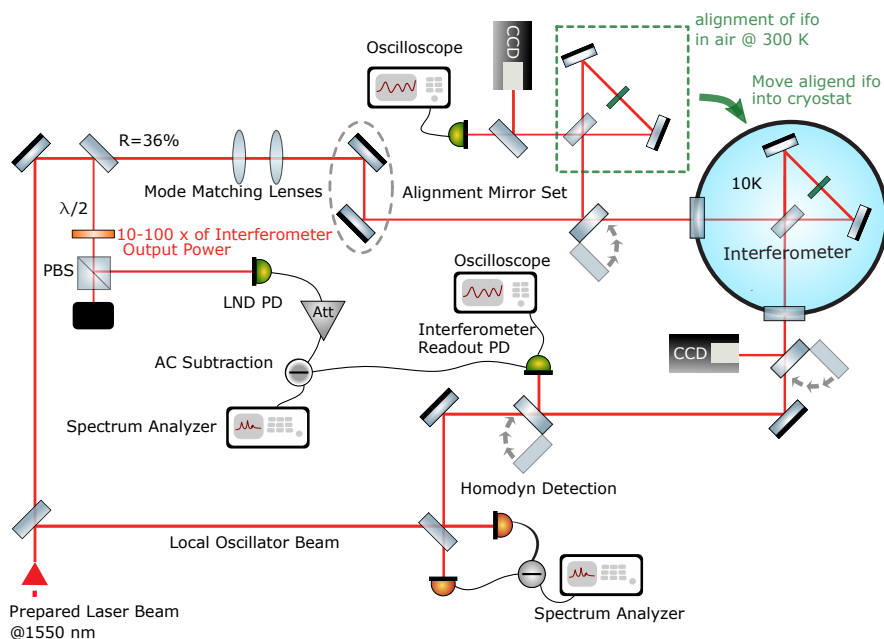


Figure 6.1.: Simplified schematic of the readout for the interferometer in the cryostat. The internally induced signal was detected by a photo diode (interferometer readout PD). A second photo diode (LND (laser noise detection) PD) measured about 10–100 times higher power than the readout PD. After an attenuator the output voltage was equalized to the output voltage of the readout PD and then both outputs were subtracted from each other. Because of the correlation of the laser noise in both photo diodes, it vanished after subtraction. Only the uncorrelated shot noise and the interferometer internal induced signals, were detected afterward by the spectrum analyzer.

by the PD in the readout path, which means it was not subtracted in the subtraction process and so it still was observable with the spectrum analyzer. This technique helped to get shot noise limited spectra of the interferometer output.(cf. figure 6.2)

But this technique also had its limits which should be mentioned. If both PDs for example detect a light field which is shot noise limited, a subtraction of these two noise measurements would result in an increasing noise budget by a factor of 2 compared to the shot noise level detected by one PD as shot noise is an uncorrelated noise. Therefore at the LND-PD the detected power was set to be 10 – 100 times higher as the detected power on the readout PD to make sure the detected light field at the LND-PD was mainly dominated by laser noise. At least the laser noise was several orders of magnitude above the shot noise level. But to get a correct subtraction one had to equalize the voltage levels of both PDs. This was done by an additional electrical attenuator at the LND-PD.

6. Towards a Cryogenic Interferometer

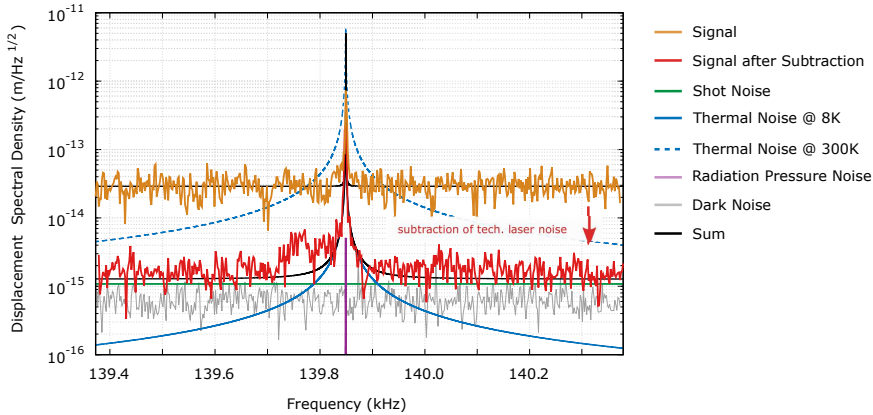


Figure 6.2.: These measurements were done with the electrically tunable interferometer made out of copper. (cf. chapter 7.2) They demonstrate the displacement noise and the effect of the subtraction of technical laser noise by a second photo diode. All measurements are done at 8 K and with 5 mW input power. The orange line display the poor signal in the output of the interferometer. While the red line shows the subtraction of two photo diodes. The technical laser noise was measured by an additional photo diode in front of the interferometer and this noise was subtracted from the signal of the photo diode in the interferometer output. This results in a spectrum measurement where the signal only was limited by the shot noise and the dark noise of the photo diode.

6.2.2. Homodyne Detection

As an alternative to the single photo diode, a balanced homodyne detection scheme [Che07] with two equal PDs and an external shot noise limited local oscillator (LO) field was set up. The homodyne detector offers two advantages:

- **Measurements on dark fringe:** The first advantage was the possibility to measure on the dark fringe. In contrast to a measurement with a single PD, (also called "self homodyne" detection) where the signal comes with carrier light, the signal was gained at the homodyne detector by an external (shot noise) limited LO (local oscillator). This helps to get rid of the technical laser noise as it interferes also destructively with the carrier light field (cf. section chapter:topology). This gets more important for higher input powers as required for the observation of RPN.
- **Using squeezed light fields:** Secondly the interferometer was prepared to operate with a squeezed light field to lower the shot noise level and increase the RPN [Kim01]. Therefore it was necessary to have the possibility to detect different quadratures of the interferometers output signal. For the squeezing measurements it also was necessary to measure at the dark fringe of the interferometer, to reduce loss. As in section 3.1 described the interferometer could be seen as a compound

mirror with a tunable reflectivity. This reflectivity depends on the membrane position, which defines the operating fringe of the interferometer. The dark fringe is the placement where the interferometer has the highest reflectivity (cf. section 2.2). The higher the reflectivity of the interferometer, the lower is the loss of the squeezed light field through the second mirror (interferometer) of the signal recycling cavity. This is why the squeezed light field would be coupled into the interferometer through the output port. So the reflectivity of the second mirror (interferometer) of the signal recycling cavity, would cause the more loss the lower its reflectivity is. As loss is highly impacting the squeezing level, it was important to use a homodyne detector to have the possibility of operating the interferometer at the dark fringe.

6.3. Optical Parameter Discussion for the Interferometer

This section discusses the different optical parameter needs for the congenially cooled interferometer to reach the RPN. In particular the practicability and the implementation to the interferometer were considered. The sensitivity depended mainly on the reachable contrast, the internal optical losses, the signal recycling mirror and the SiN-membrane parameters.

6.3.1. Impact of the Contrast

In previous calculations of the resulting displacement sensitivities in the sections 2.3 and 3.2 it was assumed that the contrast C was perfect ($C=1$). But in reality the contrast was $C<1$ due to not perfectly aligned mode matching, the unbalancing of the beam splitter and the unequal losses in the interferometer arms. An as high as possible contrast was required because of two different reasons.

Influence of Laser Noise

The impact of technical laser noise to the measurement of displacement noise spectra is proportional to the detected power at the output port of the interferometer (see section 2.3.4). As mentioned, there are two laser noise effects which had an impact to the displacement measurement of the interferometer. The first effect is due to the amount of the measured output power, which depends on the contrast and the membrane position. As in figure 6.3 shown the RIN for the used 1550 nm laser at membrane resonance frequency is about $5 \cdot 10^{-7} \text{ Hz}^{1/2}$. With these laser characteristics and equation 2.20 one could calculate the power limit to provide a higher shot noise level as laser

6. Towards a Cryogenic Interferometer

noise to

$$\begin{aligned} 5 \cdot 10^{-10} \frac{\text{W}}{\sqrt{\text{Hz}}} &> P_{\text{out}} \cdot 5 \cdot 10^{-7} \frac{1}{\sqrt{\text{Hz}}} \\ 10^{-6} \text{W} &> P_{\text{out}}. \end{aligned} \quad (6.1)$$

As shown in figure 2.3, high input power was necessary to increase the RPN above the thermal noise although the membrane would be cooled to a few Kelvins. The lower the contrast is the higher is the effective reflectivity of the interferometer. And low transmitted power is equivalent to low detected laser noise at dark fringe (for homodyne detection) or slightly off dark fringe (for single PD detection). That means that for an input power of 1 W an interferometer contrast of $C=99.9999\%$ (at dark fringe) was required, excluding any additional laser noise reductions.

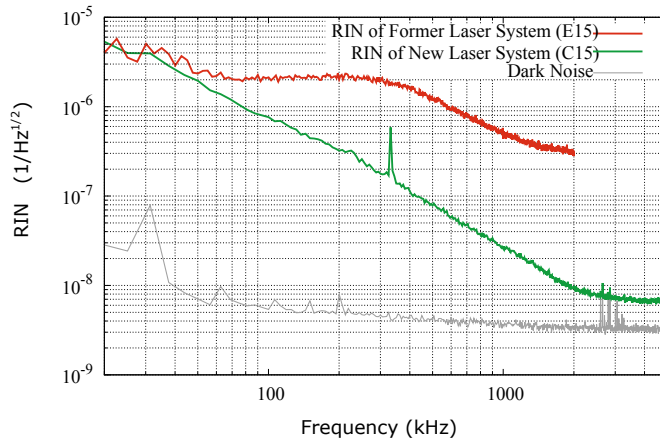


Figure 6.3.: The RIN (Relative Intensity Noise) of the new laser system was about $5 \cdot 10^{-7} \text{ Hz}^{1/2}$ at the membranes fundamental resonance frequency of 150 kHz, which was about 5 times lower than the RIN of the formers one. The peak at about 330 kHz shows the relaxation oscillation of the laser.

The second effect is caused by the unbalancing of the beam splitter. For an unbalancing of the beam splitter the absolute laser noise is different in the interferometer arm and would not cancel out on the membrane. This causes a fluctuation force which drives the membrane similar to the RPN. The impact of this laser noise effect due to unbalancing can be calculated by the equation 2.19 as

$$\begin{aligned} 5 \cdot 10^{-10} \sqrt{\frac{\text{W}}{\text{Hz}}} &> \Delta_{\text{bs}} \sqrt{P} \cdot \text{RIN} \\ 5 \cdot 10^{-10} \sqrt{\frac{\text{W}}{\text{Hz}}} &> 10^{-3} \sqrt{P} \cdot 5 \cdot 10^{-7} \frac{1}{\sqrt{\text{Hz}}} \\ 1 \sqrt{\frac{\text{W}}{\text{Hz}}} &> \sqrt{P} \frac{1}{\sqrt{\text{Hz}}} \end{aligned} \quad (6.2)$$

where the unbalancing measurement results of $\Delta_{\text{bs}} \approx |0.501 - 0.499|$ shown in section 6.3.2 were used. Because of the high balancing the laser noise induced force fluctuations could be neglected for input power below 1 W.

Signal Recycling Cavity

To avoid signal losses the signal recycling cavity had to be undercoupled, which means that the contrast C had to be higher than the power reflectivity of the signal recycling mirror. It was planned to use a signal recycling mirror with $r_{\text{sr}}^2 = 99.93\%$ which was the lower limit for the required contrast.

Reached Contrast in the Cryogenic Experiments

The best reached contrast value was about 99.96% (dark-fringe) for the remotely controllable interferometer with the positioners from **Janssen Precision Engineering** (see section 7.3). As for the signal recycling case a mirror with a reflectivity of $r_{\text{sr}}^2=99.93\%$ was planned, this contrast was high enough to fulfill the condition $r_{\text{sr}}^2 < C$ of an undercoupled signal-recycling cavity (see section 3.1.1) to reduce the signal losses. For the laser noise reduction this reached contrast value seemed to be too low, here one have to consider a few things which let assume that the real contrast might be even higher than the measured value of 99.96%.

The first one is that the precision of the measurement of the contrast was limited by the resolution of the oscilloscope, which results in an error bar of $\approx 0.3\%$. This error bar was high compare to the required last 0.04% to get a perfect contrast. So in principle the contrast might be even higher. The second consideration was that the residual 0.04% interferometer transmitting power was a composition of higher order optical modes which was observed with an CCD camera. This modes were transmitting the interferometer because they could not interfere destructively at the beam splitter. When using a signal recycling mirror these "dirty" modes would be filtered out by the cavity, which would increase the effective contrast significantly. This effects were already observed in the signal recycled interferometer described in chapter 4, where a contrast of $C=99.7$ was reached. After the signal-recycling mirror with a reflectivity of $r_{\text{sr}}^2 = 99.97\%$, it was possible to under couple the signal recycling cavity. This showed that the real contrast was higher than 99.97% although the measured contrast was "just" 99.7%. So overall the reached contrast of 99.96% for the cryogenic experiment seemed to be promising and was in a good range to provide a quantum noise limited measurement at high powers.

6.3.2. Internal losses

The internal interferometer losses had a significant impact to the signal recycling cavity gain G_{sr} and thereby on the reachable sensitivity of the interferometer. According to [Kau13] the loss including signal recycling gain can be calculated as

$$G_{\text{sr}} = \frac{\nu t_{\text{sr}}}{1 - (\nu^2 \sqrt{1 - t_{\text{sr}}^2})}, \quad (6.3)$$

where t_{sr} is the amplitude transmissivity of the signal recycling mirror and ν the amplitude de-amplification inside a cavity. To provide a cavity gain above unity the internal power loss $\eta=(1-\nu^2)$ in the cavity had to fulfill $\eta < t_{sr}^2/4$. On the other hand the optimal gain is given by the condition $t_{sr,opt}^2 = (1 - \nu^4)$. To calculate the reachable sensitivity the internal losses inside the cavity had to be estimated and measured. A general overview of the internal losses of the Michelson-Sagnac interferometer was given in the thesis of H. Kaufer [Kau13]. Thus the loss values of the particular optics could be estimated as 20 ppm for the two steering mirrors, about 5 ppm for a 50 nm thick SiN-membrane at a wavelength of 1550nm [Ste17], 40 ppm due to clipping at the membrane for a 5 times smaller spot diameter than length of the membrane square, and about 200-1000 ppm for the beam splitter. As the highest loss impact was expected to be caused by the beam splitter, in thesis focuses this optical part.

Beam Splitter

In this experiment used a beam splitter made out of high quality fused silica named *Suprasil 3001*[®] was used. While the absorption loss was expected to be about 1-2 ppm [Qua17], the main internal interferometer loss was due to the reflectivity of the AR (anti-reflective) coating on one side. The reflectivity of the AR coating was optimized for an incoming beam under an angle of 45°. The angle was defined by the incoming beam and the perpendicular of the beam splitter surface. The reflectivity of the AR coating was specified $R_{AR} \leq 100$ ppm for the angle of 45°. Since the beam in one interferometer arm was transmitting the AR coating twice, the total loss could be expected to be approximately 200 ppm. According to *Tafelmaier Dünschicht Technik* company, which coated the AR coating, they were not able to specify the AR coating more precisely. So it could even be, that the AR coating was even less the specification. As the AR coating loss was angle dependent, the AR reflectivity has a minimum value for a specific angle.

The other side of the beam splitter was coated with a reflectivity coating specified as $r_{bs}^2 = t_{bs}^2 = 0.5$ at an angle of 45°. The reflectivity and transmissivity of this coating was also highly angle dependent. Generally for angles above 45° the balancing was $r_{bs} > t_{bs}$ and for smaller angles $r_{bs} < t_{bs}$. As described in section 2.3.4 this balancing was crucial for the suppression of the technical laser noise impact inside the interferometer to reduce the laser noise induced force fluctuations to the membrane.

As the loss characterization of the interferometer was crucial for the signal recycling gain and the balancing for the laser noise suppression, a simple test station to characterize the beam splitters angle dependent AR and reflectivity coating more precisely was built up. To measure the very low reflectivity of the AR coating a laser beam with a power of about 1 W was used. This high power beam was transmitting the beam splitter under 45°, while first transmitting the AR coating and afterward the reflectivity coating. To measure the reflected power for different angles, the beam splitter was mounted

6.3. Optical Parameter Discussion for the Interferometer

on a rotation stage. To have a better angle resolution the power was measured in a distance of 75 cm from the beam splitter by a power meter. Figure 6.4 shows the measurement of the angle dependent beam splitting ratio and the AR coating reflectivity. For an angle of 44.5° the best splitting ratio was achieved. The minimum unbalancing was about $0.112 \pm 0.45\%$ (reflected power: $50.06 \pm 0.2\%$, transmitted power: $49.94 \pm 0.2\%$). This was quite good as the perfect unbalancing was in the range of the error bars. But for the same angle the AR coating was about 260 ppm, which was above the specification. Even at the angle of 45° the AR reflection was about 170 ppm. The minimum AR reflectivity of 25 ppm was observed for an angle of 46.9° . But at this angle the unbalancing was at the higher value of $2.7 \pm 0.45\%$. Considering the both characteristics of splitting ratio and AR reflectivity in isolation the measured values looked quite promising, but unfortunately the two minimal values were not at the same angles. In general the unbalancing of the

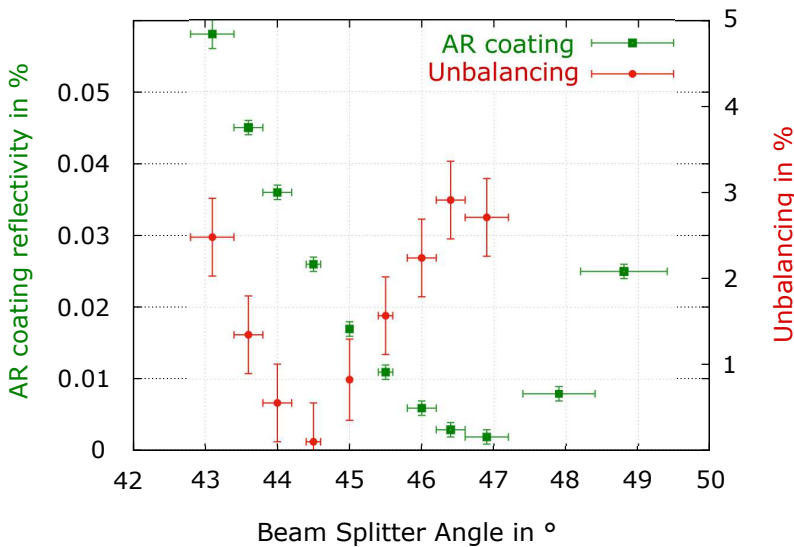


Figure 6.4.: This measurements refer to a "Subrasil 3001" beam splitter [Qua17] and its angle dependent reflectivity. The power reflectivity of the anti-reflective (AR) coating (green) is displayed in % at the left axes. The unbalancing (red) was calculated by $(P_r - P_t)/(P_r + P_t)$, where P_r was the reflected power and P_t the transmitted power at the 50% reflective coated side.

interferometer was more crucial, because it effects not only the maximum reachable contrast but also the impact of the laser noise, described above. In addition the unbalancing was about two orders of magnitude higher than the AR reflectivity, which made it even more important to concentrate on the optimization of balancing than on the lowest AR reflectivity. Therefor the cryogenic cooled interferometers were aligned to the highest reachable balancing (equivalent highest contrast). The estimate unbalancing loss had a wide range because it could not be measured very precisely due to the high

6. Towards a Cryogenic Interferometer

error bars of 4500 ppm (mainly power meter error) compared to the average measured value of 1120. A more precise measurement of the balancing is given by a contrast measurement of an interferometer with an PD at the interferometers output. The highest measured contrast of $\mathcal{C}=99.96\%$ with this beam splitter was done with the remotely controllable interferometer made out of Invar (see section 7.3). Due to this result and to the considerations which are mentioned in section "Reached Contrast in the Cryogenic Experiments" above, it was assumed that the loss induced by an unbalanced interferometer could be expected to be much below 400 ppm. Considering that the beam splitter loss could be estimated to 520 ppm - 920 ppm. The lowest value was given if the real unbalancing loss was just a few ppm (contrast almost 1) and the highest value is estimated by the sum of AR coating loss plus the maximum expected loss from the unbalancing of about 400 ppm.

Total internal loss impact

The total internal loss was ≈ 600 -1000 ppm depending on the real unbalancing value. Using these estimated loss values the effective cavity gain \mathcal{G}_{sr} can be calculated with equation 6.3 as

$$\begin{aligned}\mathcal{G}_{sr,max} &\approx 28 \\ \mathcal{G}_{sr,min} &\approx 20.\end{aligned}\tag{6.4}$$

This is about a factor of 0.5-0.6 smaller compared to the ideal signal recycling cavity gain of 53 without internal loss and perfect contrast, for the given signal recycling mirror reflectivity (see section 3.2).

6.3.3. Interferometer Cavity Design Considerations

Depending on the reachable contrast values mentioned above, and the estimated internal losses the power reflectivity of the signal recycling mirror was set to be $r_{sr}^2 = 99.93\%$. To provide a cavity bandwidth as high as possible the interferometer had to be designed as small as possible. The smallest cavity length which was reached was about 9.9 cm with the possibility to change the cavity length by $\approx \pm 1$ cm. For the cavity design it was necessary to fulfill the cavity stability criterion, which is given by

$$0 < |g_1 g_2 - 1| < 1,\tag{6.5}$$

with $g_i = 1 - L/R_i$ where L is the cavity length and R_i the radius of curvature of both cavity mirrors. Since the membrane is a flat square surface the radius of curvature is $R_{mem} = \infty$ only $0 < L < R_{sr,m}$ had to be considered. So in principle for the signal recycling mirror all radius of curvatures above 9.9 cm were possible. But the additional condition of low waist size at membrane position limits this range. To avoid high losses due to membrane clipping, the spot diameter at the membrane had to be at least 5 times lower than length of the membrane square surface. As above mentioned this would provide an internal clipping loss below 40 ppm [Sie86]. Assuming the membrane was

1.5 mm × 1.5 mm the diameter of the spot should not exceed 300μm. The curvature of the wavefront of an gaussian beam can be calculated as

$$R(x) = x(1 + \frac{\pi\omega^2}{\lambda x})^2 \quad (6.6)$$

where x was the distance from the waist (equivalent to distance from the membrane), ω was the waist radius and λ the wavelength. At a distance of 9.9 cm the spot diameter was 140μm for an assumed radius of curvature $R_{srm} = 10 \text{ cm}$ for the signal recycling mirror, which suited very well to the condition of a small waist diameter.

6.3.4. Membrane Properties Requirements

After contrast, internal losses and signal recycling mirror, the final optical part which parameters had to be characterized was the membrane. In general there were four different parameters which had an impact to the measurement of displacement noise at the interferometer output, as there are the power reflectivity r_m^2 , the mass m_{eff} , the fundamental resonance frequency f_m and the mechanical quality factor Q .

To analyze the effect of the membrane parameters it was started with the present parameters at the measurement shown in figure 7.6 where the used membrane had a square surface of $L_m \times L_m = 1.5 \times 1.5 \text{ mm}$ a thickness of $d=75 \text{ nm}$, a resulting power reflectivity of $r_m^2=17.5 \%$, a fundamental resonance frequency of $f_m \approx 140 \text{ kHz}$ and a mechanical Q -factor of $Q_{293K} = 2 \cdot 10^5$ at room temperature and $Q_{8K} = 5.6 \cdot 10^6$. As in section mentioned it was also assumed a signal recycling mirror reflectivity of $r_m^2=17.5 \%$, an internal cavity loss of 1000 ppm and the resulting signal recycling gain of 20. The resulting noise budgets are shown in figure 6.5 are calculated for an input power of 100 mW and a temperature of 10 K. As start the laser noise was not included in the calculations. Because of the promising measurements results of the balancing and the contrast it was assumed that the interferometer output would be shot noise limited. For this parameters set the resulting spectrum would be limited by the thermal noise which is about one order of magnitude above the radiation pressure noise. So for the final spectrum measurement which should be limited by the radiation pressure noise a membrane with matched parameters had to be used.

The membrane parameters proportionality of the increased radiation pressure noise and decreased shot noise (cf. section 3.2) is

$$\left. \begin{aligned} S_{\text{sn}} &\propto \frac{1}{\sqrt{P_{\text{in}} r_m^2}} \\ S_{\text{rpn}} &\propto \frac{S_{\text{rpn}} \sqrt{P_{\text{in}} r_m^2}}{m f_m^2} \end{aligned} \right\} \Rightarrow \frac{S_{\text{rpn}}}{S_{\text{sn}}} \propto \frac{P_{\text{in}} r_m^2}{m f_m^2} > 1. \quad (6.7)$$

For this proportionality comparison it was assumed that $f \approx f_m$ which led to $\chi_m \propto 1/(m f_m^2)$. The ratio of $S_{\text{rpn}}/S_{\text{sn}}$ increases for increasing power and

6. Towards a Cryogenic Interferometer

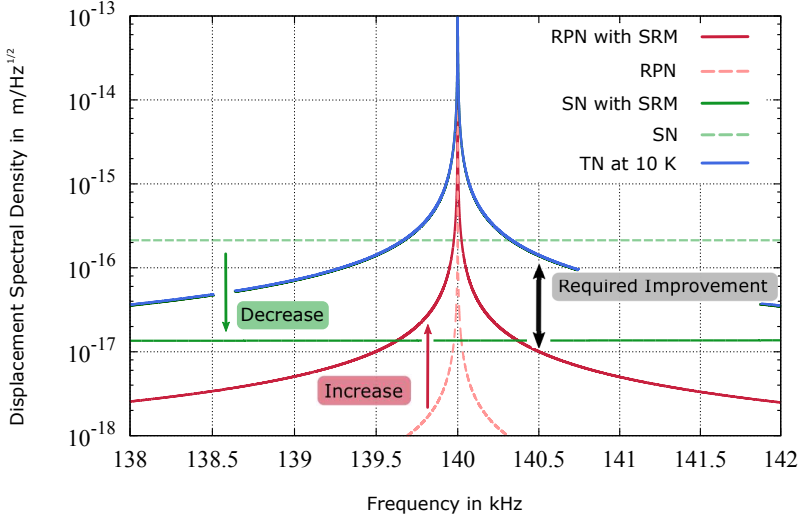


Figure 6.5.: Calculated displacement spectral density with experimental parameters and signal recycling mirror (SRM). The calculated noise budgets are radiation pressure noise (RPN), shot noise (SN) and the thermal noise (TN) at 10 K for the interferometers output without SRM. For comparison also the RPN gained by the signal recycling cavity (RPN with SRM) and the SN are shown, which was decreased by the gain induced by the SRM. The assumed gain factor was 20 and the SRM reflectivity $r_{sr}^2=99.93\%$. For all noise budgets the membrane's resonance frequency was $f_m = 140$ kHz, the quality factor at 10 K $Q_{10K} = 5.6 \cdot 10^6$, the thickness was 75 nm and the resulting reflectivity $r_m^2=17.5\%$. With this parameters the measurement would be dominated by TN which is about one order of magnitude above the RPN with SRM.

membrane reflectivity and lower membrane frequency. The comparison of the thermal noise to the radiation noise results in

$$\left. \begin{aligned} S_{tn} &\propto \frac{1}{mf_m^2} \sqrt{\frac{f_m}{mQ}} \\ S_{rpn} &\propto \frac{S_{rpn} \sqrt{P_{in} r_m^2}}{mf_m^2} \end{aligned} \right\} \Rightarrow \frac{S_{rpn}}{S_{tn}} \propto \sqrt{\frac{P_{in} r_m^2 mQ}{f_m}} > 1 \quad (6.8)$$

As shown in figure 6.5 it is necessary to increase the ratio S_{rpn}/S_{tn} . Due to equation 6.8 this could be done by increasing especially the Q-factor Q and the reflectivity r_m^2 of the membrane. According to S. Gröblacher in Delft [Nor16, Grö16] it is in principle possible to produce membranes with a Q-factor of $>Q=10^7$ at room temperature and an increased reflectivity of $>r_m^2 = 90\%$ due to a photonic crystal pattern on the SiN-membrane. Figure 6.6 shows the optimized displacement sensitivity with the conservative estimated Q-factor $>Q=5 \cdot 10^8$ at 10 K and an increased reflectivity of $>r_m^2 = 90\%$. As in general the Q factor increases by a factor of 10, while cooling down to 1-10 K, here it was assumed that the Q-factor would reach $>Q=5 \cdot 10^8$. With this optimized parameters it would be possible to

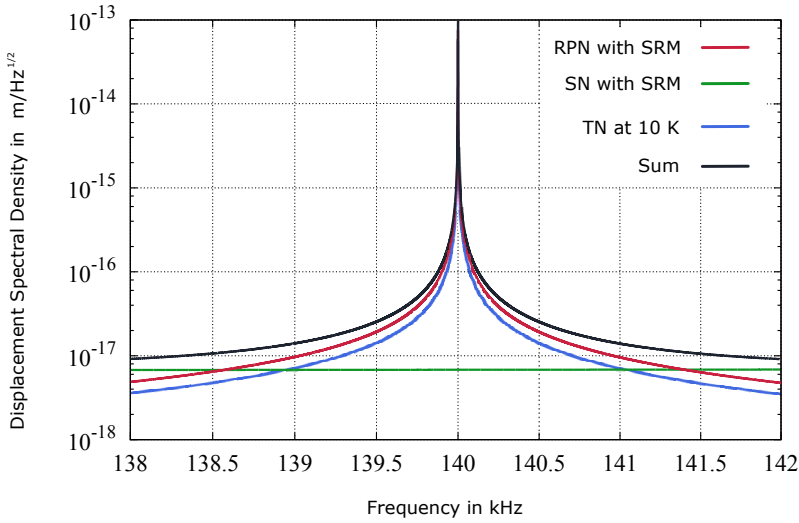


Figure 6.6.: Calculated Displacement Spectral Density with improved membrane parameters and signal recycling mirror (SRM). The calculated noise budgets are gained radiation pressure noise (RPN) and decreased shot noise (SN) by signal-recycling mirror (SRM) and the thermal noise (TN) at 10 K for the interferometers output without the SRM. The black line represents the sum of all noise budgets. The assumed gain factor was 20 and the SRM reflectivity $r_{sr}^2=99.93\%$. For all noise budgets the membrane's resonance frequency is $f_m = 140$ kHz, the quality factor at 10 K is $Q_{10K} = 5 \cdot 10^8$, the thickness was 75 nm and the resulting reflectivity $r_m^2=90\%$. With this parameters the displacement sensitivity of RPN is about 1.25 times above the thermal noise.

be mostly limited by radiation pressure noise next to the resonance frequency of the membrane. For an off resonance frequency of 138 kHz the displacement noise of RPN is $4.5 \cdot 10^{-18} \text{m}/\sqrt{\text{Hz}}$ and the thermal noise displacement $3.6 \cdot 10^{-18} \text{m}/\sqrt{\text{Hz}}$. The overall reachable sensitivity would be about $10^{-17} \text{m}/\sqrt{\text{Hz}}$ at 138 kHz. Thereby the sensitivity would be increase by one order of magnitude compare to the measured results at 10 K so far.

6.4. Chapter Conclusion

In this chapter it is shown, that with the reached interferometer contrast of $\mathcal{C}=0.9996$, the estimated internal losses of $\approx 600\text{-}1000$ ppm and an unbalancing of $\Delta_{bs} \approx 2 \cdot 10^{-3}$ for the beam splitter it is in principle possible to observe the radiation pressure noise. As the unbalancing and contrast measurement had a limited resolution it was assumed that the laser noise will be suppressed enough, so that it will not influence the spectrum measurement. It is also was shown that the membrane had to be changed to a membrane with following required parameters: mechanical Q-factor $Q=1 \cdot 10^7$, reflectivity of $r_m^2 = 0.9$, a thickness of 50 nm, square surface of $1.5 \text{ mm} \times 1.5 \text{ mm}$ and a frequency close to 150 kHz. The future planned signal recycling mirror

6. Towards a Cryogenic Interferometer

should have a reflectivity of $r_{\text{sr}}^2 = 0.9993$, to provide at least a recycling gain \mathcal{G}_{sr} of 20. A measured output spectrum with such an interferometer setup would be limited by the radiation pressure noise which is calculated (see figure 6.6) to be about 1.25 times higher than the thermal noise at 10 K.

7

Chapter 7.

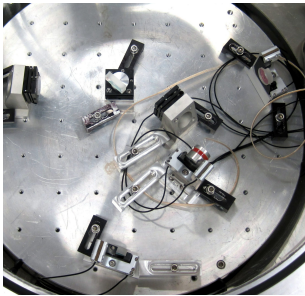
Realized Interferometers at Cryogenic Temperatures

The first Michelson-Sagnac Interferometer with a SiN-membrane was realized in the group of Prof. Dr. R. Schnabel in Hannover in 2008. Over the years different designs were developed. Table 7.1 gives an overview about the operation time, different features, achievements and challenges of all different interferometer types.

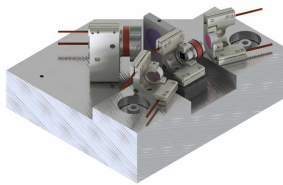
The interferometer shown in chapter 3 was conceived for operating at room temperature. There were two issues which prevented a cool down of that interferometer. The first problem was the size of the interferometer. The cryogenic vacuum chamber was much smaller than the vacuum chamber used before. The second problem were the positioners from NEWPORT, which were not compatible for cryogenic temperatures. Overall it was necessary to have a complete re-design of an interferometer that could operate at low temperatures.

The first interferometer operating at cryogenic temperature, was designed and build by Ramon Moghadas Nia during his Master thesis [Nia13] in collaboration with Henning Kaufer [Kau13]. While spectra could be measured at 8 K, it also showed up a few problems, which limited the measurements. The misalignment of the interferometer due to contraction of material during the cooldown was a severe issue. Although the membrane was electromechanically tunable, the steering mirrors were not. During the cooldown the screws, holders and the copper base plate contracted leading to a decreased contrast, from 97.4% at 293 K to almost 20% at 8 K [Nia13].

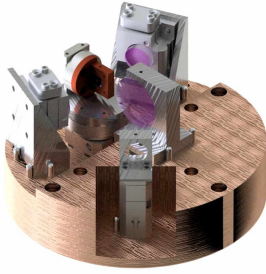
7. Realized Interferometers at Cryogenic Temperatures



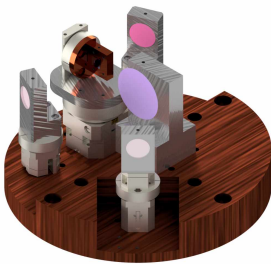
- **2008-2010**
- **Features:**
 - vacuum compatible
 - electronically adjustable in all degrees of freedom
- **Achievement:** Measurement of the readout noise below the SQL (standard quantum limit) of the membrane.
- **Publication:** [Wes12, Wes09]
- **Problems:** Vibration noise couples to the base plate and causes noise peaks in the spectrum.



- **2011-2014**
- **Features:**
 - vacuum compatible
 - electronically tunable
 - vibration isolation
 - signal recycling cavity
- **Achievement:**
 - tomographic readout
 - spectra without vibration noise
 - observation of dissipative cooling
- **Publication:** [Saw12, Kau12, Kau13, Saw15], part of this work, see chapter 3)
- **Problems:** Not compatible for cryogenic temperatures



- **2012-2013**
- **Features:**
 - vacuum compatible
 - cryogenic compatible
 - copper base plate
 - membrane position electronically tunable
- **Achievement:**
 - new membrane holder and positioner stack
 - first spectrum measurements at 8 K
- **Publication:** [Nia13, Kau13]
- **Problems:**
 - Hard to align, because of mechanical holders.
 - Misalignment of not electrically tunable optics during the cool down.



- **2013-2015**
- **Features:**
 - vacuum compatible
 - cryogenic compatible
 - copper base plate
 - electrically tunable
- **Achievement:**
 - design new steering mirror holder (electrically tunable)
 - spectrum measurements at 10 K
- **Publication:** part of this thesis, see chapter 7.2
- **Problems:** Internal vibration modes of the steering mirror holders.

7. Realized Interferometers at Cryogenic Temperatures


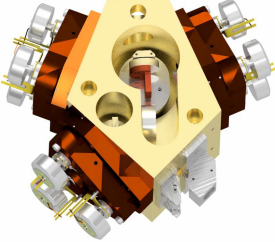
	<ul style="list-style-type: none"> • 2014 • Features: <ul style="list-style-type: none"> – vacuum compatible – cryogenic compatible – Invar base plate – quasi-monolithic • Achievement: <ul style="list-style-type: none"> – mechanical Stability – Dimension Stability during Cooling • Publication: [Ste14], part of this thesis, see chapter 7.1 • Problems: Alignment is not repeatable after several times due to hysteresis deformation of invar. Despite enhancement of the contrast still not high enough.
	<ul style="list-style-type: none"> • 2015-2017 • Features: <ul style="list-style-type: none"> – vacuum compatible – cryogenic compatible – Gold coated Invar spacer – electrically tunable • Achievement: <ul style="list-style-type: none"> – mechanical stable positioners – very high contrast @ 293 K • Publication: part of this thesis, see chapter 7.3 • Problems: electronically issues, "only" 16 K due to additional heat transfer

Table 7.1.: Overview of the evolution of the Michelson-Sagnac interferometer in the group. For comparison the different features and achievements are listed. Also the publication and the problems one had to struggle with.

One goal of this thesis was to solve this problem and develop a new interferometer in which the contrast stays very high even though it would be cooled down to 10 K. Therefore there were two ideas to get rid of decreasing contrast:

- **Quasi-Monolithic Interferometer:** One of the biggest deformation

in the former interferometer was induced by the mechanically adjustable steering mirror holders. So the idea was to leave out as many adjustable holders as possible inside the interferometer, and build it from a solid material with very low thermal expansion. With a very rigid connection between optics and this material the misalignment could be kept to a minimum. Chapter 7.1 explains the idea and the results in detail.

- **Remotely adjustable Interferometer:** This was a quite different concept in the opposite direction. The idea was to develop an interferometer which was totally adjustable from outside the cryostat. So that after a cool down the interferometer could be realigned at 10 K. Detailed descriptions of two new designs and first results are presented in chapters 7.2-7.3

7.1. Quasi-Monolithic Interferometer of Invar

The development and testing of the Quasi-Monolithic interferometer was done in collaboration with Morten Steinecke during his Bachelor thesis [Ste14].

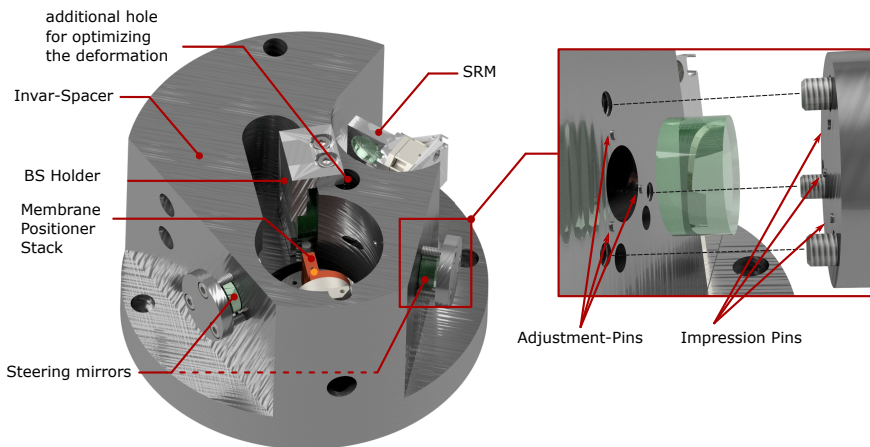


Figure 7.1.: *Quasi-Monolithic Interferometer.* The spacer for the quasi-monolithic Interferometer was made out of Invar. The Membrane was electromechanically adjustable. This also applied to the future planed SRM (signal-recycling mirror). The steering mirrors and the BS (beam splitter) were directly contacted to the Invar-Spacer. To align the Interferometer the Adjustment-Pins had to be sanded. Via the Impression-Pins the mirror was directly pressed against the Spacer by three screws.

7.1.1. Optical Mounting

On the way to a quasi-monolithic interferometer one had to evaluate which optics could be clamped to the spacer at fixed position.

7. Realized Interferometers at Cryogenic Temperatures

The steering mirrors and the BS were good candidates for clamping to the spacer, because there is no necessity to move or adjust them, once they are perfectly aligned. The difficulty here was to bring the steering mirrors and the BS into the perfect alignment for the first time. The mechanical workshop was only able to build a spacer with a precision of 10^{-5} m, which was not precise enough. To reach a contrast of $> 99.93\%$ (cf. section 6.3) the accuracy of the angle and position of the surfaces to which the optics would be clamped had to be in a range of $< 10^{-6}$ m. Since the precision of the workshop was not exact enough, we had to optimize the very fine adjustments by sanding and polishing the spacer contact surfaces for the optics by hand.

Polishing a surface by hand and keeping it smooth and controlling the angle between the surfaces simultaneously is nearly impossible. A suitable solution for this purpose was to press the steering mirrors to only three well defined points on the spacer surfaces, because they are much more controllable by hand than a total surface. Therefore we designed three tiny pillars with 1 mm diameter and 1 mm height on each surface where the steering mirrors had to be contacted. (see figure 7.1) After the workshop had built the spacer with the mentioned precision, the steering mirrors were clamped to pillars on the spacer. Starting with this simple Sagnac interferometer, a laser beam and a CCD (Charge-Coupled Device) camera the residual imperfection of the mirror angles could be monitored. The initial contrast was below 90%. By sanding and polishing (depending how hard it was misaligned) the three contact pins of each steering mirror one could control the horizontal and vertical angle of these very accurately. After polishing these adjustment pins iteratively the contrast could be increased to 99.9% [Ste14]. This technique was only used for the steering mirrors and not for the BS. The BS position and angle defines the complete level of the interferometers light field. The BS could be pressed to a surface without pillars and this was the reference for the alignment of the two steering mirrors. Another crucial issue for alignment was the torsional moment of the screws, because a too high pressure to the mirror could lead to a deformation of the adjustment pins. To avoid such damage we used a torque wrench with a very low torsional moment. This allowed to reproduce the alignment after loosening or changing mirrors. For the membrane position it was however indispensable to have the possibility of detune the membrane position to measure the contrast of the interferometer or to observe spectra at different fringe positions (dark-port, close to dark-port, mid-fringe, bright-port, etc.) Because of the good experiences which were made in the first cryogenic interferometer [Nia13], with positioner from attocube system AG [ATT17] the same also were utilized in this experiment. They allowed an alignment in a sub nm arrangement for all three directions. (more details see chapter 7.2). The future planed SRM was planed to use those positioners.

7.1.2. Spacer

The first step to a functional interferometer was to design the spacer. To keep the residual tilt of the optics as low as possible, one had to think about an optimal arrangement of the optics inside the spacer and the spacer form itself. A cylinder as basic form of the spacer seemed to be a very good solution. Because of the radial symmetric thermal deformation there was almost no contraction in the center of the cylinder. Thus we made a hole in the center for the BS, so that the reflective surface was exactly in the center of the spacer. For the steering mirrors there were two surfaces, which were cut into the curved surface of the cylinder, in a symmetric way with the same angle and distance to the BS surface. Thermal contraction would move the steering mirrors commonly, which would have almost no influence on the contrast of the interferometer. The membrane positioner stack was put in a cylindrical hole in the middle of the two steering mirrors. This arrangement had the advantage that the main deformations would almost be radially symmetric, which kept the angles between the optics quite stable. Only the asymmetric deformations lead to a misalignment of the Michelson Sagnac interferometer. Asymmetric deformation will be mainly caused by the cylindrical hole for the planed SRM. The SRM was an asymmetric but necessary optical part in the interferometer topology, which could not be avoided. The hole for the BS would also bring an asymmetric deformation. To put the reflective side of the BS exactly into the center the hole for the total BS should be slightly off center. Also the size of the interferometer played a role, because a tilted mirror, would cause much less misalignment if the optical pass would be shorter. So the design was optimized to kept the optical passes as short as possible. The resulting interferometer arm length was about 7.9 cm.

Before building the spacer one had to evaluate the material which should be used. The spacer of the former interferometer was made out of copper. The advantage of copper was the very high thermal conductivity (cf. figure 5.1). This allowed a good thermalisation of the interferometer with the cryostat, which resulted in a fast cool down of the membrane. The disadvantage was the also very high thermal expansion coefficient. In contrast the thermal expansion coefficient of the alloy of iron (64%) and nickel (36%), the so called Invar, was one order of magnitude lower than of copper. It provides a much higher dimensional stability over a range of temperatures. At that time the thermal conductivity of Invar is about 40 times lower than of copper [Gri89, Eki06], which would extend the cool down period. One could solve this by using several pure copper wires (as presented in chapter 7.3) for better thermalisation from the cold plate directly to the membrane holder which was the essential part to get fast cooling.

The third step was to simulate the residual deformation of the spacer to get an idea of the order of magnitude of the contraction. For the simulation the software *Autodesk Mechanical Simulation 2014/2017* were used. The

7. Realized Interferometers at Cryogenic Temperatures

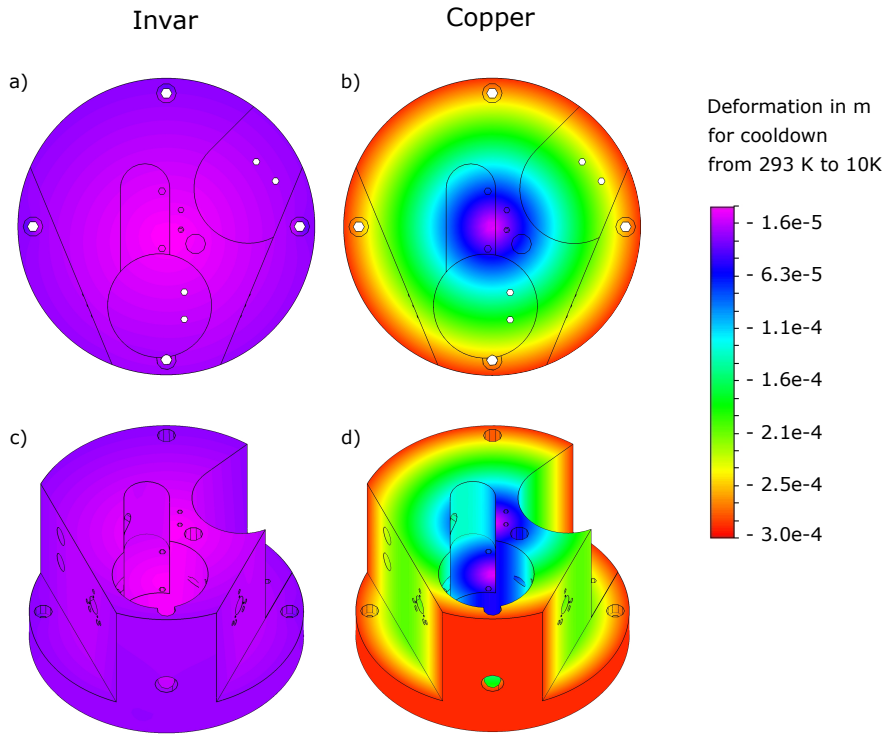


Figure 7.2.: *Thermal Simulation of Quasi-Monolithic Interferometer.* Figure a) + c) show the contraction of a spacer made of Invar and b) + d) for comparison a spacer made of copper. The deformation of the copper spacer is 1-2 orders of magnitude larger than the one of the Invar-spacer. Figures a) + b) show the top of the designed spacer which had in principle a cylindrical shape. Here it is clearly visible that the spacer deformation in both cases is almost radial symmetric. So that the main deformations are not crucial to the contrast of the interferometer.

simulation was a steady state thermal analysis where the dimension of the spacer was simulated at 10 K compared to the spacers initial dimensions at 293 K. The spacer was simulated with Invar material properties. The bottom line property for this simulation was the thermal expansion coefficient. In general thermal expansion of Invar is temperature dependent and decreases at lower temperatures. For this simulation the value was set to be constantly at the room temperature value $\alpha=2.0 \cdot 10^{-6} \text{K}^{-1}$, so the simulation gave a conservative result of the contraction of the spacer.

First simulation showed that the expected tilt of the steering mirrors and the BS induced by contraction of the Invar-spacer was in a range of $10^{-5} - 10^{-3} \text{ }^\circ$. This tilting could be optimized with an additional hole in the spacer. This extra hole antagonized the asymmetric deformation of the spacer. After a few iterative optimization steps the tilt range could be minimized to $2.4 \cdot 10^{-6} - 1.2 \cdot 10^{-3} \text{ }^\circ$ [Ste14]. On this simulation results one could calculate how much the contrast would decrease by cooling down the interferometer.

To keep it simple it was calculated only for the Sagnac mode. For starting the calculation the contrast was set to be perfect (100%) at room temperature, which means that the spots of the counter running optical fields are perfectly matching. After the cool down and the above shown tilting angles of the steering mirrors the centers of the two spots were separated by a distance of $3.6 \mu m$ [Ste14]. The assumed diameter of the spots was about $500 \mu m$. This means that after a cool down the two modes of the Sagnac interferometer would still overlapping with 98.9%. These were only estimated calculations, but they still gave a good idea which precision could be reached with the quasi-monolithic interferometer.

7.1.3. Measurement at 10 Kelvin

In the bachelor thesis of Morten Steinecke [Ste14] it was shown, that we could reach a contrast of 99.9% at 293 K for the Sagnac mode, which was the quasi monolithic part of the Michelson-Sagnac interferometer. During this thesis I upgraded this interferometer with a electronically adjustable SiN-membrane to measure the contrast of the total Michelson-Sagnac interferometer. Here it also was possible to align the total interferometer to get a contrast of 99.9% at room temperature. The next step was to put the interferometer inside the cryostat and observe the contrast while cooling down the interferometer to 8 K and compare the simulation results to the real behavior of the interferometer with the spacer out of Invar. After cooling down the interferometer the contrast decreased to about 55%. This was much worse than expected from the simulation results. Three different reasons might cause this discrepancy:

- **Variant dimensions between designed and build spacer:** Since the accuracy of the workshop was limited there might be some differences in the dimensions between the designed and simulated spacer and the actually built spacer. Especially the position of the additional hole for optimization of the deformation was crucial. Changes in the depths and position of this hole might have caused a different behavior than simulated. Also the workshop was not able to drill the depth of all screw holes for the steering mirror plates as it was designed. This as well could be a reason for the higher deformation as expected.
- **Unequal behavior of screws:** In the ideal world the contraction of the screws with which the steering mirrors were pressed to the spacer, would contract in the same way. But in the real world the length of the screws might be slightly different or the material of the screws could be inhomogeneous. This would cause a different contraction and so an unequal pressure to the mirrors surface and to the three small pins on the spacer, which resulted in a tilted mirror.
- **Different thermal expansion:** When this observation was done the screws were out of stainless steel and the holding plates, in the back

7. Realized Interferometers at Cryogenic Temperatures

of the mirrors, were made out of aluminum. Both materials have one order of magnitude higher thermal contraction than Invar (cf. figure 5.2). Using screws and holding plates from Invar would definitely reduce the misalignment, but not exclude the unexpected deformation. The two above mentioned issues would still play a role, but in a smaller dimension.

7.1.4. Conclusion

Overall the quasi monolithic interferometer was an improvement compared to the former one. While the contrast of the former decreased from 97.4% to almost 20% [Nia13], the quasi monolithic interferometer could be aligned to a contrast of 99.9%. Although there was a discrepancy between the predicted high contrast by the simulations and the actually measured contrast of about 55%, it was an improvement to the contrast of the former interferometer. The results, especially the simulations, exhibit that Invar had a really high mechanical stability over a large temperature range. Also the idea using small pins for adjustment and contacting the steering mirrors, worked very well. Only by sanding the pins by hand this stunningly high contrast was reached at room temperature.

The biggest mechanical problem was to control the pressure of the steering mirrors to the spacer. On the one hand there was the torsional moment of the screws. Although a torque wrench was used the adjustment was not as reproducible as hoped. We observed a hysteresis in that after loosen and tightening the screws several times it was not possible to get the high contrast with the adjusted torsional moment again. So one had to start from the beginning and sanding and polishing the pins again. One reason was that the small pins with the tiny surfaces were deformed by the pressure. On the other hand there were the uncontrollable changing pressures to the mirrors during cooling down the interferometer. A more fundamental issue was shown in the simulation results. Although the material for the spacer had a very low thermal expansion coefficient the misalignment caused by contraction of this material only was still too high. A resulting contrast below 99% was definitely not good enough for detection of radiation pressure noise with the necessary and in future planned signal recycling technique (cf. chapter 6). To solve these issues one could make the screws and the holder plates out of Invar and additionally try to reduce the interferometer size. To get decisive improvements by changing the size one would have to build an interferometer at least one order of magnitude smaller. This seems to be almost impossible. So the better option was to follow a different idea, and try to make all optics remotely adjustable, which is described in the next chapters 7.2-7.3.

7.2. Electric adjustable Interferometer of Copper

In this chapter the idea was followed to design a total electrically adjustable interferometer. The starting position was the first interferometer which operated at 8 K in 2012 and 2013 [Nia13, Kau13]. While first spectra at 8 K were measured, it also revealed a few difficulties. The biggest issue were determined by the holders of the steering mirrors, which were mechanically adjustable by screws. These holders caused a high misalignment after cooling down the interferometer to about 8 K. So the idea was to exchange the mechanical holders by newly designed electrically adjustable positioners. Apart from the steering mirror holders the new interferometer was almost designed as the former one (cf.7.3).

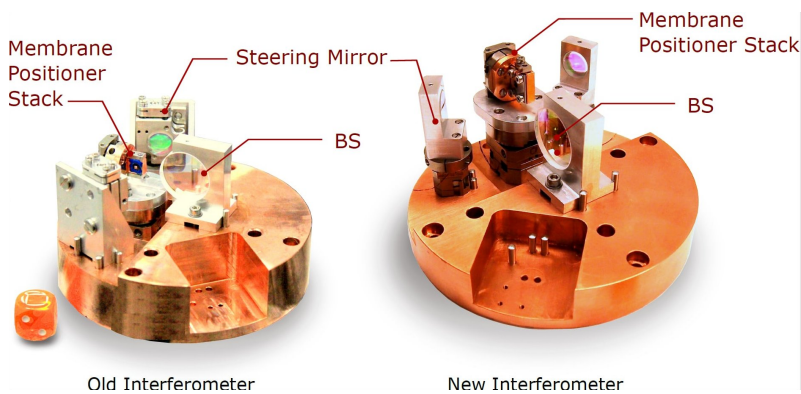


Figure 7.3.: *Electric Adjustable Copper-Interferometer.* The big difference of the new designed interferometer to the old one, were the positioner stacks for the steering mirrors. For the rest it stayed quite similar. All optics were also based on a copper plate. Except the BS all optics were tunable by positioners, which were electric driven by piezos. This was a big advantage compare to the old interferometer setup. It gave the possibility to realign the interferometer after cool down from outside the cryostat.

7.2.1. Interferometer Design

Designing a new interferometer setup required a development of various sections and and their interlock. As there were the base plate, beam splitter mounting, positioning and mounting of membrane and steering mirrors.

Base plate

As the former at the former interferometer the base plate was designed to be out of copper. Although the thermal expansion of copper was very high, it was not as crucial as for the quasi monolithic interferometer, because deformations due to cool down could be compensated by electronic adjustments

7. Realized Interferometers at Cryogenic Temperatures

of the positioners from outside the cryostat. So in this situation it was more important to choose a material with high thermal conductivity.

Beam Splitter

The BS was clamped into a mounting made out of aluminum. This holder was screwed to the base plate. The BS was the only optical part of the interferometer, which was fixed and not adjustable. So the BS was the permanent reference to all other optics, which were designed to be tunable via electrical positioners. If the BS was tilting due to the cool down process the other optics could be realigned using the BS as reference.

Attocube-Positioners

All positioners for this interferometer were provided by the company **attocube system AG**. These positioners were perfectly suitable for the extreme environment in the experiment. Made from titanium, ceramics and special twisted pair wires out of copper, the outgassing of these devices could be reduced to a minimum. Therefore they were appropriate for ultra high vacuum environments down to 5^{-11} mbar, which was fine for our vacuum of $2^{-7} - 5^{-6}$ mbar. Furthermore they were conceived for ultra low temperatures down to 10 mK. The high resolution of positioning was in a range of sub-nm and μm and gave the opportunity to align the interferometer much more accurate than alignment by hand. The actuators in the positioners were piezoelectric ceramics. The innovative matter of this positioners was the stepping and positioning technique. They used a spring-clamped technique, which means by using sawtooth shaped voltage pulses (0 – 150V) the optics could be moved, but to hold them in place there was no voltage applied to the piezoelectrics. It was mechanically fixed by the spring-clamped technique. This was an advantage because there was much less noise coupling into the experiment through the voltage supply of the positioners. The residual noise could be suppressed by two integrated electronic low pass filters with the corner frequency of 16 Hz and 160 Hz [ATT17]. An additional benefit of these positioners was the size. They were very tiny (cf. figure 7.5,7.4) which allowed to design an interferometer with short armlength and cavity length. This was important to get a broadband signal-recycling cavity and more mechanical stability of the interferometer.

Membrane Positioner Stack

The membrane was clamped or glued to a copper holder. This mounting was made out of copper, to have a good thermal contact and conductivity to the membrane. The holder was screwed to a stack of positioners from **attocube system AG** which made it easy to exchange the membrane. By this positioner stack the vertical and horizontal angle of the membrane could be tuned.

Also it was possible to oscillate the membrane position in direction of the light field, to observe the interferometer fringe and measure the contrast (cf. figure 7.4). While it was very import to have the possibility to align the membrane it also was very essential to have a good thermalisation of the membrane with the cold part of the cryostat. But due to the positioner stack, made out of titanium and ceramic, the thermal conductivity from the membrane to the copper base plate was declined a lot. To sustain a good thermal contact, despite the positioner stack, a few twisted copper wires were connected to the copper membrane mounting an directly connected to the cold plate of the cryostat. So both requirements, electrical adjustability and high thermalisation, were fulfilled.

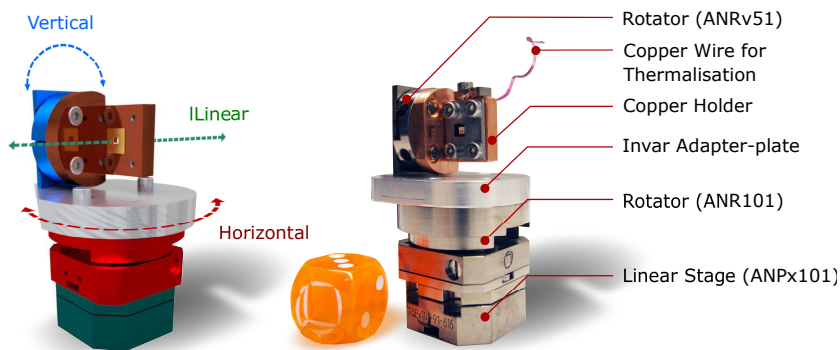


Figure 7.4.: *The Membrane Positioning Stack.* The membrane itself was clamped to a copper holder. A few copper wires were also clamped to this holder and lead to the 10 K cold plate, for better thermalisation. The copper holder was mounted to a rotator (blue) for vertical alignment. A second rotation positioner (red) was for horizontal adjustments. Between this two rotators was an adapter plate made out of Invar. The lower positioner (green) was a linear stage to shift the membrane in the direction of the propagating light field inside the interferometer.

Steering Mirror Positioners

The steering mirror mounting were also designed with a positioner stack (cf. figure 7.5). With a Goniometer-Positioner (Model:ANGt50) it was possible to tilt the mirror in the vertical direction over a range of 7.2° . On top of the Goniometer a Rotator-Positioner (Model: ANR50) was screwed for adjustments in the horizontal direction. The range of this positioner was 360° . With these two positioners both steering mirrors could be aligned with an accuracy of μ° [ATT17].

7. Realized Interferometers at Cryogenic Temperatures

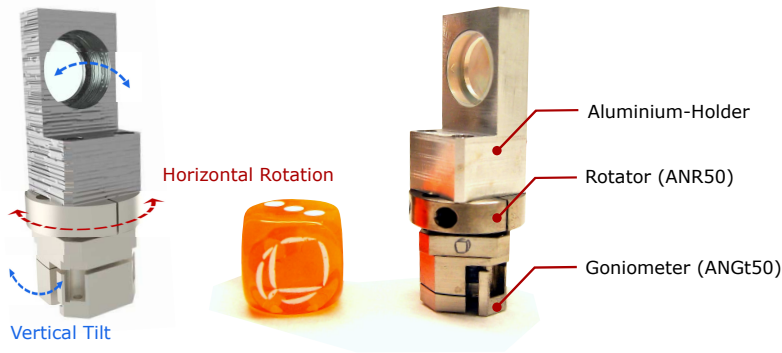


Figure 7.5.: *New Concept for Steering Mirror Mounting.* The steering mirrors were maintained by holders made out of aluminum. Underneath there was a stack of two AT-TOCUBE positioners. The bottom one was a Goniometer-Positioner which was able to tilt the mirror in the vertical angle. The upper positioner was a Rotation-Positioner which allowed to align the steering mirror in the horizontal angle. This positioners were both driven by piezos and provide an accuracy alignment in a sub nm range.

7.2.2. Interferometer Alignment Process

The alignment process of the interferometer was tricky. It was impossible to align the interferometer without any references. So one could not put the total interferometer inside the cryostat and align it afterward with the positioners, because there were 4 optical parts and there was no chance to know, which of them was misaligned. The point was that the interferometer had to be attached upside-down to the cold finger, which was on the lid of the vacuum chamber. The lid had to be closed to have the mirrors of the interferometer at the optical beam height of the view ports and the laser beam. That was the reason why in general the interferometer first had to be aligned on air and at 293K and afterward it could be put into the cryostat and then the final alignment could be done. To get a well aligned interferometer inside the cryostat at 293 K and 8 K one had to follow an alignment procedure consisting of 7 steps:

- **1st step:** Match the optical mode with the two lenses in such a way, that the waist was exactly at the same distance of the flip mirror as the membrane would be. To monitor this a beam analyzer was used. One should also consider that the size of the waist should be about 5 times smaller than the membrane size to avoid clipping losses. Here the waist diameter was set to about $300\mu\text{m}$.
- **2nd step:** Now the alignment of the interferometer in free space could be started. The base plate had to be positioned at the right distance from the flip mirror and the BS was screwed to the base plate. By rotating the whole base plate the splitting ratio to 50/50 was tuned as precise as possible.

- **3rd step:** After the angle of the BS was aligned, the steering mirrors had to be adjusted. The alignment of this simple Sagnac interferometer could be monitored by the CCD camera and a photo diode.
- **4th step:** The next step was to include the membrane on the positioner stack and adjust the membrane. Also here the adjustments could be monitored by the CCD camera. For the fine alignment one could scan the position of the membrane with the ANPx101 positioner and monitor the contrast with a PD.
- **5th step:** Now the interferometer was completely aligned. The next step was to install the interferometer inside the cryostat. Because of the cryostat concept the interferometer had to be screwed upside-down underneath to the cold plate. In doing so one had to be very careful to not tilt the optics of the interferometer.
- **6th step:** After it was fixed to the top of the cryostat the angle between the incoming beam and the beam splitter had to be adjusted roughly by rotating the top of the cryostat, which stand on the vacuum chamber. Thereafter the fine adjustment to match the already in it self aligned interferometer mode with the incoming beam could be done by the mirror set outside the cryostat. Now the mode matching lenses could also shifted again to have the mode matching perfectly matched to the final position of the membrane. After this step the alignment of the interferometer was finished for measurements at 293 K.
- **7th step:** For measurements at cryogenic temperatures one had to cool down the interferometer, and during the cool down the interferometer could be realigned by using the positioners for the membrane and steering mirrors. The difficulty here was to figure out which optics were misaligned. This could be found out by tilting the membrane such that in the output on the CCD camera the Michelson mode and Sagnac mode were separated. Now it could be verified if the Sagnac output was dark (good aligned) or not (misaligned). If not, the Sagnac mode respectively the steering mirrors were misaligned. After realigning the Sagnac mode one by the steering mirrors one could tilt the membrane back and match the Michelson mode to the Sagnac mode by tilting the membrane.

7.2.3. Measurement Results

The pivotal question for this electrically tunable interferometer was: which interferometer contrast could be achieved with the new positioners at cryogenic temperatures?

High Contrast at 8 K

Following the alignment procedure step by step it turned out that the posi-

7. Realized Interferometers at Cryogenic Temperatures

tioners performed very well, and compared to the former cryogenic interferometers a very high contrast of 99.5 % as well at 293 K as at 10 K, could be reached. Further improving the contrast was not possible, because of the not perfectly balanced beam splitting ratio. It turned out that a more precise alignment of the beam splitting ratio, was not possible due to the used alignment process. After putting the interferometer into the vacuum chamber the alignment of the beam splitting ratio, by rotation the upper part of the cryostat, was only roughly possible (Step 6 described in the previous section). The reason was, that it lays on the rubber seal, which was between the vacuum lid (screwed to the cryostat) and the vacuum chamber (fixed to the optical table). The upper part of the cryostat had a weight of about 20 kg and therefor the friction was too high for smooth rotation, even with vacuum grease. This not perfectly balanced beam splitter ratio, could not be total compensated by the mirror set outside the cryostat, because of the very small range for a beam shifting. The limit for the beam shift was given by the view ports of only 15 mm diameter, half inch optics inside the interferometer and the small membrane with a square of around 1 mm. But since this contrast value did not limit the measurement results for this interferometer design, it was quite sufficient for the first performing test in a cryogenic environment.

Spectrum at 10 K

Figure 7.6 shows two measurements of the displacement noise around the fundamental mode of the membrane at 293 K and 8 K. The temperature was not measured at the membrane directly, but at the sample holder. It was assumed that after some waiting time the membrane was in a thermal equilibrium with its environment (interferometer + sample holder). A good indicator which showed that the membrane was in a thermal equilibrium was the fundamental resonance frequency. The resonance frequency was lowered during the cool down due to internal stress changes between the membrane and its frame. During the cool down the resonance frequency shifted over 11.53 kHz from 151.4 kHz to 139.87 kHz. After the sample holder had reached the 10 K and was held there for several hours a constant frequency at 10 K indicated that the membrane also reached the 8 K.

The input power for both measurements was 100 mW. To keep the laser noise low, the membrane was positioned close to the dark fringe and the spectra were detected with the subtraction technique. Therefore the dark noise clearance was very low. The resulting spectra were limited by the sum of dark noise, shot noise and the thermal noise. Due to the cool down the sensitivity next to the peak was increased by more than an order of magnitude to $3 \cdot 10^{-16}$ m/Hz^{1/2} which matched very well with the theoretical calculations of the resulting output. To improve the sensitivity the power had to be increased to get a better dark noise clearance and a better shot noise to signal ratio. On the way to observation of radiation pressure noise the power will have to be at least several Watts.

Vibration Noise Peaks

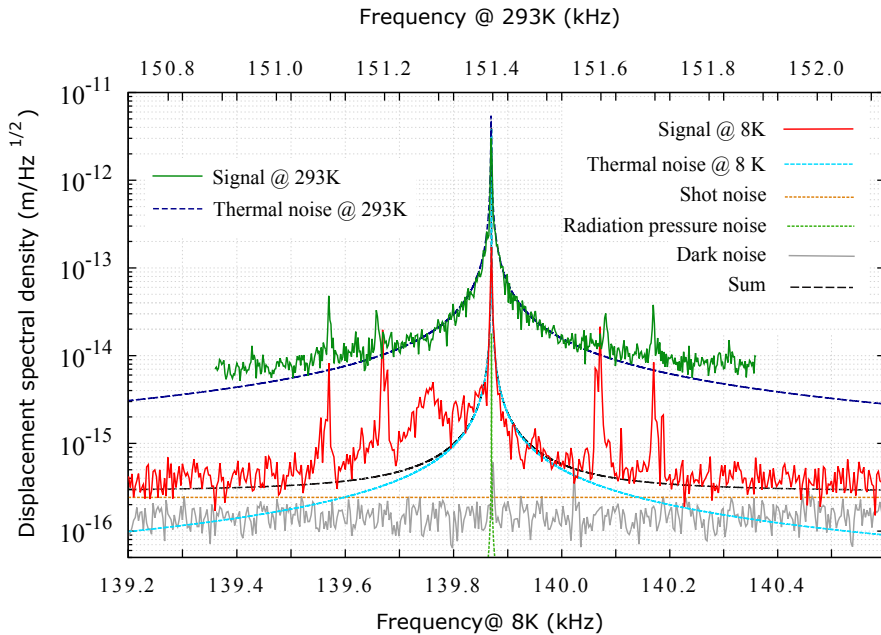


Figure 7.6.: *Displacement Spectrum at 293 K and 10 K.* This figure shows the membrane displacement spectrum around the fundamental mode for two different temperatures and an input power of 100 mW. Both were calibrated by the known thermal noise [Saw12]. The signal measured at 293 K is displayed with a solid dark green line. The dashed dark blue line shows the calculated thermal noise at 293 K for the membrane. The fundamental resonance frequency here was at 151.4 kHz (top frequency axis). The red line shows the signal measurement at 10 K for the same membrane and input power. Due to cool down the resonance frequency shifted to 139.87 kHz (bottom frequency axis). The calculated thermal noise at 10 K is represented by the light blue line. Off resonance the measurement was limited by the shot noise (orange dashed line) and the dark noise (gray line) of the photo diode. The calculated sum of thermal noise, shot noise and dark noise match the measurement very well. The calculated radiation pressure noise is about two orders of magnitude below the signal measurement. In this figure one can see only the peak which is displayed in a dashed green line. The satellite peaks which were ± 200 Hz and 300 Hz beside the membrane peak were induced by vibrational noise.

Increasing the power bore two issues in particular. The first one was that higher powers enhanced noise peaks which appeared next to the fundamental mode at ± 200 Hz and ± 300 Hz. These satellite peaks were beats between the resonance peak of the membrane and some noise sources at 200 Hz and 300 Hz in the lab. The noise sources could not be located, but electronic noise induced by the piezos could be excluded, because the satellites were present even if the positioners were disconnected. Thus they coupled into the interferometer through the mechanical parts of the interferometer. A closer look to the measurements done with the very first cryogenic interferometer, presented in [Nia13, Kau13], revealed that even at those measurements small peaks at ± 200 Hz were visible, but not at ± 300 Hz. In those measurements the ± 200 Hz satellites were almost not visible, because the sensitivity of that

7. Realized Interferometers at Cryogenic Temperatures

interferometer was worse, so the peaks were almost mask by the laser noise. The main change of the new, remotely controllable interferometer compare to the first one, were the positioner stacks for the steering mirrors. This positioner stacks also seemed to be the shakiest parts in the interferometer design and sensitive to external vibrations. Assuming this, the ± 200 Hz satellites might be caused by the membrane positioner stack, as this stack was principally similar to the positioner stacks of the membrane. The membrane positioning stack was identical to the one used in the first cryogenic interferometer. The difference of the positioner stack of the membrane to those of the steering mirrors, were the mass and the size of the positioners. These differences could explain the lower frequency of ± 200 Hz.

A closer look to the positioner stacks of the steering mirrors and the membrane gave the impression that especially the rotator axes were highly susceptible to vibrations. To got a better sensation a modal frequency analysis of these positioner stacks were done with the *Autodesk Inventor Professional 2014/2017* software. This analysis had revealed that their two first eigenfrequencies were between 400 Hz and 500 Hz (cf. 7.7). This value deviated from the measured frequency of the satellite peaks. The reason was that for this analysis only the *simplified* 3D CAD (computer aided design) drawings of the positioners were available, which were specially made for customers from the company **attocube system AG**. In this simulation the positioners were modeled as a bulk material, especially the rotator axes. In reality the top of the rotator was screwed to the axis, which actually were not fixed but movable. This was true for the whole positioners which were built together of many different small pieces. This could cause the difference of measured satellites to simulated eigenfrequencies. The fact that the positioners were cooled down from 293 K to 10 K could not cause the difference of real measured and simulated modal frequencies, because the temperature change had a small effect to the modal frequency shift, as the two measurements at different temperatures presented in figure 7.6 showed. Although the analysis quantitatively not precise, it gave a qualitative idea where the noise might coupled in. In principle this position oscillation would change the phase inside the arms of the interferometer and transfer into amplitude oscillations at for example 200 Hz and 300 Hz.

As long as the displacement sensitivity was only about 10^{-14} m/ $\sqrt{\text{Hz}}$, around the membrane resonance peak, the satellites were not an issue for spectrum measurements. But as soon as the sensitivity increased as shown in the measurement in figure 7.6 the vibrational induced satellites became more crucial. For even higher input powers (increasing sensitivity), which was necessary for the observation of RPN, the signal would be masked by these satellites.

An other issue with high power was the detection scheme used so far. At an input power of 1 W and a contrast of 99.5% the output power in the dark fringe would be about 5 mW. To have still an almost shot noise limited spectra the detected power of the LND-PD (see figure 6.1) should be at least 50 mW. This would be hard to manage with an InGaAs PD, as

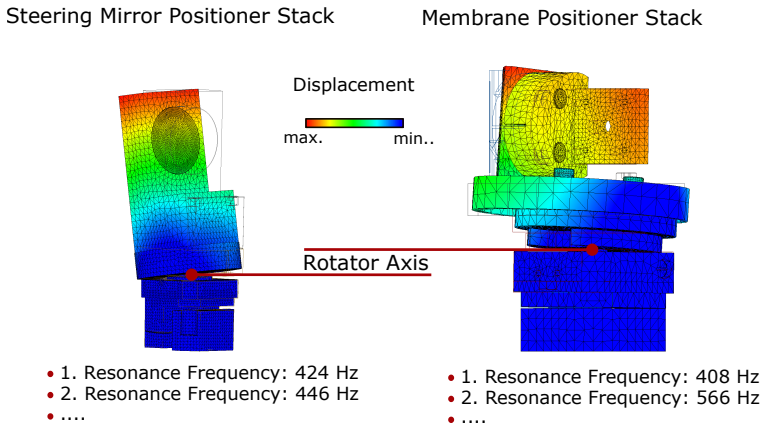


Figure 7.7.: *Modal Frequency Analysis.* The modal frequency analysis of the steering mirror and membrane positioner stacks have shown that the shakiest part of the stacks were the axes of the rotation positioners. The first two resonance frequencies are between 400 - 500 Hz. The 3D CAD drawings of the positioners used for this analysis were simplified, so that in the real experiment the resulting modal frequency could be shifted.

used so far. A better contrast $>99.9\%$ would help out here, and reduce the output power to sub 1 mW. An even better contrast and operation at (almost) darkport would avoid the laser noise subtraction method. In this case a balanced homodyne detector is required. Because of the external LO the signal does not need carrier light field in the output of the interferometer.

Measurement with Balanced Homodyne Detection

After realizing a balanced homodyne detector it was found out, that only low input power of up to 10 mW could be used. The reason was that at higher input powers the amplitudes of the noise peaks of ± 200 Hz and ± 300 Hz were very high and saturated the homodyne detector. Because of these fluctuations, it also was impossible to lock the phase between the LO and the signal. This lead to fluctuations of the height of the membrane resonance peak, because the quadrature was fluctuating. One could only hold the phase constant by hand for a few seconds and measure the spectrum with low resolution bandwidth.

7.2.4. Conclusion

The adjustable interferometer of copper was a big improvement in comparison to our previous cryogenic interferometers. The big issue of a high contrast at cryogenic temperature was almost solved. With the new electrical positioners it was possible to reach a contrast of 99.5%. The performance was quite promising. With better beam splitting ratio, even a higher contrast could be reached. Nevertheless with a contrast of 99.5% it was possible to measure a spectrum at 10 K with the highest observed sensitivity in our

7. Realized Interferometers at Cryogenic Temperatures

group so far, of $3 \cdot 10^{-16} \text{ m}/\sqrt{\text{Hz}}$.

The biggest issue this interferometer had, were the vibrational noise peaks, which limited further sensitivity improvements. This could be solved by a more mechanical stable interferometer design (see next chapter 7.3) and an additional vibration isolation platform (cf. chapter 5.3.3).

7.3. Adjustable cooled Interferometer of Invar

The purpose of the final interferometer design of this thesis was to combine the advantage of previous versions. Whereas the quasi monolithic interferometer had a very high mechanical and dimensional stability over a big temperature range, the second interferometer had the alignment flexibility due to the electrical positioner. The mechanical and dimensional stability was necessary to avoid vibration coupling into the interferometer and the electrical alignment flexibility was essential to reach a high contrast value at low temperatures.

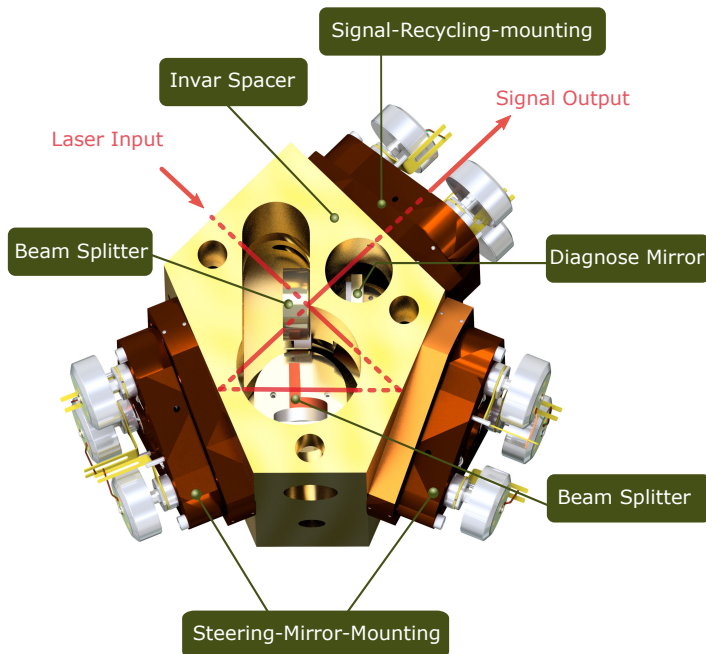


Figure 7.8.: *Adjustable Cooled Interferometer of Invar.* The final interferometer of this thesis used a gold coated Invar spacer to provide dimensional stability. The Steering mirrors (STM) and the signal recycling mirror (SRM) could be mounted by quasi-monolithic tip and tilt stages from Janssen Precision Engineering (JPE) company. The membrane positioner stack was screwed into a hole between the steering mirrors. The beam splitter was clamped onto the spacer. An additional diagnose mirror could be rotated into the light path between beam splitter and signal recycling to monitor the interferometer output excluding the signal recycling mirror.

7.3.1. Robust and Adjustable Interferometer Design

The bottom line innovation the realization of a quasi-monolithic interferometer with adjustable steering mirrors, signal-recycling mirror and membrane.

Steering Mirror Mounting

The steering mirror clamped directly to the spacer was a quite stable solution in the previous quasi monolithic interferometer (cf. chapter 7.1). The main problem with this clamping technique was the changing force during the cool down, which came along with misalignment. The basic idea was to change the screws with the piezoelectric "*Cryo Linear Actuators*" (CLA) from **Janssen Precision Engineering** (JPE) company. After discussion with the company, they came up with a customized all in one tip and tilt stage. (see figure 7.9) The steering mirror was fixed with a mirror socket to the stage, and the stage was screwed to vertical surfaces of the spacer (see figure 7.8). The connecting surface of the stage was as large as possible to have a very stiff contact, which suppressed internal vibrations of the stage. While the outer frame, in figure 7.9 shown in blue, was screwed to the spacer, the inner triangle, presented in green, was movable by the three CLAs. The inner part was tightened by stiff springs to the CLAs, in such a way, that this section with the mirror on it, also was very stiff and insensitive to vibrations. The very low step size of the actuators was 5 nm-25 nm at 293 K and about 1-5 nm at 4 K, allowing a precise alignment of the mirrors. The total range of ± 1.5 mm was sufficient to compensate the misalignment during the cool down multiple times.

The outer fixed triangle (blue) and the inner flexible triangle (green) was a monolithic piece of bronze. The inner triangle was flexible because it was only connected to the outer triangle with flat springs, which were shaped out of the bulk material. This stiff springs pressed the inner triangle against the linear actuators with a force about 40 N. This composition made the mirror in the center of the inner triangle insensitive to vibrations. While copper had a much higher thermal conductivity, only bronze guarantees the reset force of the springs and the overall stiffness. In principle other materials as Invar or stainless steel would also provide quite similar stiffness but even lower thermal conductivity. The most suitable material for the mirror socket was Invar. Here the most important property was the low thermal expansion coefficient. As the mirrors, made out of fused silica, had a very low contraction during the cool down, the socket should have similar thermal contraction to avoid increasing stress during the cool down (cf. figure 5.2).

Spacer

Similar to the quasi-monolithic interferometer in chapter 7.1, a spacer made from bulk material was used and not a breadboard as in the previous interferometer. A spacer with holes for the laser beam paths, provided higher

7. Realized Interferometers at Cryogenic Temperatures

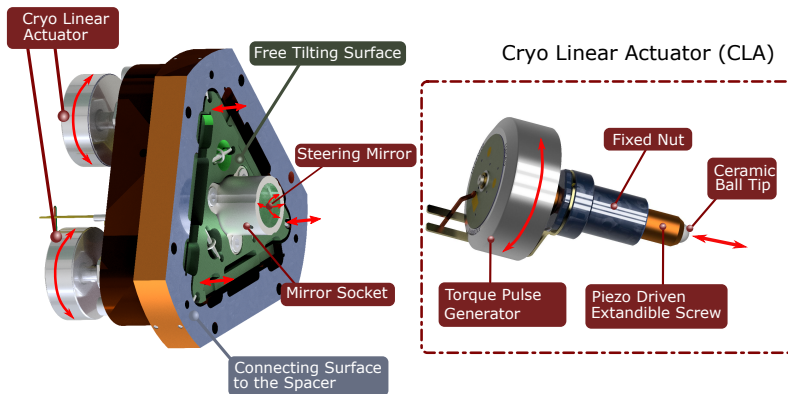


Figure 7.9.: *Steering Mirror Mounting to Invar Spacer.* The total mounting device for the steering mirrors was customized by Janssen Precision Engineering (JPE). It was designed as a tip and tilt stage with the steering mirror located in the center. Tilting in all direction was achieved by three "Cryo Linear Actuators" (CLA) from the same company. The CLA were piezoelectric driven linear actuators, which could shorten and extend their length by a torque pulse generator [JPE17]. The total tip/ tilt stage was clamped to the spacer, which gave a high dimensional stability to mirror positioning.

mechanical stability by screwing the optical parts vertical against the spacer surfaces. Although the new positioning stages for the steering mirrors were quite large, it was possible to reduce the arm length of the interferometer to 6.1 cm, which was about a reduction of 20% compared to the previous one. This reduced the misalignment due to tilting of the steering mirrors, and shortened the signal-recycling cavity, which resulted in a higher cavity bandwidth. Because of the big CAL stages, and the short arm length, it was not possible to keep the spacer in a cylindrical shape as in the quasi-monolithic interferometer. The deformations during a cool down were thus expected to be higher. Even though it was possible to compensate the deformations with the tunable mirrors, the spacer still was made out of Invar to prevent too high deformations.

Beside its advantage Invar also comes with disadvantages when compared to copper. The first was the higher specific heat capacity, which extended the cool down time by at least a factor of two for the temperature range 293 K to about 75 K. For lower temperatures the specific heat capacities were almost the same. The second disadvantage was the three times higher emissivity at room temperature, which led to an almost three times higher absorption of radiation from the heat shield. To reduce the absorption, the Invar spacer was polished and gold coated ($1\mu\text{m}$ coating thickness) A further benefit of the gold coating was the improvement of thermal conductivity at the interface between the spacer and the pure copper adapter, and also at the interfaces of the mirror positioning stages.

Membrane Mounting and Cooling

The membrane was mounted on the same positioner stack used in the previous interferometer. Although this positioning stack could cause satellites with ± 300 Hz, it was not changed because of two reasons. There was no solution found to made the mounting of the membrane more stable but still electronically adjustable, without changing the size if the interferometer. A positioner like the ones for the steering mirrors, were not possible unless the interferometers spacer would be designed to be 3-4 times larger than the present one. This would also make it necessary to increase the cooling chamber far more than it already was done (cf. section 5.3). Since it was not certain that the membrane positioner stack was sensitive to incoupling vibrations from outside, the better way to get ride of the vibrations was to install a passive vibration isolation platform, which is described in section 5.3.3. Besides we had good experiences with passive vibration isolation in general, which were implemented into the signal recycled interferometer, operating at the wavelength of 1064 nm (described in chapter 4). This passive vibration isolation was implemented during my master thesis [Saw12] in collaboration with H. Kaufer [Kau13]. Although the setup was quite different and based on rubber instead bronze springs, it demonstrated that passive damping is a useful approach against the satellites.

Since the membrane is the important part to cooldown and the thermal conductivity of the membrane positioning stack (made out of titanium) was very low, I implemented a pure ultra flexible copper wire (cross section: 0.32 m^2 / length= 12 cm) to increase the thermal contact to the sample holder. It connected the copper membrane holder directly to the pure copper adapter plate at the sample holder. Thereby the lower thermal conducting vibration isolation platform, the Invar spacer and the titanium positioner stack could be bridged. A silicon temperature sensor was used to monitor the membrane temperature.

Signal-Recycling Mirror Mounting and Alignment

For the signal-recycling mirror it was planned to use the same stage as for the steering mirrors. For the alignment the three CLAs could also be used for parallel shifts of the signal-recycling mirror in the direction of the light field to match the radius of curvature to the optical mode of the interferometer. The distance of the signal-recycling mirror to the beam splitter was designed to be 38 mm, resulting in a total cavity length of 9.9 cm. The signal-recycling mirror had a power reflectivity of 99.93 % and a radius of curvature of 10 cm. With these specifications the cavity length depended highly on the waist size of the optical mode at the membrane. The waist size range was limited by the membrane size. To avoid losses due to clipping at the membrane the waist size should be 1/5 of the membrane size. During the experiments different membrane sizes from 0.5 mm x 0.5 mm to about 2.5 mm x 2.5 mm were used. To fulfill the optical stability criterion of the signal-recycling

7. Realized Interferometers at Cryogenic Temperatures

cavity the length $L=9.8$ cm of the cavity should be smaller than the radius of curvature of the signal-recycling mirror $R_{SRM}=10$ cm, which was fulfilled by the new interferometer design. As mentioned above the fine adjustment of the cavity length could be done by the CLAs of the stage, which were able to shift about ± 1.5 mm. This new interferometer design was conceived in such a way, that even future unscheduled but necessary bigger changes of the cavity length could easily be done by a redesign of the signal-recycling mirror socket (quite similar to the steering mirror once). Due to building new mirror sockets the cavity length could be changed by ± 1 cm, which should give a large enough range for different optical needs.

7.3.2. Optimized Interferometer Alignment Process

To improve the alignment of the beam splitter angle with respect to the incoming beam, a positioning ring table (PRT) was developed. The idea of the PRT was to have the possibility to align the interferometer at its final position, mounted upside down to the cryostat, which also could be smoothly rotated. Therefore a ring made out of aluminum was designed, where the new lid (cf. figure 5.6) directly fitted into the inner diameter of the ring. The ring was laying on three posts, which had exactly the same height as the vacuum chamber. The posts were cylinders with a cut of surface. They were screwed to the ring slightly off their own center, so that the cross section of the posts were not overlapping to the inner side of the ring. But if the post was rotated the off center fixation led to a small overlapping surface of the post's cross section to the inner side of the ring of about 5 mm. The new alignment process with this PRT was as following:

- **1st step:** The optical mode was transformed with two lenses and two mirrors in such a way, that the position of the waist ($w=120\mu m$) was at the center of the cryostat (beam splitter surface) plus the arm-length of the interferometer. This position matched the distance to the membrane to be implemented later. A beam analyzer was used for monitoring the alignment of the waist. The waist was about 5 times smaller than the membrane size to avoid clipping losses.
- **2nd step:** Now the positioning ring table PRT was screwed to the table at the final position of the cryostat. The posts were rotated to have an overlapping surface to the inner side of the ring. Also the interferometer spacer including just the beam splitter was screwed to the cryostat. Afterward the cryostat with the new lid was put onto the PRT. As the diameter of the new lid was equal to the inner diameter of the ring, it went through until it was stopped by the slightly overlapped surfaces of the posts. Because the posts had the same height as the vacuum chamber, the cryostat and the upside down fixed interferometer were at this step already at its final position.
- **3rd step:** The cryostat was rotated to adjust the beam splitting ratio,

which could be monitored by a power meter. Because the cryostat lid was just laying on the small overlapping surfaces of the legs (low friction), it was possible to rotate the cryostat very smooth and with a precision of about 0.16° .

- **4th step:** The steering mirrors were mounted and adjusted. This was possible without moving the spacer, since they were visible. The alignment of this simple Sagnac interferometer could be monitored by the CCD camera and a photo diode.
- **5th step:** The next step was to include the membrane on the positioner stack and adjust the membrane. Therefor the total cryostat had to be lifted up. But before doing so the rotation position of the cryostat was marked on the PRT. Experiences had shown that with this mark, it was very simple to reposition the cryostat after the membrane positioning stack was included. The adjustments of the membrane could be monitored by the CCD camera. For the fine alignment one could scan the position of the membrane with the ANPx101 positioner and monitor the contrast with a PD.
- **6th step:** Now the interferometer was completely aligned and already at its final position. The next step was to install the vacuum chamber. Therefor the cryostat was lifted up again. The posts of the PRT were rotated in such a way, that the overlapping surface on the inner side of the ring vanished. As the vacuum chamber had the same diameter as the lid of the chamber and the inner diameter of the ring, the vacuum chamber was put through the ring onto the optical table. Thereby the position of the chamber was defined by the PRT.
- **7th step:** In this next step the lid of the chamber was also put through the PRT and lay onto the vacuum chamber. The cryostat had to be rotated to match the mark on the PRT, to reposition the beam splitter angle. Afterward the very fine adjustments were done by the mirror set and the lenses outside the cryostat. After this step the alignment of the interferometer was finished for measurements in vacuum at 293 K.
- **8th step:** For measurements at cryogenic temperatures one had to cool down the interferometer, and during the cool down the interferometer could be realigned by using the positioners for the membrane and steering mirrors. The difficulty here was to figure out which optics were misaligned. If signal recycling was already included one had realign the interferometer first, i.e. using an output beam that did not "see" the signal-recycling mirror. This could be done by the electric adjustable diagnose mirror, which was placed between the beam splitter and the signal recycling mirror on a rotation mount. By rotation the diagnose mirror into the beam path the signal-recycling mirror was blocked and the interferometer output beam could be steered out the vacuum chamber and monitored by a CCD and PD. Additionally the

7. Realized Interferometers at Cryogenic Temperatures

membrane had to be tilted in such way, that the Michelson mode and Sagnac mode were spatially separated on the CCD camera. Now it could be verified if the Sagnac output was dark (good aligned). If not, the Sagnac mode, respectively, the steering mirrors were misaligned. After realigning the Sagnac mode one could tilt the membrane back and match now the Michelson mode to the Sagnac mode. And then the diagnose mirror could be rotated back and the signal-recycling mirror could be aligned as the last part of the interferometer.

7.3.3. Measurements

This section presents the first experimental results of the new interferometer. The interferometer was mounted upside-down into the modified cryostat. Figure 7.10 shows the interferometer mounted to the copper adapter plate (lower copper plate). The copper braids provided a faster thermalisation of the interferometer. For the same reason an additional copper wire connected the membrane holder and the upper copper plate. The temperature at the membrane mount was measured by a silicon diode temperature sensor (cf. section 5.3.5). Within this thesis a first cool down of the interferometer could

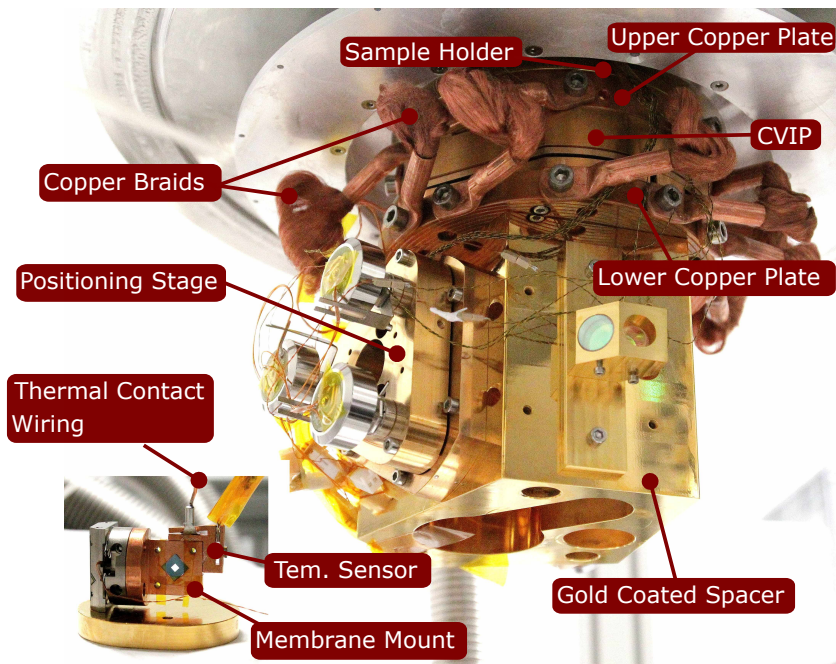


Figure 7.10.: *Interferometer Setup in the Cryostat.* The gold coated interferometer was mounted upside-down to the lower copper plate. 10 copper braids were screwed to the lower and upper copper plates to provide a good thermalisation. For same reason an additionally wire was connecting the membrane's copper mount with the upper copper plate.

be realized.

Cool Down of the Interferometer

The interferometer was cooled down with the modifications of the cryostat implemented, as described in section 5.3. The cool down performance is presented in figure 7.11. It was measured the decreasing temperature over time at the sample holder (green dots) and at the membrane mount (red dots). The blue measurement points present the temperature devolution

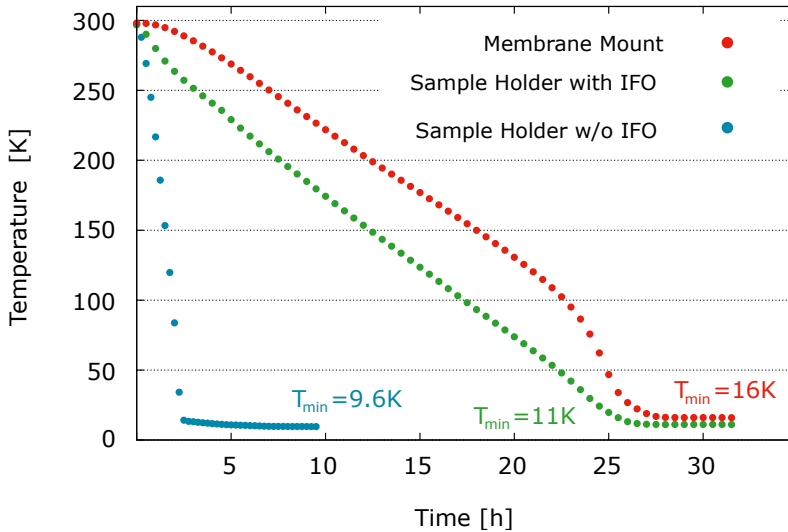


Figure 7.11.: *Cool down of the interferometer.* The blue measurement data represent the temperature development of the sample holder during a cool down without any additional mass (without interferometer, etc.). The minimum temperature of $T_{\min}=9.6$ K was reached in about 8 h of cooling time. For a second cool down the interferometer was implemented into the cryostat and the cool down was repeated. During this cool down the temperature was measured at the membrane mount (red dots) and at the sample holder (green dots). With this additional mass (i.e. heat capacity) the minimum temperatures of $T_{\min}=11$ K and $T_{\min}=16$ K were reached at the sample holder and the membrane mount after about 27h -29h cooling time.

for the sample holder for an "empty" chamber without additional masses in terms of interferometer, adapter plates, damping isolation plate. Without any additional mass a minimum temperature of $T_{\min}=9.6$ K could be reached in ≈ 8 h. The red and green measurement data were measured at the similar cool down run. With an additional mass of about 9.5 kg (interferometer, etc.) the sample holder reached a minimum temperature of $T_{\min}=11$ K in about 27 h. The minimum temperature of the membrane mount was $T_{\min}=16$ K, reached after 28 h of cooling. The extended time for the cool down was caused by the increased heat capacity (i.e. mass) and reduced thermal contact due to the interfaces, as described in section 5.1. Since the estimated overall heat load, through radiation and thermal conduction, were

7. Realized Interferometers at Cryogenic Temperatures

below the cooling power of the cryostat (cf. section 5.3), a temperature even lower than 16 K was expected. Improved results might be possible by gold-coating the positioners, by improving the polishing of the new aluminum shield, by adding more copper braids that connect the membrane holder and the cold plate, and by adding radiation insulation in terms of multilayer foil to the heat shield and the positioners.

Interferometer Performance

An impressive high contrast of $>99.96\%$ was achieved at 293 K. In the first cool down run showed that the misalignment due to thermal expansion was small and the realignment simple and fast in comparison of previous interferometer designs. Unfortunately a few electrical contacts of the new wiring broke during the first cool down, so that only 3 of 6 steering positioners were controllable. However with this restriction a contrast of $\mathcal{C}=0.98$ was achieved at 16 K.

7.3.4. Conclusion

It was shown that the new alignment process and the new positioning stages enable a high contrast of $> 99.93\%$ (cf. chapter 6.3) that is sufficient for observing radiation pressure noise on the SiN-membrane at 130 kHz. It is expected that the same high contrast can be reached with this setup also at cryogenic temperatures. The results of the first cool down of the new interferometer indicated that a still to high heat transfer existed. Using additional multilayer insulation at the heat shield and positioners and an increasing thermal contact at the membrane mount might result in the final goal temperature of ≈ 10 K. The improvements due to the new vibration isolation platform and new mounting of the steering mirrors could not be investigated by the time this thesis was handed in. From the simulation and design point of view a significant reduction of vibrations are expected, as shown in chapter 5.3.3.

8

Chapter 8.

Conclusion

In the framework of this thesis the following two main results were achieved:

- For the first time, generalized optomechanical coupling, including dissipative coupling was observed in a setup in which also the dissipative channel was accessible to photo-electric detection.
- A new remotely controllable Michelson-Sagnac interferometer, for operating at cryogenic temperatures with high displacement sensitivity, was realized and investigated.

Observed Optomechanical Coupling

The general theory of dissipative coupling in an optomechanical system due to an oscillator-motion dependent cavity linewidth, was first suggested by Elste et al. in [Els09]. In 2011 the presence of this coupling effect in the specific optomechanical system of a signal-recycled Michelson-Sagnac interferometer with signal-recycling mirror (SRM) reflectivity of unity, was predicted [Xue11]. Later in 2013 the generalized optomechanical coupling (interference of dissipative and dispersive coupling) in such an optomechanical system was investigated and theoretically modeled by S. Tarabrin et al. and published in [Tar13].

During this thesis the predicted generalized optomechanical coupling in a signal-recycled Michelson-Sagnac interferometer was observed. For the first time optical cooling, with strong dissipative coupling, was measured. This observation was in contrast to other experiments [Li09, Wu14], which observed dissipative coupling only generated by photon losses into inaccessible channels. The behavior of the optomechanical coupling in this interferometer cavity was investigated for several membrane and signal recycling mirror detunings. The measurements were in excellent agreement with the theoretical model. For a certain detuning a strong reduction of the effective temperature from room temperature to $T_{\text{eff}}=126$ mK could be observed. Thereby for the

8. Conclusion

first time cooling on cavity resonance was measured and also a second instability regime on the cooling side of the cavity resonance could be detected. These two observations were key evidences for the presence of dissipative coupling [Tar13].

The optical cooling results presented in this thesis might pave the way towards ground-state cooling of heavy oscillators. To increase the cooling the internal cavity losses had to be reduced in a further step. Even ground state cooling is possible if additionally the signal recycling mirror reflectivity would be increased to an power reflectivity of $r_{sr}^2 = 1.0$ [Xue11]. Therefore the detection scheme had to be changed to the input port of the interferometer (detection in cavity reflection).

The here experimentally confirmed generalized optomechanical coupling is not only interesting for the optomechanical community, but also highly related to the field of gravitational-wave detectors. The dissipative coupling could cause a stable spring [Tar13], as proposed in [Vos14], which results in an improvement of the gravitational-wave detectors.

Cryogenically cooled Interferometer

Since for the detection of radiation pressure noise the signal-recycled Michelson-Sagnac interferometer has to be cooled down, several interferometer designs were realized and investigated for the application in a cryogenic environment.

The starting point of this thesis, was an interferometer, which was only in air adjustable by hand, with maximum reachable contrast values of 97.4 % at 293 K and 20 % at 10 K. To improve the contrast performance of this interferometer, various interferometer designs were analyzed to maximize the contrast. Overall three different interferometer designs were simulated, realized and investigated at cryogenic temperatures:

- The first investigated interferometer was a quasi-monolithic interferometer built with a rigid spacer made out of Invar (ultra low thermal expansion), with fixed steering mirrors. Due to this the interferometer had a high dimensional stability at room temperature as well as at cryogenic temperatures. With a steady state thermal analysis the expected thermal induced deformations could be minimized. The finally experimentally reached contrast was 99.9 % at 293 K and 55 % at 10 K.
- The second interferometer followed a different concept and was a fully electronically tunable interferometer, with piezo-actuated positioners and a spacer made out of copper. Here the measured contrast was 99.5 % at 293 K and 99.5 % at 8 K, where the contrast could in principle be further improved. Due to this reached high contrast at low temperatures an spectrum with displacement sensitivity of $3 \cdot 10^{-16} \text{m}/\sqrt{\text{Hz}}$

was observed, which was the highest observed displacement sensitivity in the group so far. The biggest issue of this interferometer where vibrational noise which coupled into the interferometer through the positioners.

- Therefore a third interferometer was developed to combine the advantages of the two previous ones. Therefore the spacer was made out of Invar and in collaboration with the JANSSEN PRECISION ENGINEERING company a new positioning concept was developed and applied. It also was developed a new alignment procedure to reach higher contrast. Thereby a very high contrast of 99.96 % at 293 K could be observed. During a first cool-down a contrast of 98 % at 16 K could be measured. The contrast was limited due to electronically problems with the wiring inside the cryostat, which caused a restriction in alignment. However the positioning stages operated quite promising and a contrast value as high as that at room temperature should be feasible. Further reducing the temperature to about 10 K should also be possible following the suggestions made in section 7.3.3.

Overall, the new developed interferometer operation at low temperatures constitutes a big step towards the detection of radiation pressure noise. With a reachable contrast of 99.96 %, a determined total internal loss of 600-1000 ppm, and a signal-recycling reflectivity of $r_{sr}^2=0.9993$ a signal gain of about 20 could be expected. Changing the so far used membrane to a membrane with the realizable parameters of mechanical Q-factor $Q=1 \cdot 10^7$, reflectivity of $r_m^2 = 0.9$, a thickness of 50 nm, square surface of 1.5 mm \times 1.5 mm and a frequency close to 150 kHz the radiation pressure noise could be expected to be about 1.25 times above the thermal noise at 10 K.

B

Appendix B.

Appendix

B.1. Material Properties

The following tables, list the temperature dependent values of the key cryogenic material properties for materials selected. The key properties are: thermal conductivity, thermal expansion coefficient and specific heat capacity.

Table B.1.1: Thermal conductivity (W/(mK)) for different materials at different temperatures. [Eki06, Sim92, NIS17, Mar05, Cry17a]

Material	Notation	4 K	10 K	20 K	40 K	77 K	100 K	150 K	200 K	295 K
Standard Aluminum	Al 5083	3.3	8.4	17	33	55	66	85	99	118
Aluminum (99.5%)	AW-1050A	-	-	-	-	-	-	-	-	215
Aluminum (99.0-99.95%)	AW-1100A	54.2	141.8	281.3	388.7	290.1	249	220	215	212
Aluminum Alloy	AlMgSi0.5	-	-	-	-	-	-	-	-	210
Copper ($\geq 99.99\%$)	CW009A	630	1540	2430	1470	544	461	418	407	397
Copper Tin Alloy (Bronze)	CuSn6	1.7	5.1	10.5	19.6	32.2	38.5	49.3	57.6	70
Stainless Steel	304	0.27	0.9	2.2	4.7	7.9	9.2	11	13	15
Nickel-Iron Alloy (Invar)	Fe64Ni36	0.24	0.73	1.7	2.6	4.2	6.2	7.6	10	12
Titanium	Ti6Al4V	-	-	0.92	2.2	4.2	4.7	6.0	7.7	10.3
Teflon	PTFE	0.05	0.1	0.14	0.19	0.23	0.24	0.26	0.265	0.27
Phosphor Bronze	CuSnP	1.6	4.6	10	-	25	-	34	-	48

Table B.2.: Thermal Contraction $\Delta L/L_{293}$ for different materials at different temperatures and the thermal expansion coefficient at 293 K. [Eki06, Sim92, NIS17, Mar05]

Material	Notation	$\Delta L/L$ at 4 K [%]	$\Delta L/L$ at 40 K [%]	$\Delta L/L$ at 77 K [%]	$\Delta L/L$ at 100 K [%]	$\Delta L/L$ at 150 K [%]	$\Delta L/L$ at 200 K [%]	$\Delta L/L$ at 250 K [%]	α at 293 K $4[10^{-6}/K]$
Copper	Cu	0.324	0.322	0.302	0.282	0.221	0.148	0.07	16.7
Aluminum	Al	0.415	0.413	0.393	0.370	0.295	0.201	0.097	23.1
Bronze	CuSn6	0.331	0.327	0.308	0.285	0.223	0.15	0.073	17.0
Stainless Steel	304	0.296	0.296	0.281	0.261	0.206	0.139	0.066	15.1
Invar	Fe64Ni36	-	0.04	0.038	0.036	0.025	0.016	0.009	2.0
Titanium	Ti6Al4V	0.173	0.171	0.163	0.154	0.118	0.078	0.036	8.0
Teflon	PTFE	2.14	2.06	1.941	1.85	1.6	1.24	0.75	250
Silica Glass	ULE	-0.008	-0.005	-0.002	-0.0001	0.002	0.002	0.002	0.4

Table B.3.: Specific Heat Capacity $C_P [J/(kg K)]$ for different materials at different temperatures. [Eki06, Sim92, NIS17, Kup17]

Material	Notation	4 K	10 K	20 K	30 K	50 K	77 K	100 K	150 K	200 K	300 K
Copper	Cu	0.09	0.88	7.0	27	97	192	252	323	356	386
Aluminum	Al	0.26	1.4	8.9	32	142	336	481	684	797	902
Bronze	CuSn6	0.109	1.103	-	-	-	-	-	-	-	377
Stainless Steel	-	2.0	5.2	17	10	100	200	250	350	400	480
Invar	Fe64Ni36	1.0	3.1	12.3	-	-	-	-	-	-	515
Titanium	-	0.32	1.26	7.0	25	99	218	300	407	465	522
Teflon	PTFE	-	26	79	126	210	310	392	550	677	870
Silica Glass	ULE	-	0.7	11.3	35	97	185	261	413	543	745

Bibliography

- [Abb09] B. Abbott and et al., *Ligo: the laser interferometer gravitational-wave observatory*, Reports on Progress in Physics **72**, 076901 (2009). 16
- [Abr92] Abramovici and et al., *Ligo: The laser interferometer gravitational-wave observatory*, Science **256**, 325 (1992). 16
- [Ash78] A. Ashkin, *Trapping of atoms by resonance radiation pressure*, Phys. Rev. Lett. **40**, 729 (1978). 15
- [Asp14] M. Aspelmeyer, T. J. Kippenberg, and F. Marquardt, *Cavity optomechanics*, Rev. Mod. Phys. **86**, 1391 (2014). 15, 16, 39, 40
- [ATT17] ATTOCUBE, *attomotion premium line*, attocube system AG, (URL: <http://www.attocube.com> (June 2017)). 96, 102, 103
- [Bra97] V. Braginsky, M. Gorodetsky, and F. Khalili, *Optical bars in gravitational wave antennas*, Physics Letters A **232**, 340 (1997). 39
- [Bra01] V. Braginsky and S. Vyatchanin, *Frequency fluctuations of nonlinear origin in self-sustained optical oscillators*, Physics Letters A **279**, 154 (2001). 25
- [Buo01] A. Buonanno and Y. Chen, *Quantum noise in second generation, signal-recycled laser interferometric gravitational-wave detectors*, Physical Review D **64**, 042006 (2001). 16
- [Buo02] A. Buonanno and Y. Chen, *Signal recycled laser-interferometer gravitational-wave detectors as optical springs*, Physical Review D **65**, 042001 (2002). 39
- [Cav80] C. M. Caves, *Quantum-mechanical radiation-pressure fluctuations in an interferometer*, Physical Review Letters **45** (1980). 16, 24
- [Cha11] J. Chan, T. P. M. Alegre, A. H. Safavi-Naeini, J. T. Hill, A. Krause, S. Gröblacher, M. Aspelmeyer, and O. Painter, *Laser cooling of a nanomechanical oscillator into its quantum ground state.*, Nature **478**, 89 (2011). 16, 41
- [Che07] S. Chelkowski, *Squeezed Light and Laser Interferometric Gravitational Wave Detectors*, Ph.D. thesis, Fakultät für Mathematik und Physik der Gottfried Wilhelm Leibniz Universität Hannover (2007). 80

BIBLIOGRAPHY

- [Che13] Y. Chen, *Macroscopic quantum mechanics: theory and experimental concepts of optomechanics*, Journal of Physics B: Atomic, Molecular and Optical Physics **46**, 104001 (2013). 16
- [Col11] T. L. S. Collaboration, *A gravitational wave observatory operating beyond the quantum shot-noise limit*, Nature Physics **7**, 962 (2011). 24
- [Cor07] T. Corbitt, Y. Chen, E. Innerhofer, H. Müller-Ebhardt, D. Ottaway, H. Rehbein, D. Sigg, S. Whitcomb, C. Wipf, and N. Mavalvala, *An all-optical trap for a gram-scale mirror*, Physical Review Letters **98**, 150802 (2007). 19
- [Cro04] D. R. M. Crooks, G. Cagnoli, M. M. Fejer, A. Gretarsson, G. Harry, J. Hough, N. Nakagawa, S. Penn, R. Route, S. Rowan, and P. H. Sneddon, *Experimental measurements of coating mechanical loss factors*, Class. Quantum Grav. **21**, S1059–S1065 (2004). 25
- [Cry17a] L. S. Cryotronics, *Cryogenic-accessories-wire specification*, Lake Shore Cryotronics Inc. Company (URL: <http://http://www.lakeshore.com> (July 2017)). 58, 60, 72, 124
- [Cry17b] L. S. Cryotronics, *Specification for Silicon Diode Temperature sensor DT-670B-SD* (URL: <http://www.lakeshore.com> (July 2017)). 74
- [Ede78] W. A. Edelstein, J. Hough, J. R. Pugh, and W. Martin, *Limits to the measurement of displacement in an interferometric gravitational radiation detector*, J. Phys. E: Sci. Instrum **11**, 710 (1978). 23, 25
- [Eki06] J. W. Ekin, *Experimental Techniques for Low-Temperature Measurements*, OXFORD University Press (2006). 53, 54, 55, 56, 57, 58, 60, 61, 62, 66, 72, 97, 124, 125, 126
- [Els09] F. Elste, S. M. Girvin, and A. A. Clerk, *Quantum Noise Interference and Backaction Cooling in Cavity Nanomechanics*, Physical Review Letters **102**, 207209 (2009). 16, 41, 51, 119
- [Flo17] R. J. Floyd, Cryogenic Physicist and Applications Engineer of Janis Research Company, personal communication (2017). 71, 73
- [Fly05] T. M. Flynn, *Cryogenic Engineering*, Marcel Dekker (2005). 56, 57, 59
- [Fre81] H. Frey, *Tieftemperaturtechnologie*, VDI-Verlag GmbH (1981). 55, 56, 57, 60, 65
- [Fri33] R. Frisch, *Experimenteller nachweis des einsteinschen strahlungsrückstoßes*, Zeitschrift für Physik **86**, 42 (1933). 15

- [Fri11] D. Friedrich, H. Kaufer, T. Westphal, K. Yamamoto, A. Sawadsky, F. Y. Khalili, S. L. Danilishin, S. Goßler, K. Danzmann, and R. Schnabel, *Laser interferometry with translucent and absorbing mechanical oscillators*, *New Journal of Physics* **13**, 093017 (2011). 17, 19, 21, 49
- [Gri89] U. Grigull, *Thermophysikalische Stoffgrößen*, Springer-Verlag (1989). 97
- [Gro13] H. Grote, K. Danzmann, K. L. Dooley, R. Schnabel, J. Slutsky, and H. Vahlbruch, *First long-term application of squeezed states of light in a gravitational-wave observatory*, *Physical Review Letters* **110**, 181101 (2013). 24
- [Grö16] S. Gröblacher, Research Group Leader of the Groeblacher Lab of Delft University of Technology, personal communication (2016). 88
- [Hä75] T. Hänsch and A. Schawlow, *Cooling of gases by laser radiation*, *Optics Communications* **13**, 68 (1975). 15
- [Har10] G. M. Harry and LSC, *Advanced LIGO: the next generation of gravitational wave detectors*, *Classical and Quantum Gravity* **27**, 084006 (2010). 16, 24
- [Hei27] W. Heisenberg, *Über den anschaulichen inhalt der quantentheoretischen kinematik und mechanik*, *Zeitschrift für Physik* **43**, 172 (1927). 16
- [JAN17] JANIS, *Overview 10 kelvin closed-cycle refrigerator systems*, Janis Research Company Inc. (URL: <https://www.janis.com> (2017)). 66
- [Jen98] O. Jennrich, *Das Quantenlimit in der Interferometrie*, Ph.D. thesis, Universität Hannover (1998). 26
- [JPE15] JPE, Janssen Precision Engineering Company, Documentary (incl. Simulations) for the Cryo Vibration Isolation Platform (CVIP) (2015). 69, 70
- [JPE17] JPE, Janssen Precision Engineering Company, Cryo Linear Actuator (CLA) (URL: <http://www.janssenprecisionengineering.com> (2017)). 112
- [Kau12] H. Kaufer, A. Sawadsky, T. Westphal, D. Friedrich, and R. Schnabel, *Tomographic readout of an opto-mechanical interferometer*, *New Journal of Physics* **14**, 095018 (2012). 17, 43, 92
- [Kau13] H. Kaufer, *Opto-mechanics in a Michelson-Sagnac interferometer*, Ph.D. thesis, QUEST-Leibniz-Forschungsschule der Gottfried Wilhelm Leibniz Universität Hannover (2013). 16, 17, 19, 22, 26, 27, 28, 31, 43, 44, 45, 46, 67, 77, 83, 84, 91, 92, 93, 101, 107, 113

BIBLIOGRAPHY

- [Kha01] F. Khalili, *Frequency-dependent rigidity in large-scale interferometric gravitational-wave detectors*, Physics Letters A **288**, 251 (2001). 39
- [Kha16] F. Y. Khalili, S. P. Tarabrin, K. Hammerer, and R. Schnabel, *Generalized analysis of quantum noise and dynamic backaction in signal-recycled michelson-type laser interferometers*, Phys. Rev. A **94**, 013844 (2016). 39, 41, 44, 51
- [Kim01] H. J. Kimble, Y. Levin, A. B. Matsko, K. S. Thorne, and S. P. Vyatchanin, *Conversion of conventional gravitational-wave interferometers into quantum nondemolition interferometers by modifying their input and output optics*, Physical Review D **65**, 022002 (2001). 25, 80
- [Kip05] T. J. Kippenberg, H. Rokhsari, T. Carmon, A. Scherer, and K. J. Vahala, *Analysis of radiation-pressure induced mechanical oscillation of an optical microcavity*, Physical Review Letters **95**, 033901 (2005). 19
- [Kip08] T. J. Kippenberg and K. J. Vahala, *Cavity optomechanics: Back-action at the mesoscale*, Science **321**, 1172 (2008). 19
- [Kit49] C. Kittel, *Interpretation of the thermal conductivity of glasses*, Physical Review **75**, 6 (1949). 58
- [Kit92] P. Kittel, A. L. Spivak, and L. J. Salerno, *Thermal conductance of gold plated metallic contacts at liquid helium temperatures*, Advances in cryogenic engineering, **37**, 241 (1992). 54
- [Kle06] D. Kleckner and D. Bouwmeester, *Sub-kelvin optical cooling of a micromechanical resonator*, Nature **444**, 75 (2006). 19
- [Kup17] D. Kupferinstitut, Wekstoffe Datenblätter: CuSn6 (URL: <https://www.kupferinstitut.de> (2017)). 60, 62, 126
- [Leb01] P. Lebedew, *Untersuchungen über die druckkräfte des liches*, Annalen der Physik **311**, 433 (1901). 15
- [Li99] Y.-Q. Li, D. Guzun, and M. Xiao, *Sub-shot-noise-limited optical heterodyne detection using an amplitude-squeezed local oscillator*, Physical Review Letters **82**, 5225 (1999). 25
- [Li09] M. Li, W. H. P. Pernice, and H. X. Tang, *Reactive Cavity Optical Force on Microdisk-Coupled Nanomechanical Beam Waveguides*, Physical Review Letters **103**, 223901 (2009). 41, 52, 119
- [Mai60] T. Maiman, *Stimulated optical radiation in ruby*, Nature **187**, 493 (1960). 15

- [Man67] A. Manukin and V. Braginsky, *Ponderomotive effects of electromagnetic radiation*, Soviet Physics JETP **25**, 986 (1967). 15
- [Man77] A. B. Manukin and V. Braginsky, *Measurement of waek force in physics experiments*, University of Chicago Press (1977). 15
- [Man12] Manual, *Operation instructions for the janis research ccs-xg-ch204 refrigerator system*, Janis Research Company Inc. (2012). 63, 64, 66
- [Mar05] W. Martienssen and H. Warlimont, *Spinger Handbook of Condensed Matter and materials Data*, Springer Verlag (2005). 58, 60, 61, 124, 125
- [Mar07] F. Marquardt, J. P. Chen, A. A. Clerk, and S. M. Girvin, *Quantum theory of cavity-assisted sideband cooling of mechanical motion*, Phys. Rev. Lett. **99**, 093902 (2007). 40
- [ME08] H. Müller-Ebhardt, H. Rehbein, R. Schnabel, K. Danzmann, and Y. Chen, *Entanglement of macroscopic test masses and the standard quantum limit in laser interferometry*, Physical Review Letters **100**, 013601 (2008). 17
- [Mee88] B. Meers, *Recycling in laser-interferometric gravitational-wave detectors*, Physical Review D **38** (1988). 17, 31
- [Meh10] M. Mehmet, T. E. snd S. Steinlechner snd H. Vahlbruch, and R. Schnabel, *Demonstration of a quantum-enhanced fiber sagnac interferometer*, Optical Letters **35**, 1665 (2010). 24
- [Mey13] P. Meystre, *A short walk through quantum optomechanics*, Annalen der Physik **525**, 215 (2013). 16
- [Mus05] V. Musilova, P. Hanzelka, T. Kralik, and A. Srnka, *Low temperature radiative properties of materials used in cryogenics*, Cryogenics **45**, 529 (2005). 56
- [Net17] N. A. Net, Invar - Nickel Iron Alloy (URL: <http://http://www.nickel-alloys.net> (Junly 2017)). 60
- [Nia13] R. M. Nia, *Kryogene Laserinterferometrie mit einer SiN-Membran*, Institut für Gravitationsphysik Leibniz Universität Hannover und Max-Planck-Institut für Gravitationsphysik Albert-Einstein-Institut Hannover (Master thesis 2013). 67, 77, 91, 93, 96, 100, 101, 107
- [Nic01] E. F. Nichols and G. F. Hull, *A preliminary communication on the pressure of heat and light radiation*, Phys. Rev. (Series I) **13**, 307 (1901). 15
- [NIS17] NIST, *Cryogenic technologies group*, National Institute of Standards and Technology, Material Measurement Laboratory (URL: <http://cryogenics.nist.gov> (2017)). 58, 61, 62, 124, 125, 126

BIBLIOGRAPHY

- [NOR12] NORCADA, Norcada company (2012). 21
- [Nor16] R. A. Norte, J. P. Moura, and S. Gröblacher, *Mechanical resonators for quantum optomechanics experiments at room temperature*, Phys. Rev. Lett. **116**, 147202 (2016). 88
- [Nyq28] H. Nyquist, *Thermal agitation of electric charge in conductors*, Class. Quantum Grav. **32**, 110 (1928). 25
- [Qua17] H. Quarsglas, Heraeus Quarsglas GmbH & Co. KG., Product Information sheet 2017- Suprasil 3001 (URL: <http://www.optik.heraeus-quarzglas.com> (2017)). 84, 85
- [Sau90] P. R. Saulson, *Thermal noise in mechanical experiments*, Physical Review D **42** (1990). 26
- [Saw12] A. Sawadsky, *Das Michelson-Sagnac-Interferometer mit SiN-Membran und Signal-Recycling*, Institut für Gravitationsphysik Leibniz Universität Hannover und Max-Planck-Institut für Gravitationsphysik Albert-Einstein-Institut Hannover (Master thesis 2012). 16, 17, 19, 22, 25, 26, 31, 43, 45, 92, 107, 113
- [Saw15] A. Sawadsky, H. Kaufer, R. M. Nia, S. P. Tarabrin, F. Y. Khalili, K. Hammerer, and R. Schnabel, *Observation of generalized optomechanical coupling and cooling on cavity resonance*, Phys. Rev. Lett. **114**, 043601 (2015). 16, 43, 45, 47, 49, 50, 92, 133
- [Ser17] I. Services, *Infrared service inc.*, Infrared Thermography (URL:<http://www.infrared-thermography.com> (Junly 2017)). 56
- [Sie86] A. E. Siegman, *LASERS*, University Science Books (1986). 86
- [Sim92] N. Simon, *Properties of Copper and Copper Alloys at Cryogenic Temperatures*, National Institute of Standards and Technology Monograph (1992). 58, 61, 62, 124, 125, 126
- [Ste86] S. Stenholm, *The semiclassical theory of laser cooling*, Rev. Mod. Phys. **58**, 699 (1986). 15
- [Ste13] J. Steinlechner, *Optical absorption measurements for third-generation gravitational wave detectors*, Ph.D. thesis, Gottfried Wilhelm Leibniz Universität Hannover (2013). 21, 77
- [Ste14] M. Steinecke, *Entwurf und Aufbau eines monolithischen Michelson-Sagnac-Interferometers*, Institut für Gravitationsphysik Leibniz Universität Hannover und Max-Planck-Institut für Gravitationsphysik Albert-Einstein-Institut Hannover (Bachelor Thesis (2014)). 94, 95, 96, 98, 99

- [Ste17] J. Steinlechner, C. Krüger, I. W. Martin, A. Bell, J. Hough, H. Kaufer, S. Rowan, R. Schnabel, , and S. Steinlechner, *Optical absorption of silicon nitride membranes at 1064 nm and at 1550 nm*, Phys. Rev. D **96**, 022007 (2017). 28, 77, 84
- [sup] See Supplementary Material at [Saw15] for calculations . 40, 51
- [SW14] D. S. S.I. Woods, T.M. Jung and J. Yu, *emissivity of silver and stainless steel from 80 k to 300 k: Application to iter thermal shields*, Cryogenics **60**, 44 (2014). 56
- [Tar13] S. P. Tarabrin, H. Kaufer, F. Y. Khalili, R. Schnabel, and K. Hammerer, *Anomalous dynamic backaction in interferometers*, Physical Review A **88**, 023809 (2013). 16, 22, 33, 35, 39, 40, 41, 43, 44, 51, 52, 119, 120
- [Vah05] H. Vahlbruch, S. Chelkowski, B. Hage, A. Franzen, K. Danzmann, and R. Schnabel, *Demonstration of a squeezed-light-enhanced power- and signal-recycled michelson interferometer*, Physical Review Letters **95**, 211102 (2005). 24
- [vB17] B. van Bree, engineer from Janssen Precision Engineering (JPE) company, personal communication (2017). 69, 70, 71
- [Vit07] D. Vitali, S. Gigan, A. Ferreira, H. R. Böhm, P. Tombesi, A. Guerreiro, V. Vedral, A. Zeilinger, and M. Aspelmeyer, *Optomechanical entanglement between a movable mirror and a cavity field*, Physical Review Letters **98**, 030405 (2007). 17
- [vL41] J. von Lammeren, *Technik der tiefen Temperaturen*, Verlag von Julius Springer (1941). 53
- [Vor] V. B. Y. Vorontsov and F. Khalili, *Optimal quantum measurements in detectors of gravitation radiation*, JETP Letters **27**, 276. 15
- [Vos14] N. Vostrosablin and S. P. Vyatchanin, *Stable optical spring in the Advanced LIGO detector with unbalanced arms and in the Michelson-Sagnac interferometer*, Physical Review D **89**, 062005 (2014). 16, 52, 120
- [Wei98] J. G. Weisend, *Handbook of Cryogenic Engineering*, Tayler & Francis (1998). 54, 55, 65
- [Wei13] T. Weiss and A. Nunnenkamp, *Quantum limit of laser cooling in dispersively and dissipatively coupled optomechanical systems*, Phys. Rev. A **88**, 023850 (2013). 41
- [Wei16] J. G. Weisend, *Cryostat Design*, International Cryogenics Monograph Series, Springer International Publishing Switzerland (2016). 54

BIBLIOGRAPHY

- [Wes09] T. Westphal, *Opto-mechanische Kopplung in einem Michelson-Sagnac Interferometer*, Institut für Gravitationsphysik Leibniz Universität Hannover und Max-Planck-Institut für Gravitationsphysik Albert-Einstein-Institut Hannover (diploma thesis 2009). 19, 20, 23, 26, 44, 48, 64, 92
- [Wes12] T. Westphal, D. Friedrich, H. Kaufer, K. Yamamoto, S. Gößler, H. Müller-Ebhardt, S. L. Danilishin, F. Y. Khalili, K. Danzmann, and R. Schnabel, *Interferometer readout noise below the standard quantum limit of a membrane*, *Physical Review A* **85**, 063806 (2012). 17, 48, 92
- [Wra59] K. L. Wray and T. J. Connolly, *Thermal conductivity of clear fused silica at high temperatures*, *Journal of Applied Physics* **30**, 11 (1959). 58
- [Wu14] M. Wu, A. C. Hryciw, C. Healey, D. P. Lake, H. Jayakumar, M. R. Freeman, J. P. Davis, and P. E. Barclay, *Dissipative and Dispersive Optomechanics in a Nanocavity Torque Sensor*, *Physical Review X* **4**, 021052 (2014). 41, 52, 119
- [Xue11] A. Xuereb, R. Schnabel, and K. Hammerer, *Dissipative optomechanics in a michelson sagnac interferometer*, *Physical Review Letters* **107**, 213604 (2011). 39, 41, 51, 119, 120
- [Yam10] K. Yamamoto, D. Friedrich, T. Westphal, S. Gößler, K. Danzmann, K. Somiya, S. L. Danilishin, and R. Schnabel, *Quantum noise of a Michelson-Sagnac interferometer with translucent mechanical oscillator*, *Physical Review A* **81**, 033849 (2010). 17, 21, 24, 31, 37
- [Zwi08] B. M. Zwickl, W. E. Shanks, A. M. Jayich, C. Yang, A. C. B. Jayich, J. D. Thompson, and J. G. E. Harris, *High quality mechanical and optical properties of commercial silicon nitride membranes*, *Applied Physics Letters* **92**, 103125 (2008). 19, 20

List of Publications

- [Saw15-1] A. Sawadsky, H. Kaufer, R. M. Nia, S. P. Tarabrin, F. Y. Khalili, K. Hammerer, and R. Schnabel, *Observation of generalized optomechanical coupling and cooling on cavity resonance*, Phys. Rev. Lett. **114**, 043601 (2015).
- [Saw15-2] A. Sawadsky, K. Hammerer, and R. Schnabel, *Kühlen von großen Objekten mit Laserlicht*, Physik in unserer Zeit **46**, 162 (2015).
- [Kau12] H. Kaufer, A. Sawadsky, T. Westphal, D. Friedrich, and R. Schnabel, *Tomographic readout of an opto-mechanical interferometer*, New Journal of Physics **14**, 095018 (2012).
- [Fri11] D. Friedrich, H. Kaufer, T. Westphal, K. Yamamoto, A. Sawadsky, F. Y. Khalili, S. Danilishin, S. Goßler, K. Danzmann, and R. Schnabel, *Laser interferometry with translucent and absorbing mechanical oscillators*, New Journal of Physics **13**, 093017 (2011).
- [Abb16a] B. Abbott, R. Abbott, T. Abbott, M. Abernathy, F. Acernese, K. Ackley, C. Adams, T. Adams, P. Addesso, R. Adhikari, *et al.*, *Binary black hole mergers in the first advanced LIGO observing run*, Physical Review X **6**, 041015 (2016).
- [Abb16b] B. Abbott, R. Abbott, T. Abbott, M. Abernathy, F. Acernese, K. Ackley, C. Adams, T. Adams, P. Addesso, R. Adhikari, *et al.*, *Comprehensive all-sky search for periodic gravitational waves in the sixth science run LIGO data*, Physical Review D **94**, 042002 (2016).
- [Abb16c] B. Abbott, R. Abbott, T. Abbott, M. Abernathy, F. Acernese, K. Ackley, C. Adams, T. Adams, P. Addesso, R. Adhikari, *et al.*, *Directly comparing GW150914 with numerical solutions of Einstein's equations for binary black hole coalescence*, Physical Review D **94**, 064035 (2016).
- [Abb16d] B. Abbott, R. Abbott, T. Abbott, M. Abernathy, F. Acernese, K. Ackley, C. Adams, T. Adams, P. Addesso, R. Adhikari, *et al.*, *First targeted search for gravitational-wave bursts from core-collapse supernovae in data of first-generation laser interferometer detectors*, Physical Review D **94**, 102001 (2016).
- [Abb16e] B. Abbott, R. Abbott, T. Abbott, M. Abernathy, F. Acernese, K. Ackley, C. Adams, T. Adams, P. Addesso, R. Adhikari, *et al.*,

LIST OF PUBLICATIONS

- Improved analysis of gw150914 using a fully spin-precessing waveform model*, Physical Review X **6**, 041014 (2016).
- [Abb16f] B. Abbott, R. Abbott, T. Abbott, M. Abernathy, F. Acernese, K. Ackley, C. Adams, T. Adams, P. Addesso, R. Adhikari, *et al.*, *Observing gravitational-wave transient gw150914 with minimal assumptions*, Physical Review D **93**, 122004 (2016).
- [Abb16g] B. Abbott, R. Abbott, T. Abbott, M. Abernathy, F. Acernese, K. Ackley, C. Adams, T. Adams, P. Addesso, R. Adhikari, *et al.*, *Results of the deepest all-sky survey for continuous gravitational waves on ligo s6 data running on the einstein@home volunteer distributed computing project*, Physical Review D **94**, 102002 (2016).
- [Abb16h] B. P. Abbott, R. Abbott, T. Abbott, M. Abernathy, F. Acernese, K. Ackley, C. Adams, T. Adams, P. Addesso, R. Adhikari, *et al.*, *Observation of gravitational waves from a binary black hole merger*, Physical review letters **116**, 061102 (2016).
- [Abb16i] B. P. Abbott, R. Abbott, T. Abbott, M. Abernathy, F. Acernese, K. Ackley, C. Adams, T. Adams, P. Addesso, R. Adhikari, *et al.*, *Prospects for observing and localizing gravitational-wave transients with advanced ligo and advanced virgo*, Living Reviews in Relativity **19**, 1 (2016).
- [Abb16j] B. P. Abbott, R. Abbott, T. Abbott, M. Abernathy, F. Acernese, K. Ackley, C. Adams, T. Adams, P. Addesso, R. Adhikari, *et al.*, *The rate of binary black hole mergers inferred from advanced ligo observations surrounding gw150914*, The Astrophysical Journal Letters **833**, L1 (2016).
- [Abb16k] B. P. Abbott, R. Abbott, T. Abbott, M. Abernathy, F. Acernese, K. Ackley, C. Adams, T. Adams, P. Addesso, R. Adhikari, *et al.*, *Upper limits on the rates of binary neutron star and neutron star–black hole mergers from advanced ligo’s first observing run*, The Astrophysical Journal Letters **832**, L21 (2016).
- [Abb17a] B. Abbott, R. Abbott, T. Abbott, M. Abernathy, F. Acernese, K. Ackley, C. Adams, T. Adams, P. Addesso, R. Adhikari, *et al.*, *All-sky search for short gravitational-wave bursts in the first advanced ligo run*, Physical Review D **95**, 042003 (2017).
- [Abb17b] B. Abbott, R. Abbott, T. Abbott, M. Abernathy, F. Acernese, K. Ackley, C. Adams, T. Adams, P. Addesso, R. Adhikari, *et al.*, *Directional limits on persistent gravitational waves from advanced ligo’s first observing run*, Physical review letters **118**, 121102 (2017).

- [Abb17c] B. Abbott, R. Abbott, T. Abbott, M. Abernathy, F. Acernese, K. Ackley, C. Adams, T. Adams, P. Addesso, R. Adhikari, *et al.*, *Effects of waveform model systematics on the interpretation of gw150914*, *Classical and Quantum Gravity* **34**, 104002 (2017).
- [Abb17d] B. Abbott, R. Abbott, T. Abbott, M. Abernathy, F. Acernese, K. Ackley, C. Adams, T. Adams, P. Addesso, R. Adhikari, *et al.*, *First search for gravitational waves from known pulsars with advanced ligo*, *The Astrophysical Journal* **839**, 12 (2017).
- [Abb17e] B. Abbott, R. Abbott, T. Abbott, M. Abernathy, F. Acernese, K. Ackley, C. Adams, T. Adams, P. Addesso, R. Adhikari, *et al.*, *Search for continuous gravitational waves from neutron stars in globular cluster ngc 6544*, *Physical Review D* **95**, 082005 (2017).
- [Abb17f] B. Abbott, R. Abbott, T. Abbott, M. Abernathy, F. Acernese, K. Ackley, C. Adams, T. Adams, P. Addesso, R. Adhikari, *et al.*, *Upper limits on the stochastic gravitational-wave background from advanced ligo's first observing run*, *Physical review letters* **118**, 121101 (2017).
- [Abb17g] B. Abbott, R. Abbott, T. Abbott, M. Abernathy, K. Ackley, C. Adams, P. Addesso, R. Adhikari, V. Adya, C. Affeldt, *et al.*, *Calibration of the advanced ligo detectors for the discovery of the binary black-hole merger gw150914*, *Physical Review D* **95**, 062003 (2017).
- [Abb17h] B. Abbott, R. Abbott, T. Abbott, M. Abernathy, K. Ackley, C. Adams, P. Addesso, R. Adhikari, V. Adya, C. Affeldt, *et al.*, *Exploring the sensitivity of next generation gravitational wave detectors*, *Classical and Quantum Gravity* **34**, 044001 (2017).
- [Alb17] A. Albert, M. André, M. Anghinolfi, G. Anton, M. Ardid, J.-J. Aubert, T. Avgitas, B. Baret, J. Barrios-Martí, S. Basa, *et al.*, *Search for high-energy neutrinos from gravitational wave event gw151226 and candidate lw151012 with antares and icecube*, *Physical Review D* **96**, 022005 (2017).
- [Sci17] L. Scientific, B. Abbott, R. Abbott, T. Abbott, F. Acernese, K. Ackley, C. Adams, T. Adams, P. Addesso, R. Adhikari, *et al.*, *Gw170104: Observation of a 50-solar-mass binary black hole coalescence at redshift 0.2*, *Physical Review Letters* **118**, 221101 (2017).

Acknowledgements

First of all I would like to thank Karsten Danzmann for creating and leading this institute. I feel very fortunate to have done research here, which includes the friendly and motivating atmosphere as well as the financial support for carrying out and presenting the research. This all made the daily work very enjoyable. I am very grateful to my supervisor Roman Schnabel who has supported me from the beginning of my master thesis up to the results presented here. You gave me the opportunity to work on interesting topics and always found time for engaging conversations. I thank H. Kaufer who supervised me in the lab during my master thesis, you pushed the experiment and i could learn a lot from you. Without your effort in your thesis it would not be possible to present this results in my thesis. For their excellent theoretical support and great work together, I would like to thank Prof. Klemens Hammerer and Dr. Sergey Tarabrin. Without your theoretical model it would not be possible to observe the generalized optomechanical coupling. I would like thank all my colleagues for the great time i had in the group. Specially thanks to Ramon Moghadsa Nia for great discussion in the office, Lisa for the huge amount of time you spend with me in the lab, and Sebastian Steinlechner for fruitful discussions. I would like to thank my family for all the love and support along the way.

Curriculum Vitae

Personal Data

Andreas Sawadsky

Email: sawand@gmx.de

Born: September 16, 1986 in Kazakhstan
married, 3 children, german

Academic History

- 2012–2017 Doctoral studies in Physics
 @ Intitute for Gravitational Physics, Gottfried Wilhelm
 Leibniz University of Hannover
- 2009–2012 Master of Science
 @ Intitute for Gravitational Physics, Gottfried Wilhelm
 Leibniz University of Hannover
- Master thesis:
 Das Michelson-Sagnac Interferometer mit SiN-Membran
 und Signal-Recycling (The Michelson-Sagnac Interfero-
 meter with SiN-Membrane and Signal-Recycling)
- 2006–2010 Bachelor of Science
 @ Intitute for Quantum Optics, Gottfried Wilhelm Leib-
 niz University of Hannover
- Bachelor thesis:
 Charakterisierungs Methoden für die Vibrationssensitivität
 von Ultrastabilen Resonatoren (Characterization meth-
 ods of the vibration sensitivity of ultra stable cavities)